UNIVERSITY OF ZAGREB

Faculty of Mechanical Engineering and Naval Architecture

MASTER'S THESIS

Marko Horvat

Zagreb, 2016

UNIVERSITY OF ZAGREB

Faculty of Mechanical Engineering and Naval Architecture

A STUDY OF ROTOR-STATOR INTERACTION MODELS FOR NUMERICAL PERFORMANCE PREDICTION OF CENTRIFUGAL PUMPS

Supervisor:

Prof. Hrvoje Jasak, PhD

Student:

Marko Horvat

Zagreb, 2016

I hereby declare that this thesis is entirely the result of my own work except where otherwise indicated. I have fully cited all used sources and I have only used the ones given in the list of references

I would like to thank everyone whose knowledge, insights and advices helped in the process of working on the thesis.

I am truly thankful to Professor Hrvoje Jasak for being the mentor of the thesis. I would also like to thank my friends and colleagues for helping me whenever needed and my special thanks goes to Gregor Cvijetić whose guidance and comments significantly contributed to the work presented in the thesis.

Last but not least, I would like to thank my girlfriend and parents for the support during the work on the thesis.

<div align="right">

Thank you,
Marko Horvat

</div>

Table of Contents

Nomenclature

Greek letters

ε	Dissipation of turbulent kinetic energy	m^2 / s^3
γ	Diffusion coefficient	m^2 / s^2
ω	Angular velocity	rad / s
ν	Kinematic viscosity	m^2 / s^2
ν_t	Kinematic eddy viscosity	m^2 / s^2
ν_{eff}	Kinematic effective viscosity	m^2 / s^2
Φ	Transported scalar variable	-
ρ	Density	kg / m^3

Latin letters

g	Gravitational acceleration	m / s^2
q	Heat flux	$W \cdot m$
u	Velocity	m / s
e	Specific internal energy	$J \cdot m^3 / kg$
k	Turbulent kinetic energy	m^2 / s^2
p	Kinematic pressure	m^2 / s^2
Q	Volumetric heat source	$W \cdot m^3 / kg$
t	Time	s

List of Figures

List of Tables

Abstract

Optimisation of flow in centrifugal pumps is often performed using Computational Fluid Dynamics (CFD). With the aid of CFD, pump geometry can be optimised without using expensive experiments. However, numerical simulations are an approximation of a real flow and an error in results is always present. Critical part of fluid flow assumption in pumps is the rotor-stator interface treatment which is used to couple rotor and stator zone into a single domain on a matrix level. Selection of the rotor-stator interface treatment used in flow simulation effects accuracy and time required to perform numerical simulation.

In this thesis, four different types of simulations are performed and compared:

- *multiple frames of reference* (MRF) with *general grid interface* (GGI) between rotor and stator zone,

- *multiple frames of reference* with *mixing plane* interface between rotor and stator zone,

- transient simulation with dynamic mesh and time averaged results and

- *harmonic balance method*.

The multiple frames of reference model is a steady state approximation of a transient flow, which enables a steady state simulation of turbomachinery by ignoring transient phenomena. Rotation of the rotor in the MRF is taken into account with additional terms in mathematical model, such as centrifugal and Coriolis term, without a dynamic mesh. The harmonic balance method is a quasi steady-state model which enables calculation of results in specific time instances of a transient flow using a steady-state formulation. This is only possible with the assumption that the flow is periodic and that each primitive variable can be accurately represented by a Fourier series in time. Due to complex geometries of turbomachinery numerical spatial domains are often made from more parts merged together. This often leads to non-conformal cell zones of rotor and stator. In this thesis, interfaces used for joining multiple non-conformal domains are GGI and mixing plane interface. Introduced numerical models are applied on two centrifugal pump geometries. $Q - H$ and $Q - \eta$ performance curves are approximated by a parabola defined with three operating points.

CPU time analysis is also covered. Additional methods, which are not specified in the assignment of the thesis, are done to compare additional numerical models. Comparison between consistent and non-consistent simulation shows that the consistent transient solver gives the solution with less oscillations. Comparison between coupled and segregated solver shows that the coupled solver, even though it requires more memory, improves the convergence of the results. Therefore with the development of new methods for simulations will in future converge faster, yielding lower CPU time.

Sažetak

U ovom radu su predstavljene različite metode koje se koriste kod sumulacija centrifugalnih pumpi. Simulacije se sve češće koriste jer se njima mogu zamijeniti skupe eksperimentalne metode kod optimizacije strujanja. Da bi sama simulacija bila izvediva, potrebno je definirati matematički model koji dobro opisuje fiziku zadanog problema. Danas je u upotrebi više različitih metoda jer simulacije nikad ne rezultiraju točnim rješenjem i dobivena rješenja su samo aproksimacija stvarnosti. Točnost rezultata ovisi o numeričkom modelu koji se koristi. U tu svrhu su u okviru ovog rada ispitane četiri različite numeričke metode:

- metoda višestrukih rotirajućih inercijskih koordinatnih sustava s *General Grid Interface* (GGI) sučeljem između rotirajuće i mirujuće zone,

- metoda višestrukih rotirajućih inercijskih koordinatnih sustava s *mixing plane* sučeljem između rotirajuće i mirujuće zone,

- tranzijentna simulacija s rotirajućom numeričkom mrežom i vremenski osrednjenim rezultatima te

- metoda harmoničke ravnoteže.

Rezultati dobiveni tranzijentnom simulacijom se smatraju najtočnijim i ostali rezultati su uspoređeni relativno u odnosu na njih. Simulacije su provedene na geometrijama dviju različitih centrifugalnih pumpi za više različitih radnih točki. Rezultati dobiveni za tri različite radne točke su iskorišteni za izradu radnih krivulja pumpi. $Q - H$ i $Q - \eta$ krivulje su aproksimirane parabolom. Kritični dio aproksimacije strujanja se odnosi na interakciju između rotora i statora. U tu svrhu je ispitan utjecaj dvije vrste interakcija na točnost rezultata; GGI i mixing plane sučelje.

Uz usporedbu točnosti rezultata je napravljena i analiza potrebnog računalnog vremena da se provedu simulacije za različite numeričke metode. Nove metode simulacije doprinose bržoj konvergenciji rezultata, ali zahtjevaju više računalnih resursa.

Prošireni sažetak
(EXTENDED ABSTRACT IN CROATIAN)

Uvod

U ovom radu su predstavljene različite metode koje se danas koriste u numeričkim simulacijama centrifugalnih pumpi. Numeričke mreže su napravljene na dvije geometrije. Prva pumpa je nazvana OTA-1, a druga OTA-2. Metode koje su uspoređene u sklopu ovog rada su:

- metoda višestrukih rotirajućih inercijskih koordinatnih sustava s *General Grid Interface* (GGI) sučeljem između rotirajuće i mirujuće zone,

- metoda višestrukih rotirajućih inercijskih koordinatnih sustava s *mixing plane* sučeljem između rotirajuće i mirujuće zone,

- tranzijentna simulacija s rotirajućom numeričkom mrežom i

- metoda harmoničke ravnoteže.

Matematički model

Matematički model koji se koristi za modeliranje strujanja poznat je pod nazivom Navier-Stokesove jednadžbe. To je sustav vektorske jednadžbe količine gibanja te skalarne jednadžbe očuvanja mase. Za nestlačivo strujanje, u odnosu na inercijski koordinatni sustav, za koje se pretpostavlja konstantna gustoća sustav jednadžbi glasi:

$$\frac{d\mathbf{u}_I}{dt} + \nabla \cdot (\mathbf{u}_I \otimes \mathbf{u}_I) = -\nabla p + \nabla \cdot (\nu \nabla \mathbf{u}_I) \tag{1}$$

$$\nabla \cdot \mathbf{u}_I = 0, \tag{2}$$

Jednadžba 1 predstavlja jednadžbu količine gibanja za nestlačivo strujanje. Član $\frac{d\mathbf{u}_I}{dt}$ predstavlja vremenski član, koji je u stacionarnim simulacijama jednak 0. Član $\nabla \cdot (\mathbf{u}_I \otimes \mathbf{u}_I)$ predstavlja konvektivni član. Indeks I označuje inercijski koordinatni sustav u odnosu na koji je definiran vektor brzine $\mathbf{u}_I$. Član $-\nabla p$ je izvorski član, a $\nabla \cdot (\nu \nabla \mathbf{u}_I)$ je difuzijski član. Jednadžba 2 proizlazi iz jednadžbe količine gibanja za nestlačivo strujanje. Ako se sustav jednadžbi 1 i 2 prilagodi relativnom koordinatnom sustavu s apsolutnom brzinom dobije se sustav jednadžbi koji se koristi u Multiple Reference Frame (MRF) modelu simulacije. Takav sustav jednadžbi glasi:

$$\frac{d\mathbf{u}_R}{dt} + \omega \times \mathbf{u}_I + \nabla \cdot (\mathbf{u}_R \otimes \mathbf{u}_I) = -\nabla p + \nabla \cdot (\nu \nabla \mathbf{u}_I), \quad (3)$$

$$\nabla \cdot \mathbf{u}_I = 0. \quad (4)$$

U jednadžbama 3 i 4 indeks R predstavlja relativni (rotacijski) koordinatni sustav u odnosu na koji se definira vektor brzine $\mathbf{u}_R$. Član $\omega \times \mathbf{u}_I$ uzima u obzir brzinu vrtnje rotacijskog koordinatnog sustava. MRF je metoda kojim se vrtnja može uzeti u obzir dodatnim članovima, kao što su Coriolisov i centrifugalni član, bez pomaka mreže. Kod takve metode domena se dijeli na više dijelova. U promatranom slučaju su geometrije pumpi podijeljene na tri dijela. Ti dijelovi su ulazna cijev s kućištem, rotor te izlazna cijev s kućištem. Za domenu koja rotira definirana je kutna brzina. Matematički model je opisan jednadžbama 3 i 4 u kojima se zanemaruju vremenski članovi. Granice pojedinih domena trebaju biti posebno opisane. Za potrebe simulacija prikazanih u ovom radu se u tu svrhu koristi GGI te mixing plane. Takvim sučeljima se mogu definirati granice između domena u slučaju kada površinske numeričke mreže na granici domena nisu komforne. Kod GGI sučelja koristi se direktna interpolacija varijabli strujanja s glavnog (master) patcha na sporedni (shadow) patch [3], dok se kod ravnivne miješanja prije interpolacije rješenja osrednjuju u obodnom smjeru na sučelju [4].

Numeričke mreže

Numeričke mreže su generirane na dobivenim geometrijama za obje pumpe u softverskom paketu *Pointwise* [5]. Mreže su generirane ručno što omogućuje veću kontrolu korisnika nad procesom generacije mreže, ali manjak iskustva i znanja korištenja paketom može rezultirati generacijom neiskoristive mreže. Na sljedećim slikama koje prikazuju geometriju i numeričku mrežu pumpi, mirujuća zona u izlaznim kanalima je obojana plavo, žuto je obojana zona ulazne cijevi, dok je crveno obojana zona uz rotorske lopatice. Na slici 1 su prikazane slike obje geometrije. Na slici 1a je prikazana geometrija pumpe OTA-1 dok je na slici 1b prikazana pumpa OTA-2. Može se vidjeti da je pumpa OTA-1 'in-line' pumpa moderne izvedbe sa spiralnim kućištem dok je OTA-2 centrifugalna pumpa sa statorskim kućištem koje prethodi rotorskom kućištu. Prikazana geometrija pumpe OTA-2 je modificirana u odnosu na originalno dobivenu, na način da su ulazna i izlazna cijev promijenjene. Kružni poprečni presjek cijevi je zamijenjen pravokutnim da se izbjegne kompliciran prijelaz topologija numeričke mreže iz cijevi okruglog poprečnog presjeka na statorsko kućište pravokutnog poprečnog presjeka.
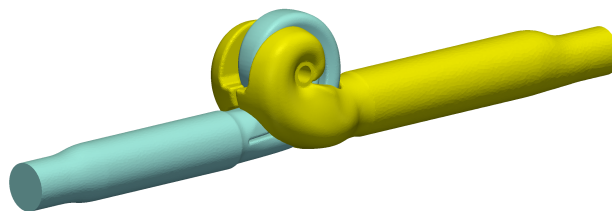
(a) OTA-1
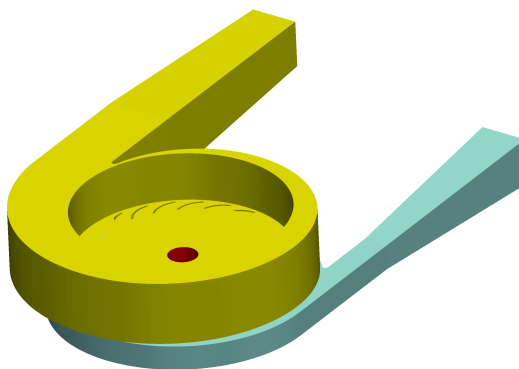
(b) OTA-2

Slika 1: Usporedba geometrija.

Na slici 2 su prikazani rotori pumpi. Prema obliku rotora može se zaključiti da je pumpa OTA-1 konstruirana za rad u cjevovodu kod kojeg je, po jedinici snage, potreban veći protok, a manja visina dobave od pumpe OTA-2.
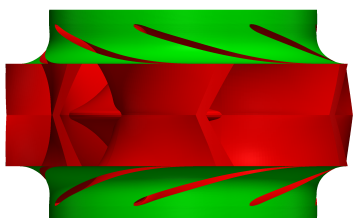
(a) OTA-1
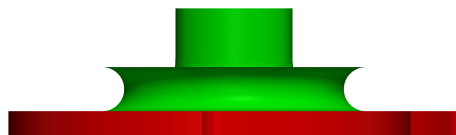
(b) OTA-2

Slika 2: Usporedba rotora.

Dio numeričke mreže OTA-1 pumpe prikazan je na slici 3. Na slici je prikazan poprečni presjek na kojem se vidi strukturu mreže. Vidljivo je da je mreža nestrukturirana u zoni ulazne cijevi te u zoni izlazne cijevi, a mreža strukturirana u zoni oko rotorskih lopatica. Takva izvedba mreže je poznata pod nazivom hibridna mreža. Ona je kompromis između točnosti rezultata te vremena potrebnog za generiranje same mreže. U zonama koje imaju najveći utjecaj na rezultate poželjno je da je mreža strukturirana. S druge strane, kod zona kompleksne geometrije koje ne utječu značajno na rezultate, nestrukturirana mreža doprinusi smanjenju vremena izrade mreže. Detalji slike prikazuju mrežu u zoni gdje je spiralno kućište spojeno s izlaznim kanalima, a također se može vidjeti dio mreže oko lopatica rotora. Uzevši u obzir boje u koje su pojedine zone obojane, može se vidjeti da je dio mirujuće statorske zone napravljen strukturirano. Razlog tome je da se izbjegnu problemi vezani uz relativno gibanje pojedinih zona u tranzijentnoj simulaciji i prijelaz sa strukturirane na nestrukturiranu mrežu na sučelju.
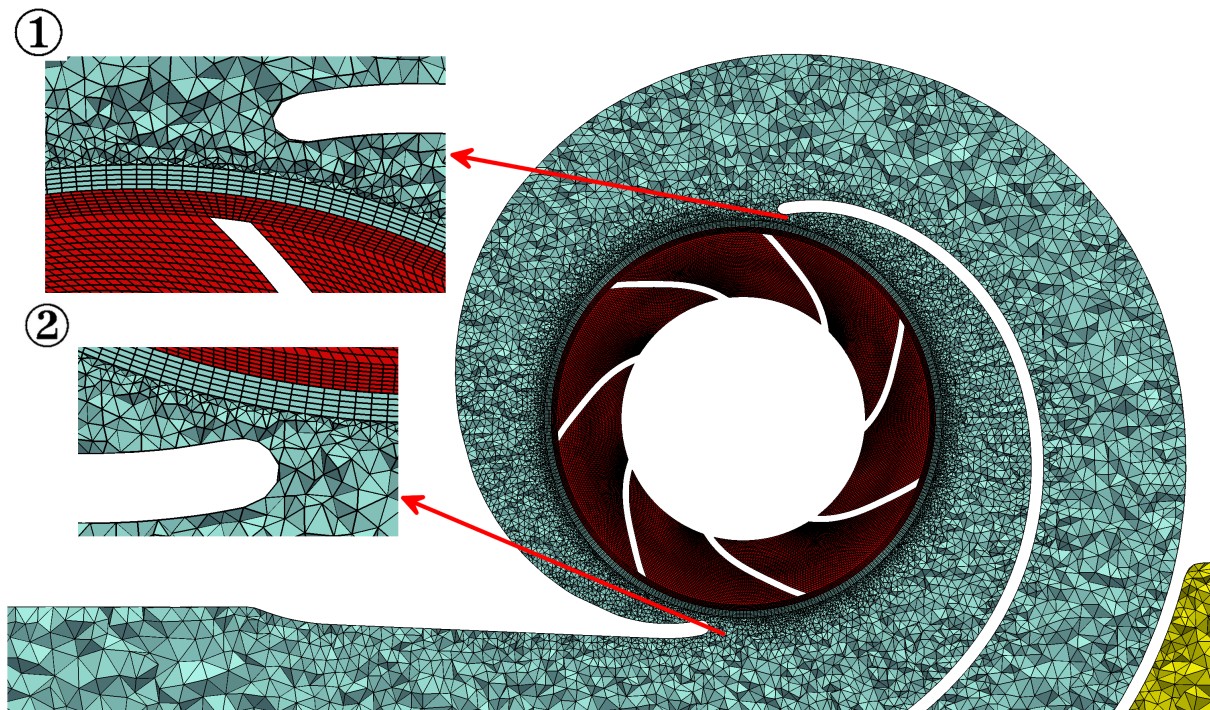
Slika 3: Poprečni presjek mreže OTA-1 pumpe.

Na slici 4 je prikazana mreža u statorskoj zoni pumpe OTA-2. Može se vidjeti da je zona napravljena potpuno strukturirano. Na detaljima slike su prikazani dijelovi oko rotorskih lopatica te oko spoja statorskog kućišta s ulaznom cijevi. Na slici 5 je prikazana mreža na poprečnom presjeku zone rotora. Detalji slike prikazuju zone mreže uz sučelje te oko spoja rotorskog kućišta s izlaznom cijevi. Na prvom detalju je također moguće vidjeti mrežu uz rotorsku lopaticu. Mreža pumpe OTA-2 je potpuno strukturirana.
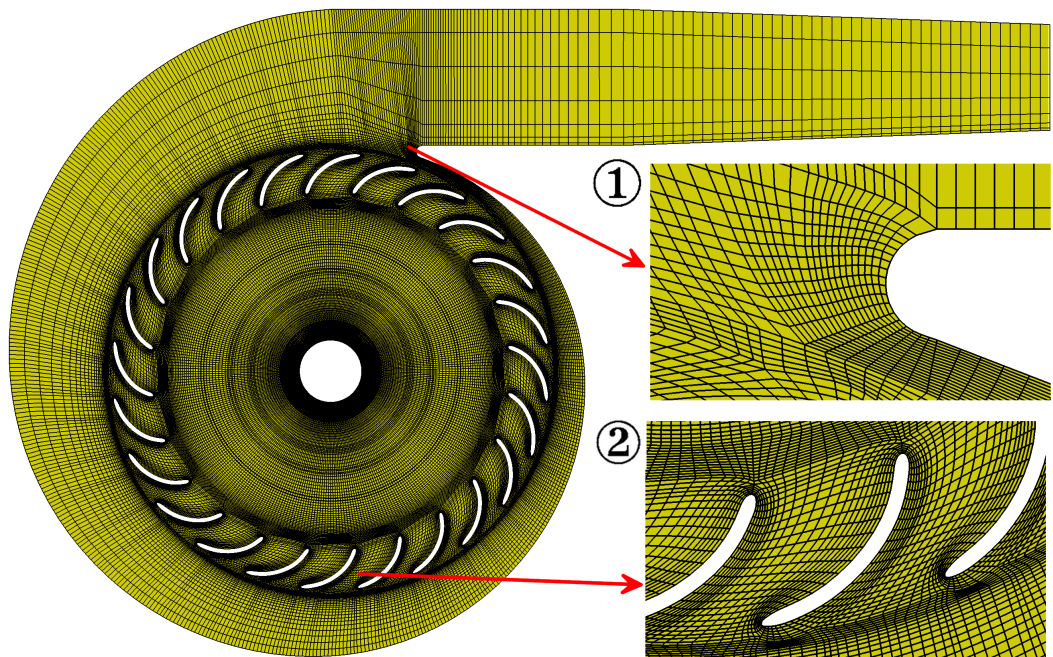
Slika 4: Poprečni presjek statorske zone mreže OTA-2 pumpe.
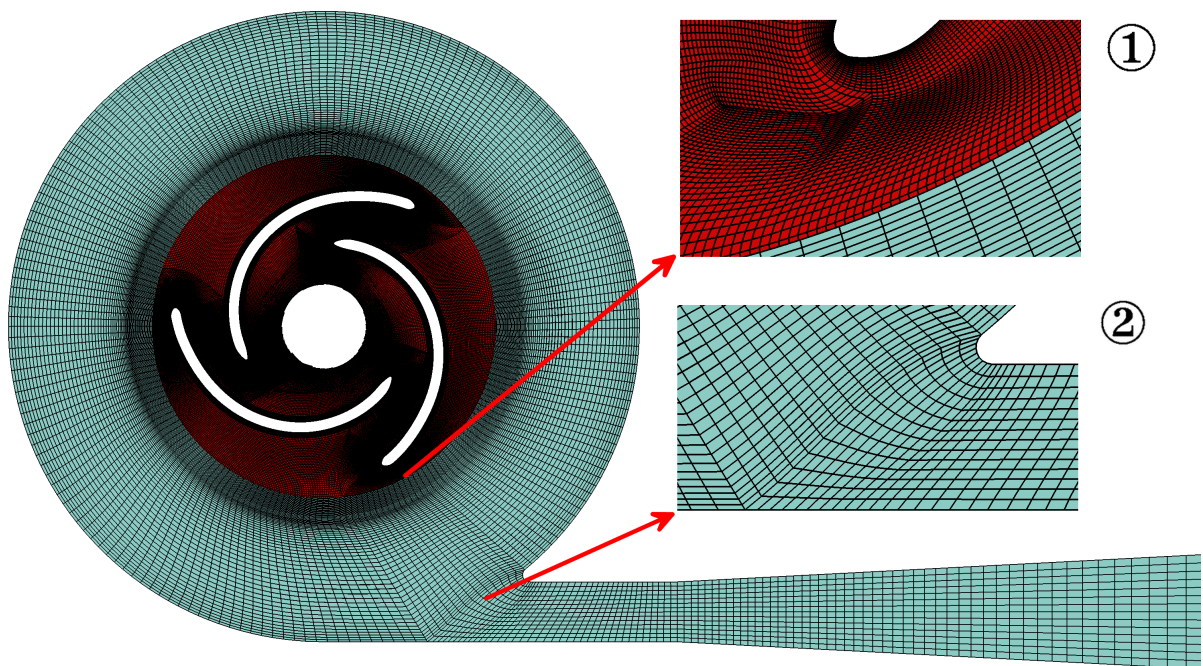
Slika 5: Poprečni presjek rotorske zone mreže OTA-2 pumpe.

Rezultati

Dobiveni rezultati simulacija su podjeljeni u dvije cjeline. Prva se bavi rezultatima dobivenih na mreži pumpe OTA-1 dok se druga bavi rezultatima pumpe OTA-2. U proširenom sažetku su dani sažeto samo dijelovi rezultata dok se opširnije prikazani rezultati nalaze u samom radu.

Pumpa OTA-1

Na slici 6 prikazana su polja brzine za različite numeričke modele. Na detalju svake slike je prikazano polje vektora brzine oko gornjeg dijela kućišta koji ima ulogu statorske lopatice. Potrebno je obratiti pozornost prilikom odabira metode simulacije na udaljenost između rotorskog i statorskog kućišta. Ako je udaljenost mala, kao na prikazanoj slici, mixing plane nije dobar odabir sučelja. Detaljniji prikaz usporedbe strujanja oko statorske lopatice, za različite tipove sučelja, je prikazan na slici 7. Opstrujavanje profila koje nije glatko rezultira znatnim padom iskoristivosti.

(a) Tranzijentna simulacija

(b) MRF (GGI)

(c) MRF (mixing plane)
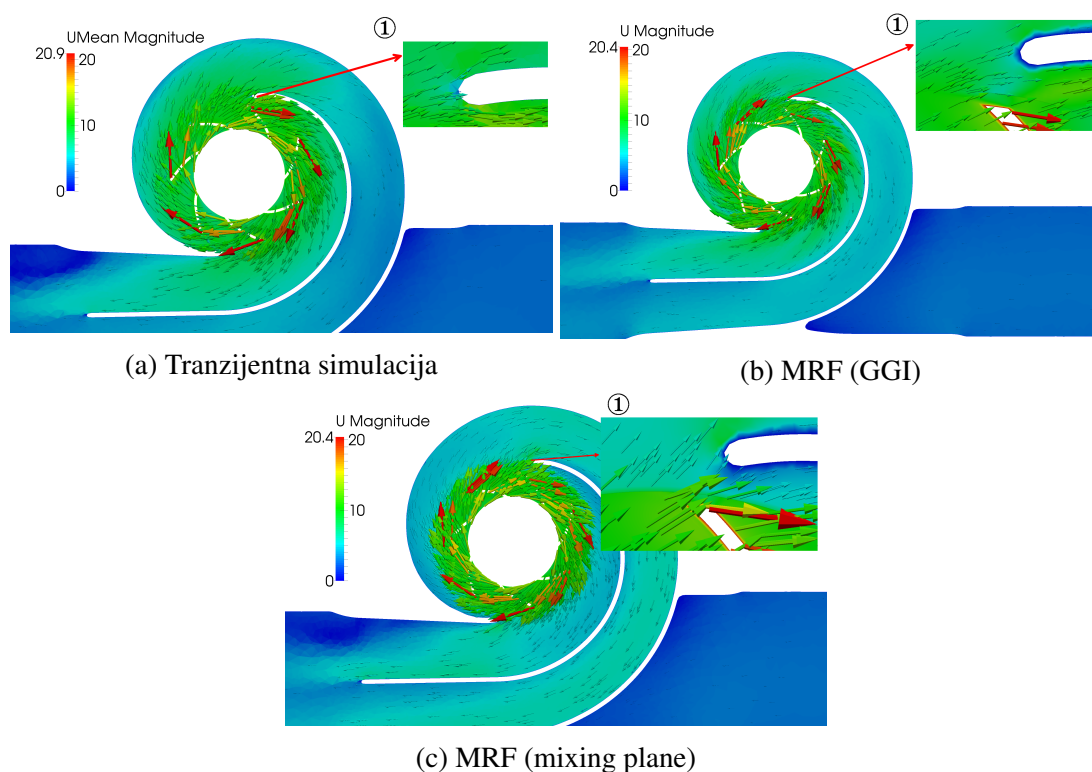
Slika 6: Usporedba polja brzine.

(a) GGI   (b) Mixing plane
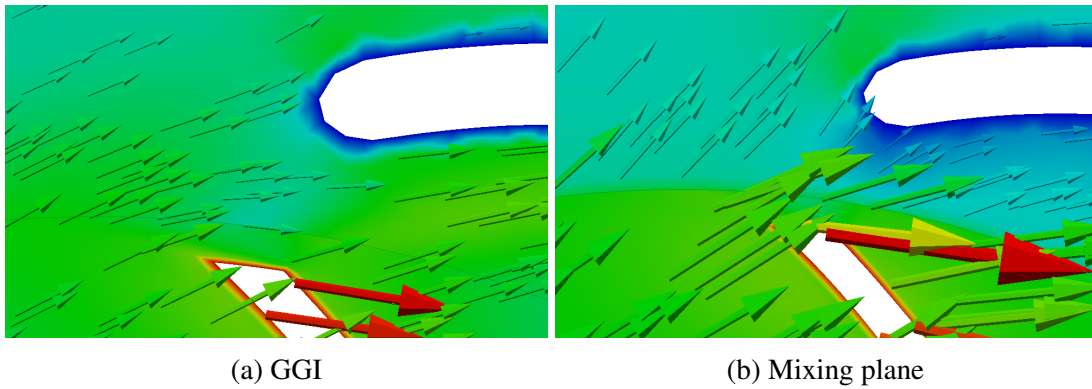
Slika 7: Usporedba strujanja oko statorske lopatice.

Usporedba polja tlaka za različite metode simulacije prikazana je na slici 8. Detalji slike prikazuju isti detalj kao za slike polja brzine. Također, ako se pogleda polje tlaka na detalju slike 8c može se vidjeti da je polje tlaka slično kao za strujanje oko profila za veće napadne kuteve što nije poželjno za opstrujavanje dijelova kućišta u pumpi.

(a) Tranzijentna simulacija   (b) MRF (GGI)

(c) MRF (mixing plane)
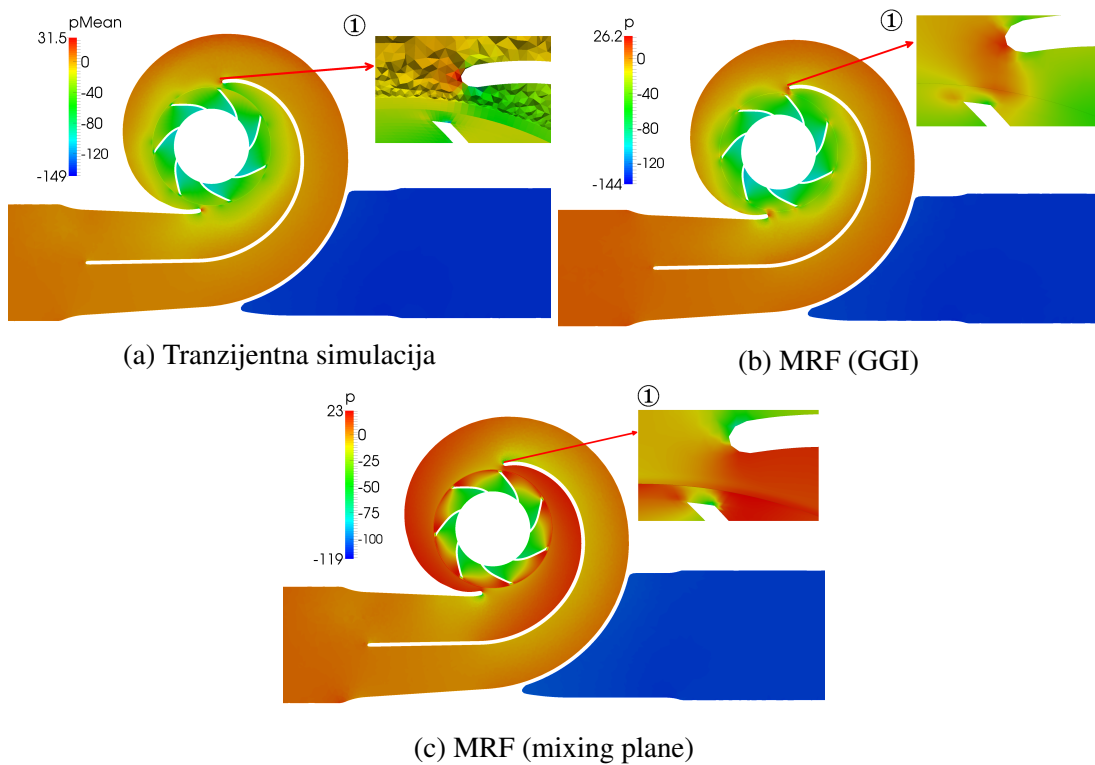
Slika 8: Usporedba polja brzine.

Radne točke pumpe su definirane volumenskim protokom, a simulacije su provedene za tri radne točke. Protok prve radna točke iznosi 14,5 m^3/min, druge 11,6 m^3/min i treće 17,4 m^3/min.

Podaci za pumpu OTA-1, za prvu radnu točku i za različite provedene metode prikazani su u tablici 1. Rezultati su uspoređeni pod pretpostavkom da je tranzijentna simulacija najtočnija

i za rezultate ostalih metoda su dane vrijednosti relativnih odstupanja rezultata u odnosu na tranzijentnu simulaciju. Vidljivo je da MRF simulacija kod koje se kao sučelje koristi GGI daje dobre rezultate dok rezultati MRF simulacije s mixing plane sučeljem odstupaju do 30%. Rezultati ostalih radnih točki MRF simulacije kod koje se kao sučelje koristi GGI su iskorišteni za izradu radne karakteristike pumpe. Ona je napravljena aproksimacijom dobivenih rezultata parabolom i prikazana je na slici 9.

Table 1: Usporedba rezultata za prvu radnu točku OTA-1 pumpe.

Simulacija	Visina dobave, m	H_{Err} , %	η , %	η_{Err} , %	Snaga, W	P_{Err} , %
Tranzijenta	15	-	85	-	41600	-
MRF (GGI)	14,47	3,53	87,1	-2,47	39013,9	6,2
MRF (mixing plane)	11,92	20,53	59,7	29,76	46918,1	-12.78
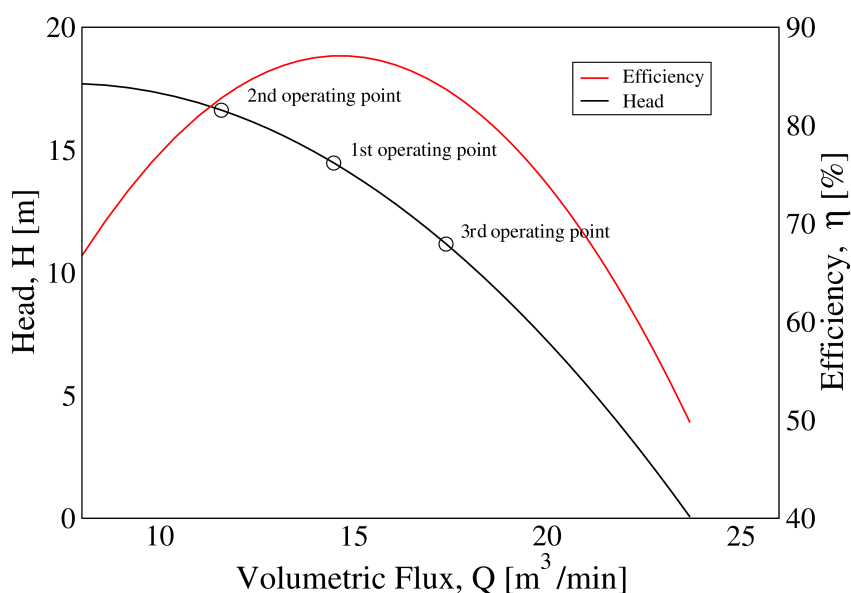
Slika 9: Radna karakteristika OTA-1 pumpe.

Pumpa OTA-2

Na slici 10 je prikazana usporedba polja brzine u statorskom kućištu za različite matematičke modele. Iz prikazanog se može vidjeti da je mreža napravljena za MRF simulaciju s GGI sučeljem, na originalnoj geometriji, što je vidljivo iz slike 10a. Originalna mreža je kasnije zamijenjena modificiranom jer se originalna mreža sastoji od previše ćelija što s dostupnim računalnim resursima, za tranzijentnu simulaciju, daje rezultate u neprihvatljivom vremenskom periodu. Na prvom detalju slike 10a prikazan je oblik toka nakon statorskih lopatica. Može se vidjeti da statorske lopatice usmjeravaju tok spiralno prema zoni rotora. Brzina toka se s približavanjem rotoru povećava jer se smanjuje površina presjeka za strujanje. Na ostalim detaljima je prikazana raspodjela vektora brzine preko statorskih lopatica. Na slici 11 je prikazana usporedba polja tlaka u zoni statora. Pad tlaka koji se javlja je posljedica povećanja brzine, a dodatno i trenja koje se javlja u strujanju. Oblik profila tlaka oko statorskih lopatica sličan je profilu tlaka kod strujanja oko proizvoljno odabranog aero-profila.

(a) Tranzijentna simulacija

(b) MRF (GGI)

(c) MRF (mixing plane)
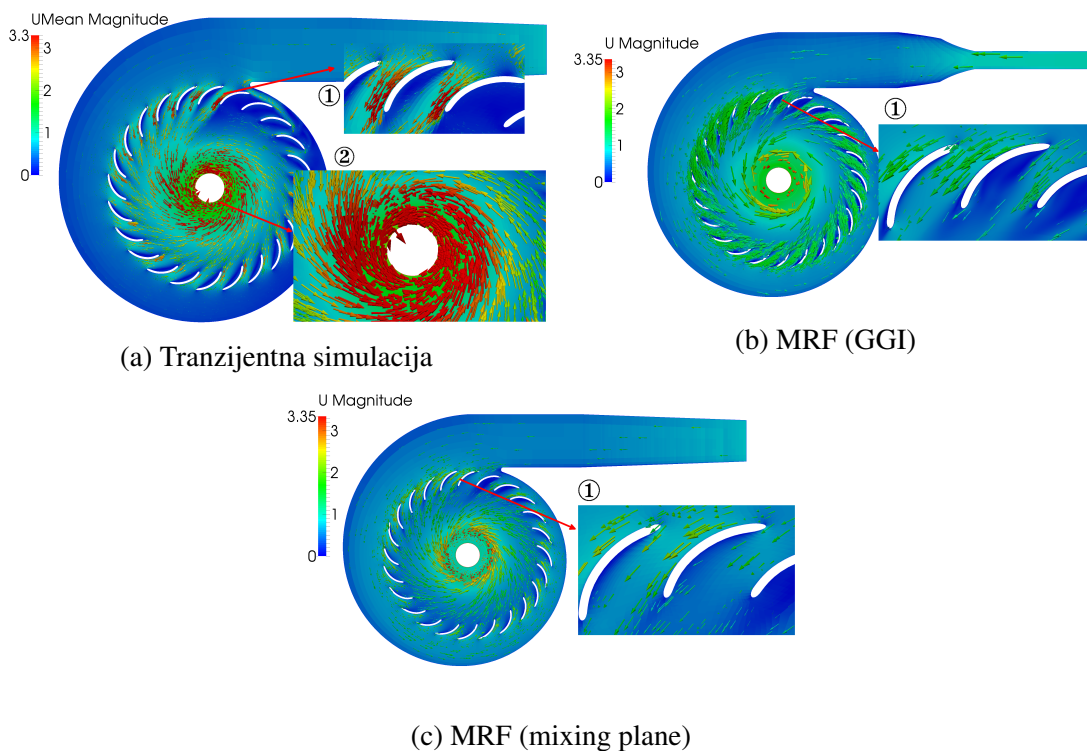
Slika 10: Usporedba polja brzine u zoni statora.

(a) Tranzijentna simulacija

(b) MRF (GGI)

(c) MRF (mixing plane)
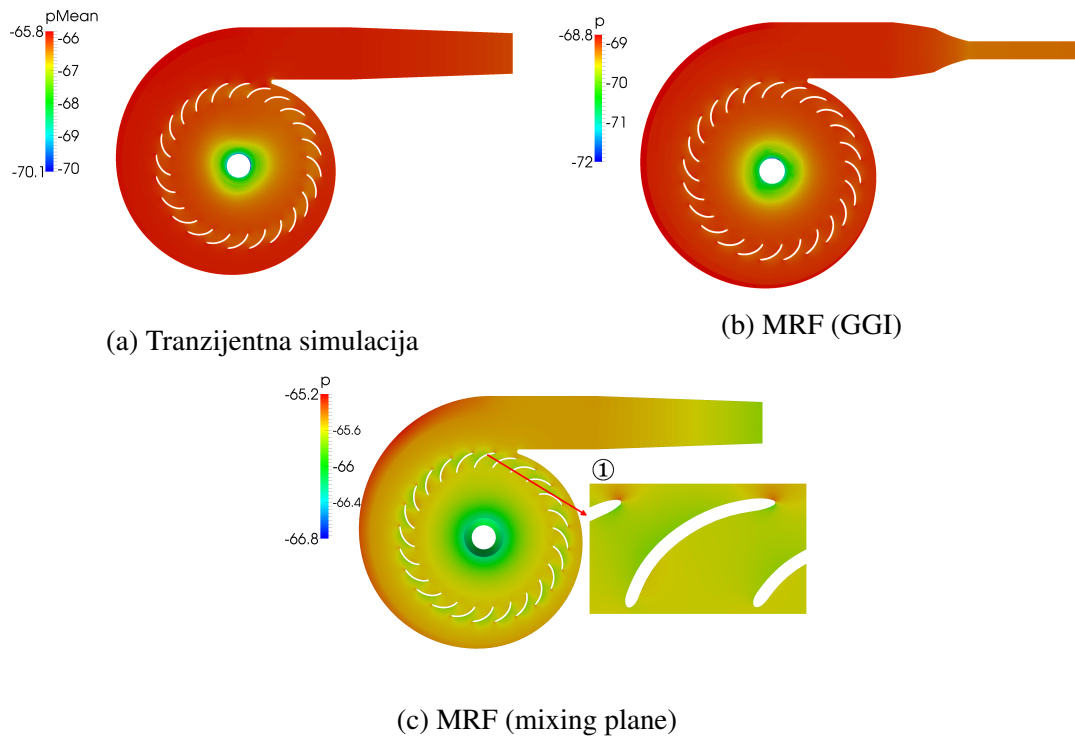
Slika 11: Usporedba polja tlaka u zoni statora.

Zona rotora ima veći utjecaj na rezultate dobivene simulacijom te je mreža u zoni rotora veće rezolucije. Na slici 12 prikazano je polje brzine u zoni rotora dobiveno različitim modelima simulacije. Detalji slika prikazuju detalj polja oko napadnog i izlaznog brida lopatice. Na slici 13 je prikazana usporedba polja tlaka u zoni statora. Detalji također prikazuju raspodjelu tlaka na napadnom i izlaznom bridu rotorskih lopatica.

(a) Tranzijentna simulacija

(b) MRF (GGI)

(c) MRF (mixing plane)
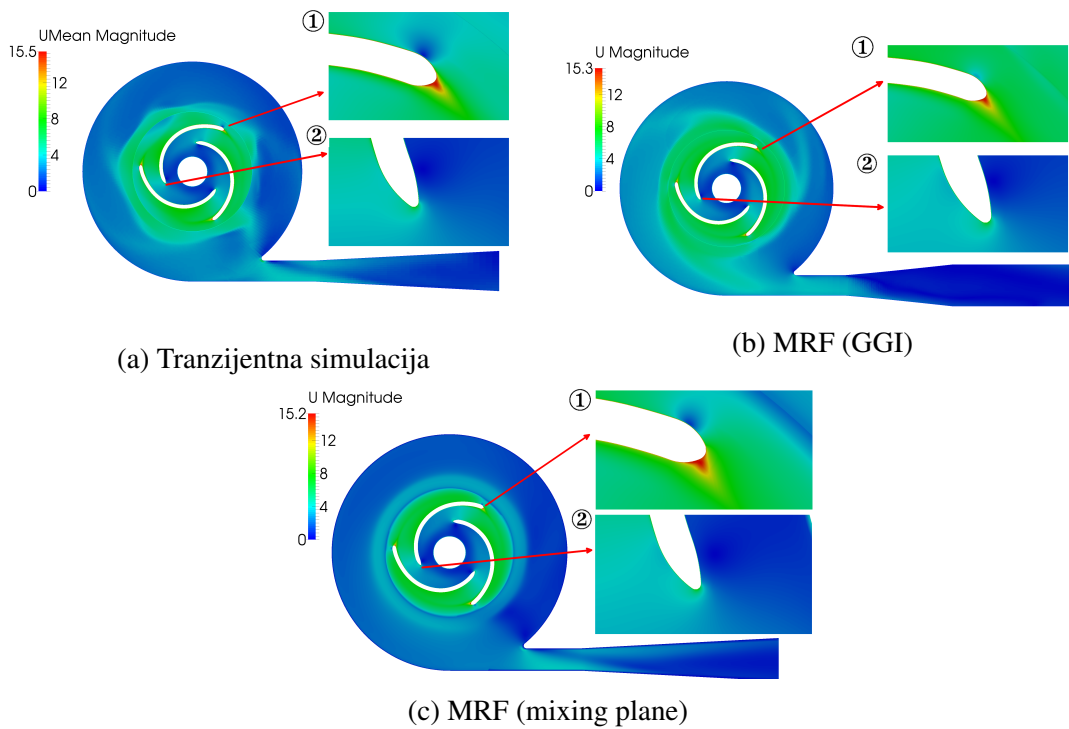
Slika 12: Usporedba polja brzine u zoni rotora.

(a) Tranzijentna simulacija

(b) MRF (GGI)

(c) MRF (mixing plane)
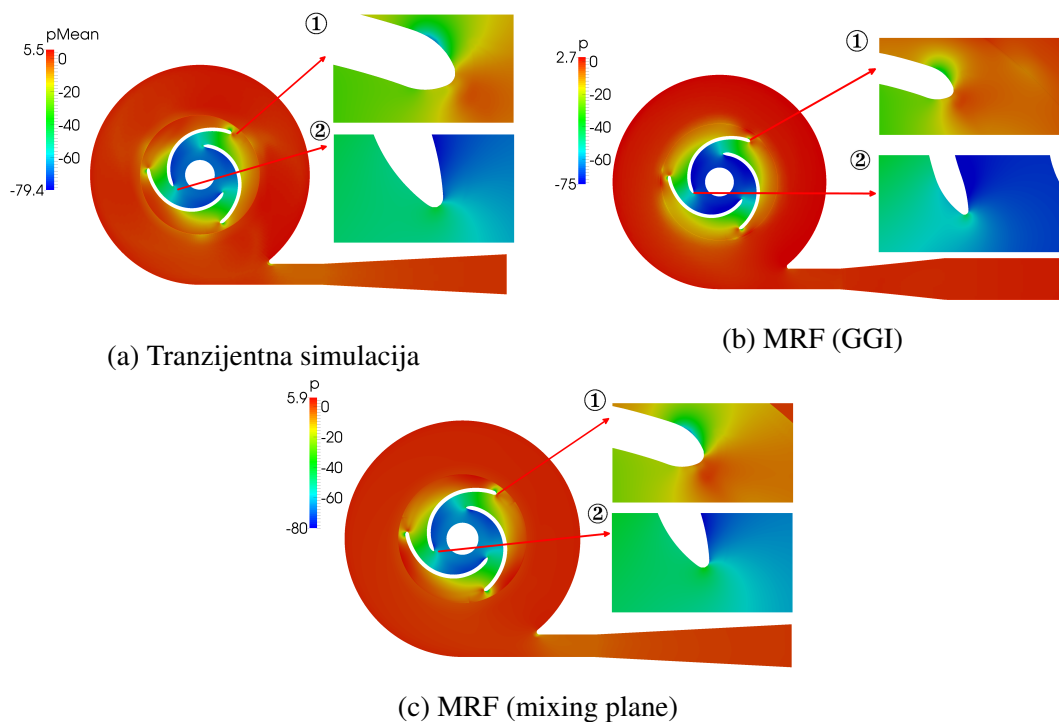
Slika 13: Usporedba polja tlaka u zoni rotora.

Rezultati su uspoređeni pod pretpostavkom da je tranzijentna simulacija najtočnija, a podaci su prikazani u tablici 2. Vidljivo je da rezultati obje simulacije daju dobra rješenja, uz iznimku iskoristivosti kod MRF simulacije kod koje se kao sučelje koristi GGI. Dodatno je zanimljivo

da se rezultati simulacije s mixing plane sučeljem bolje poklapaju s tranzijentnom simulacijom od simulacije s GGI sučeljem. Da prikaz rezultata bude konzistentan, radna karakteristika je i ovdje napravljena pomoću dobivenih rezultata iz MRF simulacije kod koje se kao sučelje koristi GGI, što je prikazano na slici 14. Radne točke pumpe koje su simulirane za izradu radne karakteristike su definirane volumenskim protokom, a simulacije su provedene za tri radne točke. Protok prve radna točke iznosi 0,95 m^3/min, druge 0,8 m^3/min i treće 1,25 m^3/min.

Table 2: Usporedba rezultata za prvu radnu točku OTA-2 pumpe.

Simulacija	Visina dobave, m	H_{Err} , %	η , %	η_{Err} , %	Snaga, W	P_{Err} , %
Tranzijenta	6,6	-	60	-	1650	-
MRF (GGI)	7,2	-9,1	69,2	-15,3	1612,6	2,3
MRF (mixing plane)	6,7	-1,5	60,6	-1	1722,4	-4.3
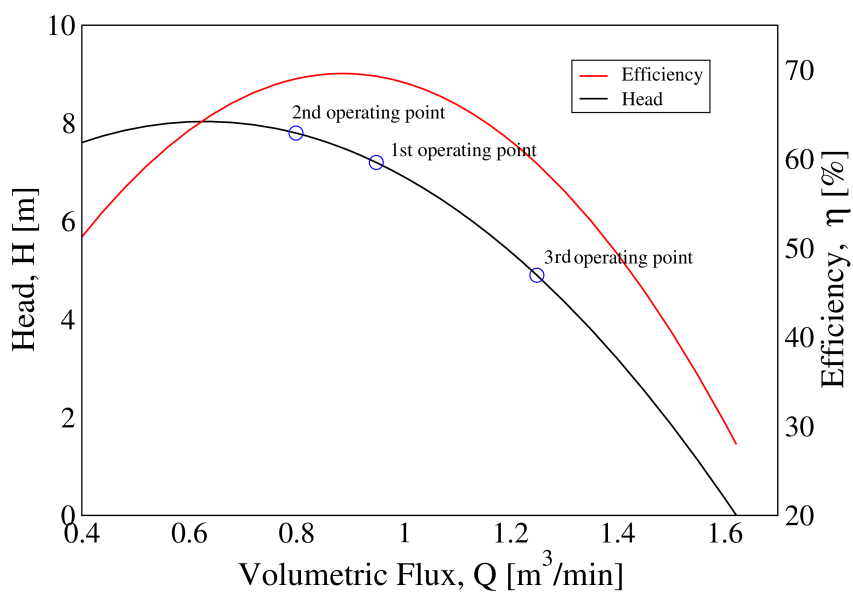
Slika 14: Radna karakteristika OTA-2 pumpe.

1 Introduction

The work presented in this thesis combines numerical simulations and turbomachinery. In first section of the thesis, topics that are important for its understanding are briefly covered. It is divided into two subsections. First subsection, named Centrifugal Pumps, deals with pumps in general. In this subsection classification of pumps and the main working principles of centrifugal pumps are explained. Second subsection, named Numerical Methods, introduces numerical models used and it also gives the general structure of this thesis.

1.1 Pumps

A pump is a device that transfers energy to an incompressible fluid enabling it to flow in a pipeline. By the mechanism they operate, pumps can be classified as volumetric and dynamic pumps. In a volumetric pump fluid is propelled by trapping a fixed amount of fluid in a chamber and forcing it into the discharge pipe. On the other hand, dynamic pumps operate according to the basic laws of turbomachinery. Most common dynamic pumps are turbopumps and they operate according to the conservation of angular momentum. In such pumps rotor and stator blades consists of airfoils what enables them desired pressure and velocity distribution in the flow.

Turbopumps can further be classified according to the application for which they are designed. Usually, this classification is made according to parameter specific speed (n_s), which is a combination of head, volumetric flux and rotational speed of the pump, as defined in [6]:

- centrifugal pumps ($n_s = 10 - 80$),

- diagonal pumps ($n_s = 80 - 160$) and

- axial pumps ($n_s = 200 - 400$),

where n_s is defined with the expression:

$$n_s = \frac{n\sqrt{Q}}{H^{\frac{3}{4}}}. \tag{1}$$

If the specific speed of pump is higher, pump is applied in the pipeline in which higher volumetric flux is required, bus lower head. From the classification can be seen that the pump with specific speeds between 160 and 200 are not manufactured due to the design reasons. Such classification also provides information about the flow in the pump. If the pump is centrifugal, flow at the inlet of the rotor is axial and radial at the outlet, while the main

direction of flow in a axial pump is in an axial direction. Diagonal pump is a combination of both axial and centrifugal pump with the axial flow at the rotor inlet, and combination of axial and radial component of the velocity at the outlet. Figure 1 shows different types of rotors according to the classification.

(a) centrifugal   (b) diagonal

(c) axial

Figure 1: Types of rotors [1]

Operating curves of pumps are usually $Q-H$, $Q-\eta$ and $Q-P$ curves, where H is head, η is the efficiency and P is the power of the pump. According to the dimensional analysis $Q-H$ and $Q-\eta$ curves can be approximated with a parabola. Operating point of pump is always positioned at the intersection of the performance curve and the pipeline curve. The latter is a function of the resistance which occurs in the pipeline and changes with a change of the volumetric flux.

1.2   Numerical methods

Optimisation of flow in centrifugal pumps is often performed using Computational Fluid Dynamics (CFD). With the aid of CFD, pump geometry can be optimised without using expensive experiments. However, numerical simulations are an approximation of a real flow and error in results is always present. Critical part of fluid flow assumption in pumps is the rotor-stator interface treatment which is used to couple rotor and stator zone into a single domain on a matrix level. Selection of rotor-stator interface treatment used in flow simulation

effects accuracy and time required to perform numerical simulation. In this thesis effects of different rotor-stator interface treatments on simulation results are presented. All simulations are performed using foam-extend, a community driven fork of open-source CFD software, OpenFOAM [7].

In this thesis, four different types of simulations are performed and compared:

- *multiple frames of reference* (MRF) with *general grid interface* (GGI) between rotor and stator zone,

- *multiple frames of reference* with *mixing plane* interface between rotor and stator zone,

- transient simulation with dynamic mesh and time averaged results and

- *harmonic balance method.*

Multiple frames of reference model is a steady state approximation of transient flow, which enables steady state simulation of turbomachinery by ignoring transient phenomena. Rotation of the rotor in MRF is taken into account with the additional terms in mathematical model, such as centrifugal and Coriolis term without the dynamic mesh. Harmonic balance method is a quasi steady-state model which enables calculation of results in specific time instances of transient flow using a steady-state formulation. This is only possible with assumption that the flow is periodic and that each primitive variable can be accurately represented by a Fourier series in time. Due to complex geometries of turbomachinery numerical spatial domains are often made from more parts merged together. This often leads to non-conformal cell zones of rotor and stator. Simulations with dynamic mesh generates a non-conformal mesh even if, for the starting position of the moving domain, the whole mesh was conformal. In this thesis, interfaces used for joining multiple non-conformal domains are GGI and mixing plane interface [3], [4].

Introduced numerical models are applied on two centrifugal pump geometries. The first pump is a double-suction in-line horizontal pump (OTA-1) and the second is a vertical pump with guiding stator blades in a section before the rotor (OTA-2). Steady state simulation including MRF model with GGI between rotor and stator and transient simulation with dynamic mesh are performed for three different operating points and for every operating point pump head, power and efficiency are calculated. The remaining two models, MRF with mixing plane interfaces and the harmonic balance method, are simulated only for operating point with maximum efficiency.

$Q - H$ and $Q - \eta$ performance curves are approximated by a parabola defined with three operating points. Parameters which define those operating points were obtained from the MRF simulation with the GGI between rotor and stator.

1.3   Thesis Outline

The main goal of this thesis is comparison of results for different simulation models, taking into account both accuracy and simulation time on real industrial pump geometries. The work covered by the thesis is divided into sections as follows: Section 2, named Mathematical Model, deals with partial differential equations used and mathematical aspects of interface treatment between rotor and stator. Section 3, named Finite Volume Discretisation, deals with discretisation of scalar transport equation and pressure-velocity coupling algorithms. Section 4, Geometry and Numerical Spatial Domain, deals with pump geometries and mesh generation process for both pumps. In section 5, results obtained from numerical simulations are presented and compared with results from transient simulation, which is assumed to be most accurate. Conclusion of the thesis is given in section 6.

2   Mathematical Model

Flow in pumps can be modelled with incompressible Navier-Stokes equations due to low Mach number. In most flows through pumps Mach number is below 0.1 and compressibility of the fluid can be ignored. Modified Navier-Stokes equations, where the velocity is specified in a rotatiing coordinate system, contain additional terms connected with rotational motion, such as Coriolis and centrifugal forces. These terms are defined by angular velocity and radius of the fluid particle from axis of rotation.

2.1   Introduction

This section deals with mathematical models used in different steady state simulations. In this thesis, two main steady state models are used. The first model is Multiple reference frames model, while the second is the harmonic balance method. In order to describe these models, in first subsection general scalar transport equation and its physical meaning are presented. The second subsection deals with Multiple reference frames model and modification of Navier-Stokes equations for turbomachinery simulations. The third subsection explains Fourier transformation and describes the way harmonic balance method is implemented in Navier-Stokes equations. The final subsection explains rotor-stator interaction models used to connect multiple mesh regions.

2.2   Governing Equations of Fluid Flow

Scalar transport equation models a combination of convection and diffusion transport of scalar [8]. Equation in standard form can analytically be expressed as:

$$\frac{\partial \Phi}{\partial t} + \nabla \cdot (\mathbf{u}\Phi) - \nabla \cdot (\gamma \nabla \Phi) = q_v, \tag{2}$$

where Φ is the transported scalar variable, $\mathbf{u}$ is the convective velocity and γ is the diffusion coefficient. The term on right hand side of Eq. (2) represents sources or sinks of the transported scalar Φ. Sources and sinks account for non-transport effects such as local volume production and destruction of Φ. In standard form of scalar transport equation four characteristic terms are present:

- term $\dfrac{\partial \Phi}{\partial t}$ is the temporal derivative of transported scalar which represents inertia of the system,

- term $\nabla \cdot (\mathbf{u}\Phi)$ is the convection term which represents the convective transport of scalar Φ by the velocity field $\mathbf{u}$,

- term $\nabla \cdot (\gamma \nabla \Phi)$ is the diffusion term which represents transport of scalar Φ based on its spatial gradient and diffusivity γ and

- term q_v represents sources and sinks od transported scalar Φ.

Diffusion of a transported scalar variable is elliptic: every point in the domain feels the influence of every other point instantaneously. On the other hand, convection of a transported scalar variable is hyperbolic term: information comes from the vicinity, defined by the direction of the convection velocity $\mathbf{u}$ [8].

2.2.1 Conservation of Mass

Conservation of mass is derived from a scalar transport equation Eq. (2) by substituting the transported scalar variable Φ with the density of fluid ρ and setting the source term to zero as shown in Eq. (3).

$$\frac{\partial \rho}{\partial t} + \nabla \cdot (\rho \mathbf{u}) = 0 \tag{3}$$

In incompressible flow density of fluid is constant and Eq. (3) can be written as:

$$\nabla \cdot \mathbf{u} = 0. \tag{4}$$

2.2.2 Conservation of Linear Momentum

Conservation of linear momentum is derived from a scalar transport equation Eq. (2) by substituting the transported scalar field Φ with the product of fluid density and velocity, $\rho \mathbf{u}$. Linear momentum $\rho \mathbf{u}$ is a vector, therefore conservation of linear momentum can be divided into three scalar differential equations, each for one spatial component of velocity vector. The source and sink term is equal to sum of mass $\rho \mathbf{g}$ and body forces $\nabla \cdot \sigma$.

$$\frac{\partial \rho \mathbf{u}}{\partial t} + \nabla \cdot (\rho \mathbf{u} \otimes \mathbf{u}) = \rho \mathbf{g} + \nabla \cdot \sigma \tag{5}$$

For incompressible flow Eq. (5) can be written as:

$$\frac{\partial \mathbf{u}}{\partial t} + \nabla \cdot (\rho \mathbf{u} \otimes \mathbf{u}) - \nabla \cdot (\nu \nabla \mathbf{u}) = -\nabla p, \tag{6}$$

where p is the kinematic pressure, ν is the kinematic viscosity and $\mathbf{g}$ is gravitational acceleration. In Eq. (5), σ is the Cauchy stress tensor. Additionally, to derive the momentum equation used in mathematical models of a pump flow, mass forces have to be ignored.

Velocity **u** in the equation for conservation of linear momentum is both the transported and the transporting variable: therefore convective term is non-linear.

2.2.3 Conservation of Energy

Conservation of energy is derived from the scalar transport equation Eq. (2) by substituting the transported scalar field Φ with product of fluid density and specific internal energy, ρe. The source and sink term is equal to sum of power of mass forces $\rho \mathbf{g} \cdot \mathbf{u}$, power of body forces $\nabla \cdot (\sigma \cdot \mathbf{u})$ and heat flux $(-\nabla \cdot \mathbf{q} + \rho Q)$.

$$\frac{\partial \rho e}{\partial t} + \nabla \cdot (\rho e \mathbf{u}) = \rho \mathbf{g} \cdot \mathbf{u} + \nabla \cdot (\sigma \cdot \mathbf{u}) - \nabla \cdot \mathbf{q} + \rho Q \tag{7}$$

In Eq. (7) e is specific energy, $\mathbf{q}$ is heat flux and Q is volumetric heat source. Conservation of energy is not used in mathematical model used to simulate turbomachinery in this thesis, because distribution of temperature in the flow is not observed.

2.3 Turbulence Models

Turbulence models are used to obtain physical results without the need for cells to have the size of smallest turbulence scale in order to resolve the turbulent phenomena. Solution caused by turbulence are in many engineering applications not desirable due to fluctuation of primitive variables value. Instead of small turbulent fluctuations, mean values of correlated variables are of interest. For most engineering applications Reynolds averaging is the method used to separate primitive variables of pressure and velocity in a turbulent flow into mean value and fluctuating parts. All the fluctuating values are assembled into the term called Reynolds stress tensor and turbulence models are used to model fluctuating values of turbulent flow. Velocity and pressure in a turbulent flow can be expressed as:

$$\mathbf{u} = \overline{\mathbf{u}} + \mathbf{u}', \tag{8}$$

and

$$p = \overline{p} + p', \tag{9}$$

where $\overline{\mathbf{u}}$ and $\overline{p}$ are mean values of velocity and pressure, while the fluctuating parts of velocity and pressure are $\mathbf{u}'$ and p'. If the expressions Eq. (8) and Eq. (9) are substituted into the Navier-Stokes set of equations, set of equations governing incompressible turbulent flow is obtained:

$$\frac{\partial \overline{\mathbf{u}}}{\partial t} + \nabla \cdot (\overline{\mathbf{u}}\,\overline{\mathbf{u}}) - \nabla \cdot (\nu \nabla \overline{\mathbf{u}}) = -\nabla \overline{p} + \nabla \cdot (\overline{\mathbf{u}'\mathbf{u}'}) \tag{10}$$

$$\nabla \overline{\mathbf{u}} = 0. \tag{11}$$

In equation Eq. (10), term $\overline{\mathbf{u}'\mathbf{u}'}$ is the Reynolds stress tensor depending on fluctuating variables of turbulent flow. The Reynolds stress tensor is a symmetrical second order tensor which consists of six additional unknowns. The system represented by Eq. (10) and Eq. (13) has more unknowns than it has equations and in such form it cannot be solved. Turbulence models based on Bousinessq hypothesis are used to model the Reynolds stress tensor with only mean value of velocity gradient:

$$\overline{\mathbf{u}'\mathbf{u}'} = \nu_t\, \frac{1}{2}\left[\nabla \overline{\mathbf{u}} + (\nabla \overline{\mathbf{u}})^T\right], \tag{12}$$

where ν_t is turbulent viscosity which is defined as:

$$\nu_t = A\, U\, \Delta, \tag{13}$$

where A is a dimensionless constant that allows tuning of the model to the actual physical behaviour. In Eq. (13), U is the velocity scale and Δ is the length scale. Velocity scale can be approximated with fluctuating part of velocity $\mathbf{u}'$. In all turbulence models it is required to model both velocity scale in form of a turbulent kinetic energy and additionaly a representative length scale. Turbulent kinetic energy is defined with following expression:

$$k = \frac{3}{2}\mathbf{u}'^2. \tag{14}$$

Benefits of Reynolds Averaged Navier Stokes models (RANS) is that turbulent flow doesn't have to be simulated in a transient way. Hence, spatial resolution is no longer governed by the Kolmogorov scale which defines the size of the smallest vortex appearing in a flow. Smallest vortex is defined as the vortex that doesn't have enough kinetic energy to perform full revolution and it is dissipated into heat. If a turbulent flow is simulated in a transient way, smallest cell in a numerical spatial domain has to be smaller than the smallest vortex appearing in a flow and the time step is defined with the greatest frequency of the vortices, making Direct Numerical Simulation prohibitively expensive for most engineergin purposes.

In this thesis for all simulations the $k - \omega\ SST$ model is used, except for the harmonic balance method simulation where the $k - \varepsilon$ model is used.

2.3.1 Incompressible $k - \varepsilon$ Turbulence Model

The $k - \varepsilon$ model is a two equation turbulence model that consists of the equation for turbulent kinetic energy k, as shown in Eq. (15), and the equation for turbulent dissipation ε, as shown in Eq. (16) [9].

$$\frac{\partial k}{\partial t} + \nabla \cdot (\overline{\mathbf{u}}k) - \nabla \cdot \left[\nu_{eff} \, \nabla k \right] = \nu_t \left[\frac{1}{2}(\nabla \overline{\mathbf{u}} + (\nabla \overline{\mathbf{u}})^T \right]^2 - \varepsilon. \tag{15}$$

$$\frac{\partial \varepsilon}{\partial t} + \nabla \cdot (\overline{\mathbf{u}}\varepsilon) - \nabla \cdot \left[\nu_{eff} \, \nabla \varepsilon \right] = C_1 \, G \, \frac{\varepsilon}{k} - C_2 \frac{\varepsilon^2}{k}. \tag{16}$$

The $k - \varepsilon$ turbulence model introduces two extra partial differential equations into mathematical model used to simulate turbulent fluid flow. Turbulent viscosity in the $k - \varepsilon$ turbulence model is defined as:

$$\nu_t = C_\nu \frac{k^2}{\varepsilon}. \tag{17}$$

Reader is reffered to [Launder Spalding] for details regarding modelling constants.

2.3.2 Incompressible $k - \omega$ SST Turbulence Model

The $k - \omega$ SST turbulence model is a two equation turbulence model consisting of the turbulent kinetic energy equation and the equation for a specific dissipation ω [9]. In the $k - \omega$ SST model turbulent kinetic energy equation reads:

$$\frac{\partial k}{\partial t} + \nabla \cdot (\overline{\mathbf{u}}k) - \nabla \cdot \left[\nu_{eff} \, \nabla k \right] = \min(G, C_1 \, \beta^* \, k\omega) - \beta * k\omega. \tag{18}$$

Specific dissipation rate equation reads:

$$\frac{\partial \omega}{\partial t} + \nabla \cdot (\overline{\mathbf{u}}\omega) - \omega \nabla \cdot \overline{\mathbf{u}} - \nabla \cdot (\nu_{eff} \nabla \omega) =$$
$$\gamma \min \left[S_2, \frac{c_1}{a_1} \beta^* \, \omega \, \max(a_1 \omega, b_1 F_{23} \sqrt{S_2} \right] \tag{19}$$
$$- \beta \omega^2 + (1 - F_1) CD_{k\omega}.$$

Turbulent viscosity is calculated as:

$$\nu_t = \frac{a_1 k}{max \left[a_1 \omega, b_1 F_{23} \sqrt{2} \left| \frac{1}{2}(\nabla \overline{\mathbf{u}} + (\nabla \overline{\mathbf{u}})^T \right| \right]}. \tag{20}$$

The $k - \omega$ *SST* turbulence model combines the best properties of both $k - \omega$ model by Wilcox and the $k - \varepsilon$ model [9]. The $k - \varepsilon$ model is used in free stream where $k - \omega$ is sensitive to the initial values of k and ω parameters. In proximity of the wall, the $k - \omega$ model is used. This allows usage of turbulence models without the near-wall damping functions if the mesh provides sufficient near-wall resolution to capture the viscous subaltern of the turbulent boundary layer. All the constants in differential equations of the $k - \omega$ *SST* model are used to tune the model to actual physical behaviour, while the reader is reffered to [Menter] for details.

2.4 Multiple Reference Frame

Multiple Reference Frame (MRF) model is a steady-state approach for turbomachinery simulations. In this model, each zone can be assigned different rotational velocity. The flow for each moving zone is solved using the moving reference frame equations. If the zone is assigned velocity equal to zero, the equations are reduced to their stationary form in the inertial frame of reference. Regardless of the assigned velocity, numerical mesh remains fixed for the whole domain. This is analogous to "freezing" the motion of the moving part in a specific position and observing the flow for that position. Because of that, MRF model is often called "frozen rotor approach" [10].

Despite the MRF being only an approximation of transient flow, it can provide reasonable numerical results of flow in turbomachinery. Another potential use of the MRF model is to compute a flow field that can be used as an initial condition for a transient flow simulation with a dynamic mesh. However, if it is necessary to simulate transient phenomena that may occur in rotor-stator interactions, transient simulation with a dynamic mesh should be performed.

2.4.1 Incompressible Navier-Stokes Equations in the Rotating Frame

For every cell zone that has been assigned a rotational velocity different from zero, Navier-Stokes equations used to solve incompressible flow have to be modified. For a general vector $\mathbf{A}$ in the inertial reference frame, following can be expressed:

$$\left[\frac{d\mathbf{A}}{dt}\right]_I = \left[\frac{d\mathbf{A}}{dt}\right]_R + \omega \times \mathbf{A}, \tag{21}$$

where ω is the angular velocity vector. If general vector $\mathbf{A}$ is substituted with the position vector $\mathbf{r}$, Eq. (21) is transformed into:

$$\left[\frac{d\mathbf{r}}{dt}\right]_I = \left[\frac{d\mathbf{r}}{dt}\right]_R + \omega \times \mathbf{r}. \tag{22}$$

Differentiation of position vector equals velocity and Eq. (22) can be written in following way:

$$\mathbf{u}_I = \mathbf{u}_R + \omega \times \mathbf{r}. \tag{23}$$

Further differentiation of Eq. (22) results in expression for acceleration in inertial reference frame. This expression in standard form is shown by Eq. (24).

$$\left[\frac{d\mathbf{u}_I}{dt}\right]_I = \left[\frac{d\mathbf{u}_R}{dt}\right]_R + \frac{d\omega}{dt} \times \mathbf{r} + 2\omega \times \mathbf{u}_R + \omega \times \omega \times \mathbf{r} \tag{24}$$

Three characteristic terms are present on the right hand side of Eq. (24):

- term $\frac{d\omega}{dt} \times \mathbf{r}$ is the tangential acceleration,

- term $2\omega \times \mathbf{u}_R$ is the Coriolis acceleration,

- and term $\omega \times \omega \times \mathbf{r}$ is the centrifugal acceleration.

By taking into account Eq. (24) for the acceleration term, Navier-Stokes equations for incompressible flow with kinematic viscosity and with respect to inertial reference frame can be written:

$$\frac{d\mathbf{u}_I}{dt} + \nabla \cdot (\mathbf{u}_I \otimes \mathbf{u}_I) = -\nabla p + \nabla \cdot (\nu \nabla \mathbf{u}_I) \tag{25}$$

$$\nabla \cdot \mathbf{u}_I = 0, \tag{26}$$

where Eq. (25) represents the momentum equation and Eq. (26) the continuity equation. If this set of equations is adjusted for relative reference frame we get a set of equations used in the MRF model [11]:

$$\frac{d\mathbf{u}_R}{dt} + \omega \times \mathbf{u}_I + \nabla \cdot (\mathbf{u}_R \otimes \mathbf{u}_I) = -\nabla p + \nabla \cdot (\nu \nabla \mathbf{u}_I), \tag{27}$$

$$\nabla \cdot \mathbf{u}_I = 0. \tag{28}$$

2.5 Harmonic Balance Method

Harmonic balance method is a quasi steady-state method developed for simulations of non-linear and temporally periodic flows [2]. The main assumption in this method is that each primitive variable can be accurately represented by a Fourier series in time, using first *n* harmonics and the mean value [2]. Such assumption allows replacing the time derivative term in transport equation with additional source terms. Because of that, the harmonic balance method consists of coupled set of steady-state equations, while being able to describe transient

effects of the periodic flow. In harmonic balance method the snapshots of a flow field in certain time steps within one period are obtained and other time steps can be reconstructed as a post processing step.

Harmonic balance can be used in turbomachinery simulations where the influences of wakes, generated by rotation of rotor, passing to the stator can be resolved without the need of conventional transient simulation with dynamic mesh [2].

2.5.1 Fourier Series Expansion

Fourier series expansion is used to represent any periodic function as a sum of infinite series of sine and cosine functions [2]. Every sine or cosine function can have a different amplitude and frequency, allowing their sum to closely approximate the original function.

If $f(x)$ is arbitrary periodic function of variable x and it is integrable on an interval $[x_0, x_0 + P]$, where P is the period of the $f(x)$, then this function can be written using Fourier expansion as:

$$f(x) = a_0 + \sum_{n=1}^{\infty} \left(a_n cos \left(\frac{2\pi nx}{P} \right) + b_n sin \left(\frac{2\pi nx}{P} \right) \right), \tag{29}$$

where a_n and b_n are called Fourier coefficients which can be calculated if a function $f(x)$ is known. Mathematical definition of Fourier coefficients reads:

$$a_n = \frac{2}{P} \int_{x_0}^{x_0+P} f(x) cos \left(\frac{2\pi nx}{P} \right) dx, \tag{30}$$

$$b_n = \frac{2}{P} \int_{x_0}^{x_0+P} f(x) sin \left(\frac{2\pi nx}{P} \right) dx. \tag{31}$$

Expression Eq. (29) shows that the sum of expansion has infinite number of terms which is inconvenient for practical use. Because of that, in every Fourier transformation the error is introduced by reducing the number of sine and cosine terms to a finite value.

To obtain a satisfactory results with reasonable calculation time, a suitable number of terms should be chosen as shown in Eq. (32).

$$f(x) = a_0 + \sum_{n=1}^{N} \left(a_n cos \left(\frac{2\pi nx}{P} \right) + b_n sin \left(\frac{2\pi nx}{P} \right) \right), \tag{32}$$

where N represents desired number of harmonics. If the desired number of harmonics is equal to zero, function $f(x)$ is approximated only with term a_0 which represents the mean value. In general, expansion of function $f(x)$ with N harmonics will have $2N + 1$ terms:

- N sine terms,

- *N* cosine terms,

- and a mean value a_0.

Amplitude of *n*th harmonic can be expressed as:

$$A_n = \sqrt{a_n^2 + b_n^2},$$ (33)

and the square of the amplitude A_n^2 stands for energy of *n*th harmonic.
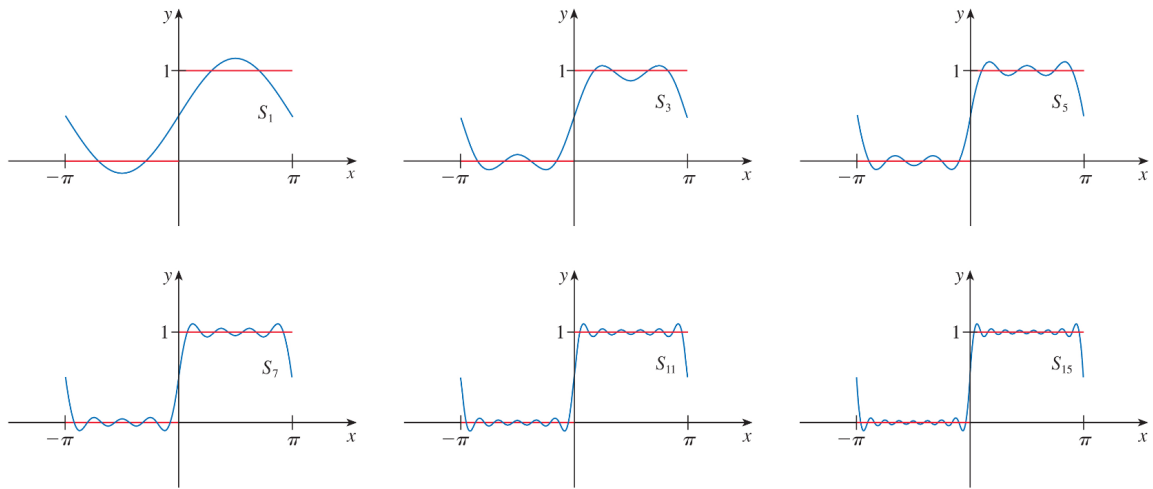
Figure 2: Fourier expansion of a step function [2].

Graphical example of Fourier expansion with different number of harmonics of a step function is shown on Figure 2. It can be seen that higher number of harmonics used for Fourier expansion results in closer approximation of step function. The example is given for approximation with 1, 3, 5, 7, 11 and 15 harmonics.

2.5.2 Harmonic Balance Method for a Scalar Transport Equation

Scalar transport equation in the standard form is shown by Eq. (2). Convection, diffusion and source/sink terms can be combined and Eq. (2) can be written in following way:

$$\frac{\partial \phi}{\partial t} + \Re = 0,$$ (34)

where $\Re$ is:

$$\Re = \nabla \cdot (\mathbf{u}\phi) - \nabla(\gamma \nabla \cdot \phi) - q_v.$$ (35)

The Fourier expansion for ϕ for desired number of harmonics, *n*, reads:

$$\phi = \varphi_0 + \sum_{i=1}^{n} \varphi_{s_i} sin(i\omega t) + \varphi_{c_i} cos(i\omega t). \tag{36}$$

In Eq. (36), φ is frequency domain field, ϕ is time domain field and ω is a base radian frequency. Expanding $\Re$ into Fourier series is done in analogous way, substituting φ in Eq. (36) with R. If ϕ and $\Re$ in Eq. (34) are substituted for their Fourier series, Eq. (34) yields sine, cosine and mean terms. This way, scalar transport equation is transformed in $2n + 1$ equations:

- 1 equation for mean value term,

- n equations for sine terms

- and n equations for cosine terms.

This set of equations can be written in matrix form as:

$$\omega \mathbf{A} \varphi + \mathbf{R} = 0. \tag{37}$$

In Eq. (37) φ is a column vector consisting of φ_{s_i} and φ_{c_i} Fourier coefficients and $\mathbf{R}$ is a column vector consisting of R_{s_i} and R_{c_i} Fourier coefficients. $\mathbf{A}$ is a $(2n+1) \times (2n+1)$ coefficients matrix containing coefficients from both φ and $\mathbf{R}$ column vectors.

Switching between time and frequency domain is done using a matrix representation of Discrete Fourier Transformation (DFT). Conversion from time domain vector ϕ and frequency domain vector φ can be expressed in a matrix form as:

$$\hat{\varphi} = \mathbf{E} \, \hat{\phi}, \tag{38}$$

Hat symbol is used to label discrete variables. In Eq. (38), $\hat{\phi}$ is discrete time domain vector needed for unique one-to-one mapping:

$$\hat{\phi}^T = [\phi_{t_1} \ \phi_{t_2} \ \phi_{t_3} \ ... \ \phi_{t_{2n+1}}]. \tag{39}$$

Multiplying Eq. (38) with matrix E^{-1}, mapping from the frequency domain to time domain is obtained:

$$\hat{\phi} = \mathbf{E} \, \hat{\varphi}. \tag{40}$$

Using the forward and backward transformation matrices $\mathbf{E}$ and $\mathbf{E}^{-1}$, the frequency domain scalar transport equation is formulated using the discrete time domain vector $\hat{\phi}$:

$$\omega \mathbf{E} \mathbf{A} \hat{\phi} + \mathbf{E} \hat{\Re} = 0. \tag{41}$$

In Eq. (41) time-derivative term is transformed into source term. Even though equations could be solved in this form, evaluating sources and fluxes in the frequency domain is computationally expensive and inconvenient. Because of that Eq. (41) is multiplied by the transformation matrix $\mathbf{E}^{-1}$ from the left:

$$\omega \mathbf{E} \mathbf{A} \mathbf{E}^{-1} \hat{\phi} + \hat{\mathfrak{R}} = 0. \tag{42}$$

Comparing Eq. (42) with the original scalar transport equation two important differences are present [12]:

- Continuous function $\mathfrak{R}$ is replaced with a discrete function $\hat{\mathfrak{R}}$. This indicates that the solution is calculated only at a fixed number of discrete time instances. Number of discrete time instances are defined by the desired number of harmonics.

- Time derivative term is replaced by terms that couple the solution at different time steps.

The expanded form of Eq. (42) can be written in following way:

$$\nabla \cdot (\mathbf{u} \phi_{t_j}) - \nabla \cdot (\gamma \nabla \phi_{t_j}) = -\frac{2\omega}{2n+1} \left(\sum_{i=1}^{2n} P_{i-j} Q_{t_i} \right), \tag{43}$$

$$\text{for } j = \{1, \, 2, \, ... \, 2n+1\},$$

where P_i is:

$$P_i = \sum_{k=i}^{n} k \sin(ik\omega\Delta t), \tag{44}$$

$$\text{for } i = \{1, \, 2, \, ... \, 2n+1\},$$

and Δt is:

$$\Delta t = \frac{T}{2n+1}. \tag{45}$$

2.5.3 Harmonic Balance Method for Navier-Stokes equations

As previously presented, harmonic balance transforms time derivative term into set of coupled source terms while convection and diffusion terms stay unchanged. Continuity equation remains the same as it doesn't contain the time derivative term [12]:

$$\nabla \cdot \mathbf{u}_{t_j} = 0, \tag{46}$$

where u_{i_j} indicates that continuity equation has to be satisfied for each observed time instant. Harmonic balance form of momentum equation reads [12]:

$$\nabla \cdot (\mathbf{u}_{t_j}\mathbf{u}_{t_j}) - \nabla \cdot (\nu \nabla \mathbf{u}_{t_j}) = -\nabla p_{t_j} - \frac{2\omega}{2n+1}\left(\sum_{i=1}^{2n} P_{i-j}\mathbf{u}_{t_i}\right). \tag{47}$$

Eq. (46) and Eq. (47) represent $2n + 1$ coupled pressure-velocity systems with enforced periodic behaviour defined using the base frequency ω and number of desired harmonics n.

2.6 Rotor-Stator Interface Modelling

Geometry of turbomachinery is often complex and it is difficult to make conformal meshes of rotor and stator cell zones. Furthermore, simulations with a dynamic mesh will generate non-conformal cell zones of rotor and stator, even if these zones were conformal at the beginning of simulation. In such simulations rotor cell zone is rotating, but the mesh is not deforming. Rotation of the mesh in turbomachinery simulations requires axisymmetric interface patches. Because of that, meshes of rotor and stator are usually made separately and connected with a coupling interface. Interpolation between the pair of interface patches can be direct or averaged. In this thesis, effects on simulation results of general grid interface (GGI) and mixing plane interface are presented. Direct interpolation is present in the GGI where the flow values are interpolated directly from one interface patch to another. Interpolation in mixing plane interface is specific because it is performed by circumferential averaging of flow variables over the interface.

2.6.1 General Grid Interface

General grid interface is a coupling interface used for joining multiple non-conformal regions where the patch nodes on each side of the interface do not match [3]. It is commonly used in turbomachinery simulations, as 3D numerical meshes of such cases are mostly made of several domains which are not connected. After joining of rotor and stator cell zone into a single computational mesh, interfaces between non-conformal parts require special attention. Interfaces are handled using pairs of GGIs, whose purpose is passing of information from one patch of GGI pair to another using direct interpolation. For transient turbomachinery simulations with a dynamic mesh, the relative rotation of the rotor and stator cell zone will produce non-conformal interfaces between zones, even if the starting mesh was conformal. Non-conformal interfaces of centrifugal pumps observed in this thesis, are shown in Figure 3.
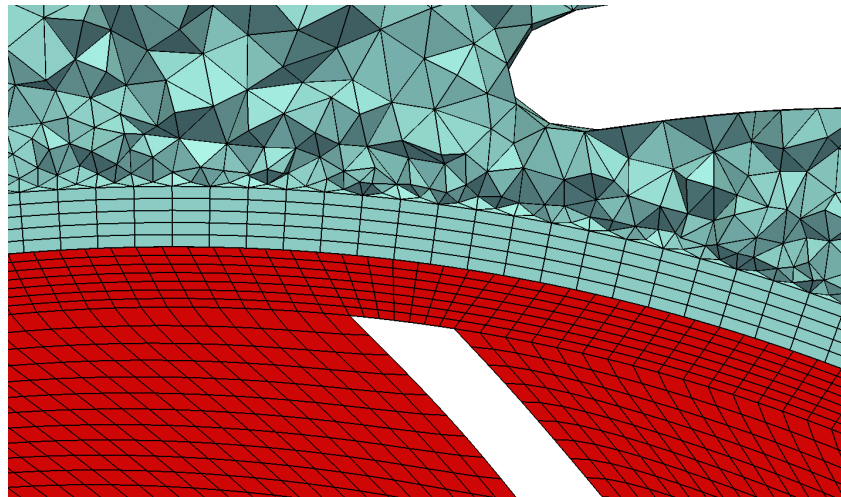
(a) OTA-1
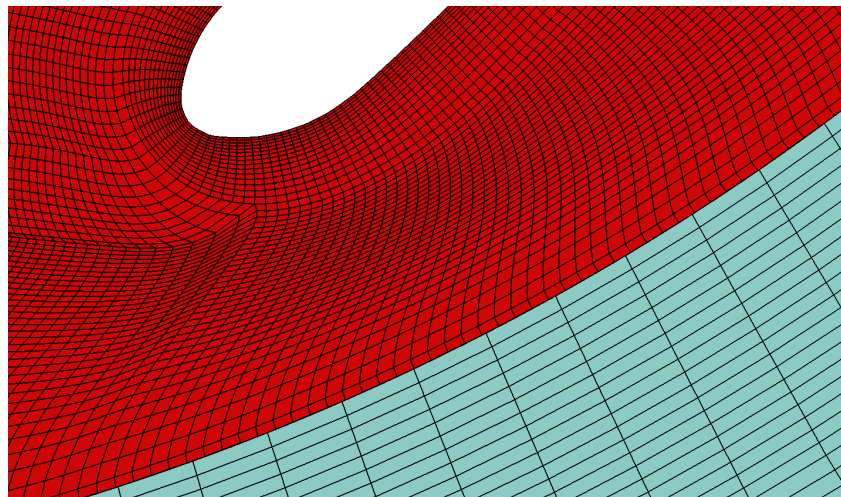
(b) OTA-2

Figure 3: GGI interface between rotor and stator cell zones.

In Subfigures 3a and 3b the rotor cell zone is coloured red, while the stator zone is coloured blue. It can be seen that meshes of rotor and stator zone are non-conformal even in simulation without dynamic mesh. Because of that, the coupling interface between rotor and stator zone is necessary. In simulated cases, where coupling interfaces are pairs of GGIs, flow values are evaluated and transmitted across a pair of non-conformal patches using weighted interpolation [3].

2.6.2 Mixing Plane Interface

The mixing plane interface is a method used for joining multiple non-conformal mesh regions. This rotor-stator interaction model is based on surface averaging of flow variables in the circumferential direction. Averaging removes unsteady phenomena created by the flow, such

as turbulent flow wakes behind individual blades. That introduces an error in numerical results, but the transient phenomena that appear in turbomachinery can be studied as a steady state problem, with the help of the MRF model [13].
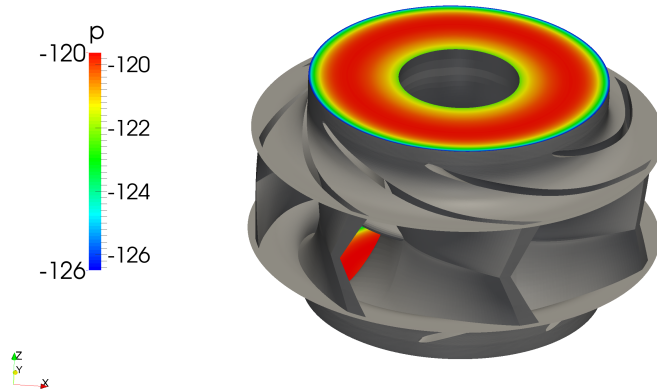
(a) Rotor-stator interface at the rotor inlet of the OTA-1 pump
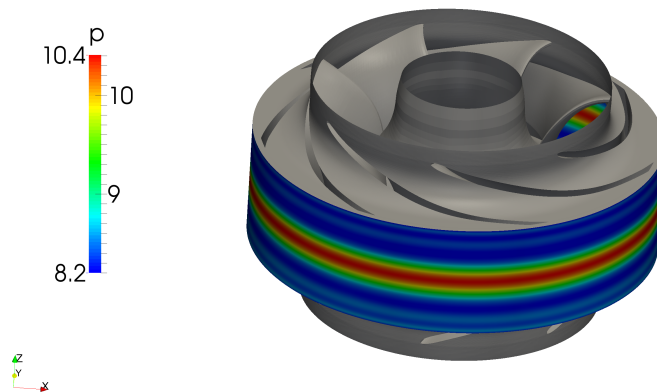
(b) Rotor-stator interface at the rotor outlet of the OTA-1 pump

Figure 4: Mixing plane interfaces with averaged pressure on the OTA-1 pump.

Figure 4 shows the distribution of pressure on interfaces between rotor and stator cell zones of OTA-1 pump. The rotor-stator interface, on the rotor inlet, can be seen in Figure 4a, where the averaging has been done in circumferential direction and the stacking of averaged bands in radial direction. Figure 4b shows a distribution of averaged pressure field on the rotor outlet. In this case the averaging of pressure has been done in circumferential direction and the stacking in direction of z axis.

2.7 Closure

This section describes the mathematical model used in the calculation of the incompressible turbulent flow in turbomachinery. Main equations are conservation of mass and conservation of linear momentum. Conservation of mass is transformed for incompressible flow into a pressure equation, while the conservation of linear momentum is a vector equation which can be divided into three scalar equations. To reduce computational resources required to solve this set of equations, turbulence models are introduced. Commonly used turbulence models are based on the Boussinesq hypothesis in which the Reynolds stress tensor is replaced with the equivalent term that contains only one unknown variable which is turbulent viscosity. To adjust the Navier-Stokes equations for turbomachinery simulation, they have to be changed in a way that rotation of a fluid in a rotor zone is taken into account. For the purposes of the simulations presented in the thesis, the MRF model and the transient simulation with a dynamic mesh are used. If the rotor and stator cell zones are non-conformal it has to be specified how are the flow variables transported from the stator zone to the rotor zone and vice versa. Commonly used rotor-stator interfaces are GGI and mixing plane whose effect on the results will be presented in the following sections.

3   Finite Volume Method

Majority of solvers implemented in OpenFOAM rely on the finite volume method for spatial and temporal discretisation.   Discretisation is a process of numerically approximating governing partial differential equation, that has to be solved, by a set of algebraic equations of equivalent properties. In OpenFOAM, operators are present in two forms:

- Calculus operators which operate directly on a given field and

- Method operators which create a set of matrix coefficients for a given implicit discretisation.

For a discretisation process, spatial and time domain have to be defined. Spatial domain is defined by a numerical mesh, while the time domain is defined by simulation time-steps representing the time interval. Spatial domain consists of a finite number of polyhedral control volumes.
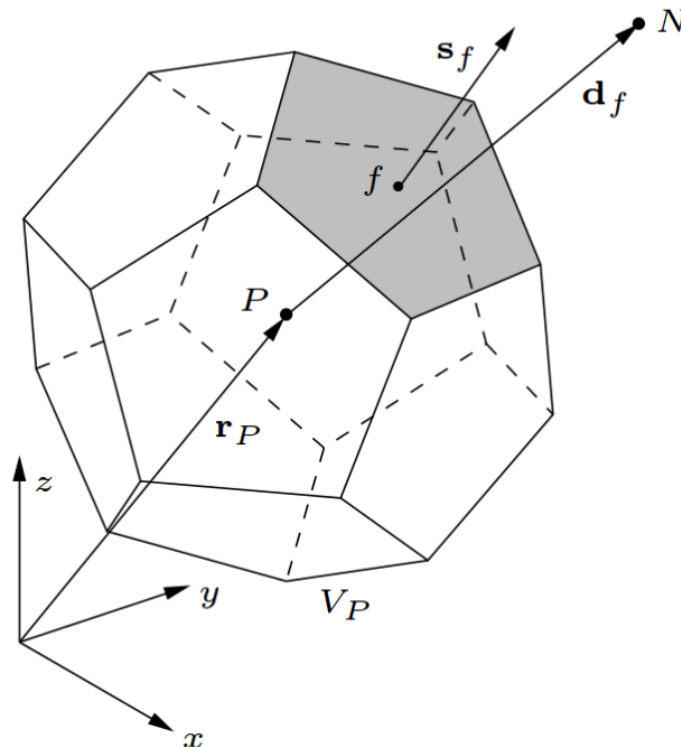

Figure 5: Polyhedral finite volume.

General convex polyhedral finite volume is shown in Figure 5. Point P is the computational point located at the cell centroid x_P that is defined by following expression:

$$\int_{V_P} (\mathbf{x} - \mathbf{x}_P) \mathrm{d}V = 0, \tag{48}$$

where V_P represents volume of the cell P. In Figure 5 point N is cell centroid of the neighbouring finite volume, $\mathbf{d_f}$ is the delta vector that connects centroids of two neighbouring cells, $\mathbf{r_P}$ is a position vector of centroid and $\mathbf{s_f}$ is a face area vector, whose magnitude equals the area of corresponding face, S_f, and its direction is defined by a normal of corresponding face. Centroid of a face area vector is located in the centre of the face, which is defined in the same manner as cell centre:

$$\int_{S_f} (\mathbf{x} - \mathbf{x}_f) \mathrm{d}S = 0. \tag{49}$$

Main solution of each variable is stored in the centre of a finite volume. Depending on the purpose different data can be required, for example values in the centre of finite volume faces. This is important because convection and diffusion term in scalar transport equation are discretised using Gauss' theorem that enables calculating volume integral by summing values over the finite volume boundary faces. Values of variables in centres of finite volumes are obtained using face interpolation schemes. Simplest face interpolation schemes are central differencing and upwind schemes. The central differencing is second-order accurate, but causes oscillation of results. It can be mathematically expressed as follows:

$$\Phi_f = f_x \Phi_P + (1 - f_x) \Phi_N, \tag{50}$$

where f_x is an interpolation weight factor which accounts for the relation between points. Value in the face centre is a combination of P and N cells, and corresponding face centre. The upwind differencing takes into account transportive property of the discretised term. This means that information comes from upstream and only the upstream phenomena influences results in downstream. Such face interpolation scheme results in stable results without oscillations, but it is first-order accurate.

$$\Phi_f = max(F,0)\Phi_P + min(F,0)\Phi_N. \tag{51}$$

From Eq. (51) can be concluded that value is defined with only value from one cell. Which cell is taken into account is defined by direction of flux through cell face. Value in the face centre is equal to the value in the centre of upstream cell.

3.1 Discretisation of a Scalar Transport Equation

General form of a scalar transport equation is shown by Eq. (2). This equation is a differential equation that has to be discretised in order to obtain a set of algebraic equations to be calculated. Discretisation of characteristic terms of Eq. (2) are shown in the following subsections.

3.1.1 Discretisation of the Temporal Derivative Term

Temporal derivative term in scalar transport equation is $\dfrac{\partial \Phi}{\partial t}$. This term describes the rate of change of field Φ. For discretisation of temporal derivative term, value of field in cell centre is required in current and previous time instances. First order discretisation of temporal derivative term is called Euler discretisation which takes into account only one previous time instance:

$$\frac{\partial \Phi^n}{\partial t} = \frac{\Phi^n - \Phi^o}{\Delta t}, \tag{52}$$

where ϕ^n is field of variable Φ in time step in which result is calculated ($\phi^n = \Phi(t = t_{new})$) and ϕ^o is field of variable Φ in previous time step ($\phi^o = \Phi(t = t_{old})$). Connection between new and old time instance is time step Δt:

$$t_{new} = t_{old} + \Delta t. \tag{53}$$

Second order approximation of temporal derivative term is called Backward differencing which can be expressed as follows:

$$\frac{\partial \Phi^n}{\partial t} = \frac{\frac{3}{2}\Phi^n - 2\Phi^o + \frac{1}{2}\Phi^{oo}}{\Delta t}, \tag{54}$$

where $\Phi^{oo} = \Phi(t_{new} - 2\Delta t)$.

3.1.2 Discretisation of the Convection Term

Convection term in scalar transport equation is $\nabla \cdot (\mathbf{u}\Phi)$. All terms that have a divergence or gradient operator are transformed from volume integral form into surface integral form using Gauss' theorem. For a general scalar Φ Gauss' theorem can be written as:

$$\int_{V_P} \nabla \cdot \Phi \, dV = \oint_{S_f} dS \cdot \Phi, \tag{55}$$

for divergence form, and

$$\int_{V_P} \nabla \Phi \, dV = \oint_{S_f} dS \, \Phi, \tag{56}$$

for gradient form. According to Eq. (55) and Eq. (56), volume integral of convective term can be transformed into surface integral:

$$\int_{V_P} \nabla \cdot (\mathbf{u}\Phi)\, \mathrm{d}V = \oint_{S_f} \mathrm{d}S \cdot (\mathbf{u}\Phi_f). \tag{57}$$

Surface integral of convection term can be discretised as:

$$\oint_{S_f} \mathrm{d}S \cdot (\mathbf{u}\Phi) = \sum_f \Phi_f (\mathbf{s}_f \cdot \mathbf{u}_f), \tag{58}$$

where scalar product of surface area vector and convective velocity equals the flux, F:

$$F = \mathbf{s}_f \cdot \mathbf{u}_f. \tag{59}$$

Eq. (58) shows that the volume integral of the convection term can be calculated by summing products of the face-centered value, Φ_f, and flux through the same face $\mathbf{F}$, for all faces.

3.1.3 Discretisation of the Diffusion Term

Diffusion term in scalar transport equation is $\nabla \cdot (\gamma \nabla \Phi)$. The volume integral is transformed into the surface integral in the same way as for the convection term:

$$\int_{V_P} \nabla \cdot (\gamma \nabla \Phi)\, \mathrm{d}V = \sum_f \gamma_f\, \mathbf{s}_f (\nabla \Phi)_f. \tag{60}$$

For complete discretisation of the diffusion term it is required to discretise the gradient term $(\nabla \Phi)_f$. Surface normal gradient term can be approximated in the following way:

$$s_f \cdot (\nabla \Phi)_f = \left| \mathbf{s}_f \right| \frac{\Phi_N - \Phi_P}{\left| \mathbf{d}_f \right|} \tag{61}$$

If the gradient term in Eq. (60) is replaced with the formulation shown in Eq. (61), the diffusion term is completely discretised using cell-centered values:

$$\sum_f \gamma_f\, \mathbf{s}_f (\nabla \Phi)_f = \sum_f \gamma_f\, \mathbf{s}_f \frac{\Phi_N - \Phi_P}{\left| \mathbf{d}_f \right|}. \tag{62}$$

3.1.4 Discretisation of Source and Sink Terms

Sink and source terms model local effects, and thus their discretisation yields:

$$\int_{V_P} q_v\, \mathrm{d}V = q_v\, V_P, \tag{63}$$

where q_v can be a function of time and space.

3.1.5   Linear System of Equations

Discretisation of a general scalar transport equation leads to a system of linear equations. Linear equation for a given cell P that assembles all the discretised terms of a scalar transport equation can be written in a general form as:

$$a_P x_P + \sum_N a_N x_N = b, \tag{64}$$

where N denotes the neighbouring cells of a current cell P. Every time x_P depends on itself, contribution is added into coefficient a_P. When x_N depends on itself, contribution is added into coefficient a_N. All other contributions are added into b. If Eq. (64) is written for each cell in the computational domain, linear system of equations is obtained which can be written in a matrix form as follows:

$$\mathbf{Ax} = \mathbf{b}, \tag{65}$$

where $\mathbf{A}$ is a matrix that contains matrix coefficients, a_P and a_N, $\mathbf{x}$ is the value of x_P in the cells and $\mathbf{b}$ is the right hand side. Matrix $\mathbf{A}$ has a dimension of $(N \ x \ N)$, where N is the number of cells required to discretise spatial domain. Even though matrix $\mathbf{A}$ is large, it is a sparse matrix which means that most of its terms are zero. Number of non-zero terms in matrix $\mathbf{A}$ equals the number of cell faces.

3.2   Coupling of Pressure and Velocity

Navier-Stokes set of equations consists of one vector and one scalar equations, while unknowns are pressure and velocity. Same number of equations and unknowns is the necessity for a system to be solvable. Between pressure and velocity exists linear coupling because in pressure equation velocity appears in form of velocity divergence, while in momentum equation pressure is present in form of pressure gradient. In this thesis three pressure-velocity coupling methods are present:

- SIMPLE algorithm,

- PISO algorithm,

- PIMPLE algorithm, which is combination of SIMPLE and PISO algorithm and

- block coupled solver.

3.2.1 Pressure Equation

The Navier-Stokes set of equations for incompressible flow consists of conservation of linear momentum and the continuity equation, where the continuity equation is a scalar equation and conservation of linear momentum is a vector equation. Equation for direct calculation of pressure doesn't exist in this set of equations and a derivation of pressure equation is required. Discretisation of momentum equation in finite volume method leads to expression:

$$a_P^{\mathbf{u}}\mathbf{u}_P + \sum_N a_N^{\mathbf{u}}\mathbf{u}_N = \mathbf{r} - \nabla p, \tag{66}$$

where the pressure gradient is left in the differential form for the purposes of equation derivation. It is common to introduce the $\mathbf{H}(\mathbf{u})$ operator, containing the off-diagonal part of momentum matrix and any right hand side contributions:

$$H(\mathbf{u}) = \mathbf{r} - \sum_N a_N^{\mathbf{u}}\mathbf{u}_N. \tag{67}$$

Using the above, it follows:

$$a_P^{\mathbf{u}}\mathbf{u}_P = \mathbf{H}(\mathbf{u}) - \nabla p \tag{68}$$

and

$$\mathbf{u}_P = (a_P^{\mathbf{u}})^{-1}(\mathbf{H}(\mathbf{u}) - \nabla p). \tag{69}$$

If the expression for $\mathbf{u}_P$ is substituted into the incompressible continuity equation following expression is obtained:

$$\nabla \cdot \left[(a_P^{\mathbf{u}})^{-1}\nabla p\right] = \nabla \cdot \left[(a_P^{\mathbf{u}})^{-1}\mathbf{H}(\mathbf{u})\right]. \tag{70}$$

Eq. (70) is the form of the pressure equation for incompressible fluid flow.

3.2.2 SIMPLE Algorithm

SIMPLE algorithm is the earliest velocity coupling method discovered by Patankar and Spalding in 1972. Sequence of operations present in this algorithm is as follows:

1. Guess the pressure field p^*.

2. Solve the momentum equation with guessed pressure from the previous step. This step is called momentum predictor.

$$a_P^{\mathbf{u}}\mathbf{u}_P = \mathbf{H}(\mathbf{u}) - \nabla p^* \tag{71}$$

3. Calculate the new pressure based on the velocity field from previous step. This step is called pressure correction.

$$\nabla \cdot [(a_P^{\mathbf{u}})^{-1}\nabla p] = \nabla \cdot [(a_P^{\mathbf{u}})^{-1}\mathbf{H}(\mathbf{u})] \tag{72}$$

4. Based on the pressure solution, conservative face flux is assembled.

$$F = \mathbf{s}_f \cdot \mathbf{H}(\mathbf{u}) - a_N^p(p_N - p_P) \tag{73}$$

5. This sequence is repeated untill desired convergence is achieved.

SIMPLE iteration sequence in the above form will diverge. Divergence is due to the fact that pressure correction contains both the pressure as a physical variable and a component which forces the discrete fluxes to become conservative. In order to achieve convergence, under-relaxation factors are used:

$$p^{**} = p^* + \alpha_p(p - p^*) \tag{74}$$

and

$$\mathbf{u}^{**} = \mathbf{u}^* + \alpha_u(\mathbf{u} - \mathbf{u}^*), \tag{75}$$

where α_p and α_u are under-relaxation factors for pressure and velocity. Pressure is under-relaxed explicitly and $\mathbf{u}$ implicitly. In Eq. (74) and Eq. (75) p and $\mathbf{u}$ are the solution of the pressure and momentum equations, $\mathbf{u}^*$ and p^* are pressure and velocity approximations from the previous iteration. Final solution consist from both solutions of the pressure and the momentum equations and approximations of pressure and velocity from previous iteration. How much of the current solution and solution from previous time step is taken into new solution is defined with under-relaxation factors.

3.2.3 PISO Algorithm

PISO algorithm is useful in simulations where the time-step is controlled by external issues and temporal accuracy is important. Sequence of operation is as follows:

1. Use the available pressure field p^* from previous corrector or time step with the conservative fluxes corresponding to p^*.

2. Discretise the momentum equation with the available flux field.

3. Solve the momentum equation using the available pressure field. This step is called the momentum predictor.

$$a_P^{\mathbf{u}}\mathbf{u}_P = \mathbf{H}(\mathbf{u}) - \nabla p^* \tag{76}$$

4. Calculate the new pressure field based on the velocity from momentum predictor step. This step is called the pressure correction step.

$$\nabla \cdot [(a_P^{\mathbf{u}})^{-1}\nabla p] = \nabla \cdot [(a_P^{\mathbf{u}})^{-1}\mathbf{H}(\mathbf{u})] \tag{77}$$

5. Based on the new pressure field, assemble the conservative face flux.

$$F = \mathbf{s}_f \cdot \mathbf{H}(\mathbf{u}) - a_N^p(p_N - p_P) \tag{78}$$

6. Explicitly update velocity field with the assembled momentum coefficients.

$$\mathbf{u}_P = (a_P^{\mathbf{u}})^{-1}(\mathbf{H}(\mathbf{u}) - \nabla p) \tag{79}$$

7. Return to pressure correction step if convergence is not reached.

3.2.4 Block Coupled Solver

Navier-Stokes set of equations is usually solved using the segregated solvers. Characteristics of segregated solvers are:

- Low memory peak due to calculation of a single equation at the time,

- under-relaxation (SIMPLE) is resulting in slower convergence,

- convergence is effected by a mesh size.

On the other side, in coupled solvers matrix size is increased, but the coupling of pressure and velocity is fully implicit. On top of that, iterations are only required to solve non-linear convective term in the momentum equation and the turbulence. Therefore, convergence is significantly improved at a cost of increase in memory usage.

Each coefficient of a block-coupled system matrix is a tensor with 4 terms as shown by Eq. (80), where $a_{P_{(U\ p)}}$ is a matrix coefficient of a cell P taking into account how the velocity of the cell P influences the pressure of the cell P. Meaning of all the other coefficients can be derived analogically. The second matrix of Eq. (80) represents the unknown variables, and third matrix represents the source terms.

$$
\begin{bmatrix}
\begin{pmatrix} a_{P_{(U\ U)}} & a_{P_{(U\ p)}} \\ a_{P_{(p\ U)}} & a_{P_{(p\ p)}} \end{pmatrix} & \begin{pmatrix} a_{N_{(U\ U)}} & a_{N_{(U\ p)}} \\ a_{N_{(p\ U)}} & a_{N_{(p\ p)}} \end{pmatrix} & \cdots \\
\cdot & \begin{pmatrix} a_{P_{(U\ U)}} & a_{P_{(U\ p)}} \\ a_{P_{(p\ U)}} & a_{P_{(p\ p)}} \end{pmatrix} & \cdots \\
\vdots & \vdots & \ddots
\end{bmatrix}
\begin{bmatrix} U_1 \\ p_1 \\ U_2 \\ p_2 \\ \vdots \end{bmatrix}
=
\begin{bmatrix} b_{U\ 1} \\ b_{p\ 1} \\ b_{U\ 2} \\ b_{p\ 2} \\ \vdots \end{bmatrix}
\tag{80}
$$

3.3 Closure

In this section, the finite volume discretisation technique has been described. It allows a transformation of the partial differential equations into a sets of algebraic linear equations of equal physical properties. Before the calculation, spatial domain in form of numerical mesh has to be defined along with the time step which defines the temporal domain. Discretisation of the desired set of equations results in a system of equations that can be solved using the linear solvers. For calculation of Navier-Stokes equations the algorithm for coupling of the pressure and velocity has to be specified. Segregated solver are nowadays usually used, but with the development of computer technology, memory usage is becoming less of a problem and the methods like the block-coupled pressure and velocity can be used.

4   Geometry and Numerical Spatial Domain

Geometries of centrifugal pumps on which meshes are generated were provided in general, STL format. Provided geometries were already cleaned and simplified. Clean geometry is geometry that consists only of parts that significantly effect fluid flow and are ready for the meshing process.

4.1   Introduction

This section presents geometries of both pumps studied in this thesis. It also covers the process of numerical mesh generation. Both numerical meshes were made manually in the software, called Pointwise [5]. The process of manual generation of mesh is time intensive, but user has greater control over the meshing process compared to the automatic mesh generation. On the other hand, the lack of working experience in this software can lead to the generation of unusable mesh.

The structure of this section is divided into two main subsection. The first subsection deals with the geometry and the mesh generation of the OTA-1 pump, while the second subsection covers the geometry and the mesh generation of the OTA-2 pump.

4.2   OTA-1 Pump

The OTA-1 pump is a double-suction in-line horizontal centrifugal pump. Rotational speed for nominal operating point of the pump equals 1300 rpm. Geometry of the pump is shown in Figure 6. Characteristic zones of the OTA-1 pump are:

- the inlet pipe zone with the inlet stator casing (coloured yellow in following figures),

- the rotor zone (coloured red in following figures)

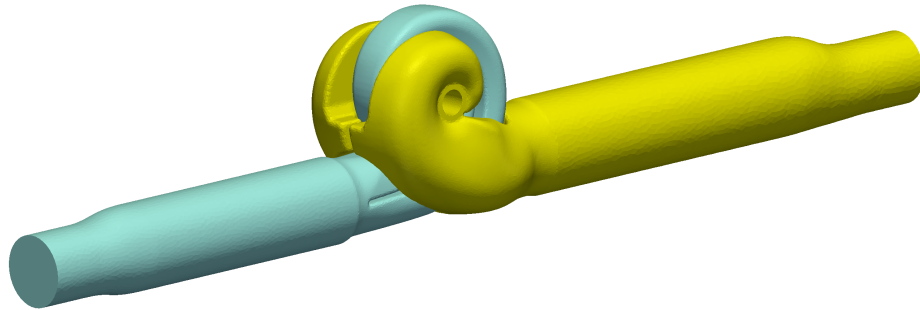- and the outlet casing zone with the outlet pipe (coloured blue in following figures).

Figure 6: Geometry of the OTA-1 pump.

The rotor of the OTA-1 pump is diagonal. This means that the fluid enters the rotor in an axial direction and leaves the rotor in a direction that is not completely radial but the absolute velocity on the outlet has an axial component. Figure 6 also defines position of the rotor. The inlet of rotor is positioned where the inlet casing, coloured yellow, ends and the rotor outlet is positioned where the outlet spiral casing, coloured blue, begins.
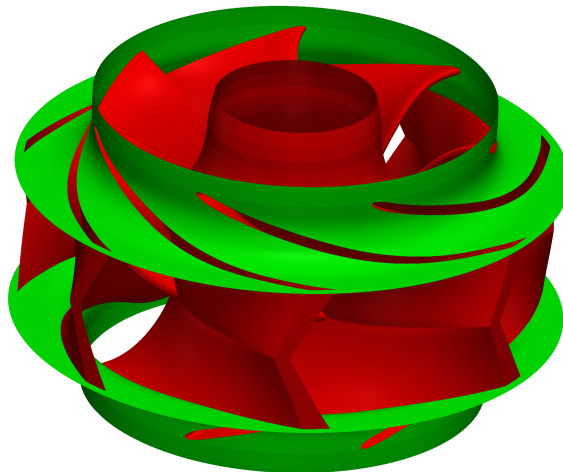

Figure 7: Geometry of the OTA-1 rotor.

Rotor of the OTA-1 pump has 7 blades that are cut to desired diameter. In case of the OTA-1 pump, desired outer diameter of rotor blades equals 0.3 m. In Figure 7 rotor blades are coloured red and the sharp trailing edges indicate that blades are cut. Manufacturer of the pumps is not producing pumps individually for an application. A pump with the specified diameter of rotor

is produced and for every other application rotor blades are cut. The cutting of rotor blades is a commonly used method for regulation of pump head and power because power of a pump increases with the 5th power of the rotor diameter.
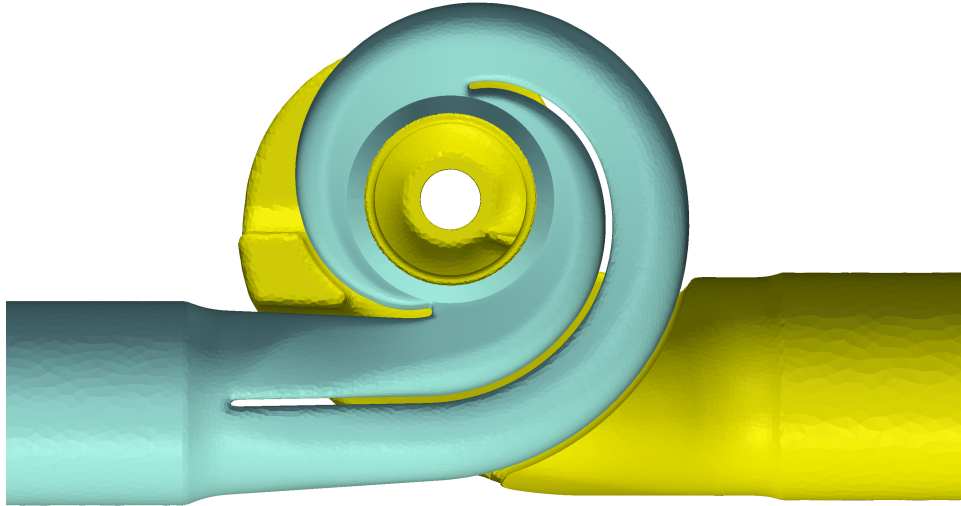

Figure 8: Spiral outlet casing of the OTA-1 rotor.

Figure 8 shows the spiral inlet and outlet casing. Shape of the casing indicated that this pump is modern and it has high efficiency. The outlet spiral casing is used as a diffuser and its function is to transform kinetic energy of fluid that leaves the rotor into pressure energy. It can also be seen that the pump casing is double-outflow. Each outflow channel acts like a stator blade of the pump. Stator blades influences frequencies of all transient phenomena that occur in the pump flow. For example, frequency of pump head in time is defined by a number of rotor blades, number of stator blades and the rotational speed of the rotor. The main harmonic of periodic pump head is defined by rotor blades and the rotational speed and its frequency equals the product of the rotational speed and the number of blades. The second harmonic is defined by the rotor blades and the rotational speed and it is superposed on the main harmonic.
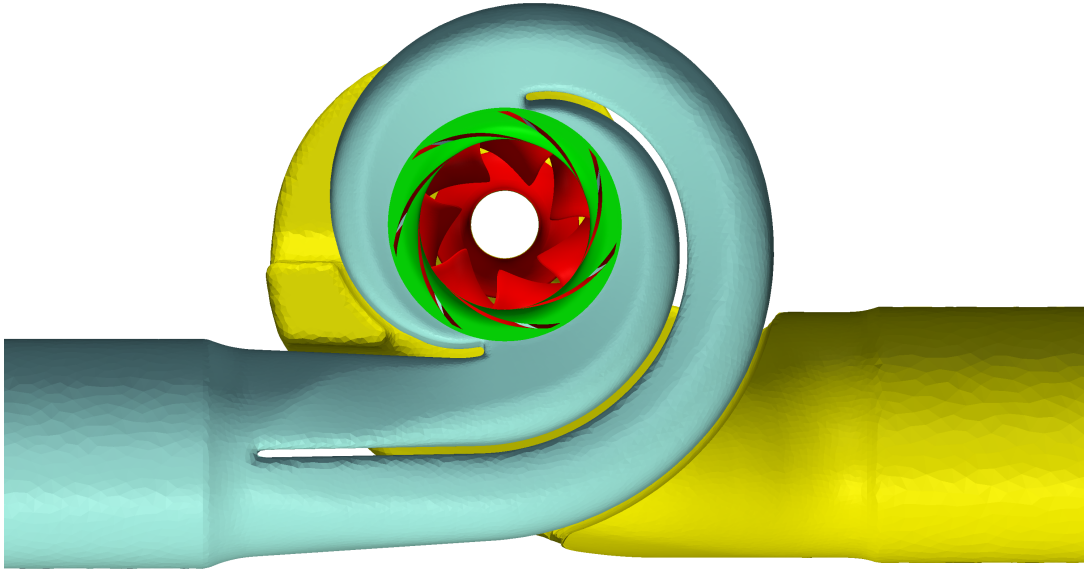
Figure 9: Cross-section of pump.

Figure 9 shows a cross-section of a pump with all the mentioned parts.

Remaining geometric parts that influences the behaviour of the pump are the inlet and the outlet pipes. The cross-section area of inlet and outlet pipes define the inlet and the outlet average velocities. For the OTA-1 pump cross-section for the outlet and the inlet pipe, are circular and have the same diameter that equals 0.254 m. Due to the same diameters of the inlet and the outlet pipe, average velocities on the inlet and the outlet have to be the same according to continuity equation for incompressible flow. Because of that, pump head is defined only by the difference of the average pressure on the inlet and the outlet:

$$H = \frac{\Delta p}{\rho g}, \tag{81}$$

where Δp is the pressure difference, ρ is the fluid density and g is gravitational acceleration.

The parameter that classifies pumps according to the rotor type is called specific speed. Specific speed is defined with following expression:

$$n_s = \frac{n\sqrt{Q}}{H^{\frac{3}{4}}}, \tag{82}$$

where n is the rotational speed of rotor, Q is the volumetric flux and H is the pump head. For the nominal operating point rotational speed equals 1300 rpm, volumetric flux equals 14.5 m^3/min and head equals 14.5 m. According to these parameters for the optimal operating point, specific speed of the OTA-1 pump is equal to 86 min^{-1}. Specific speed of 86 min^{-1} classifies rotor of the OTA-1 pump as a diagonal rotor. Specific speed of the pump is interesting parameter because it defines the type of pump rotor and the application of pump. Pumps with

higher specific speed are used where higher volumetric flux of pump is desired, but lower head. If the pump has lower specific speed it will be used where higher head is needed with lower volumetric flux. According to Eq. (83), specific speed is proportional to the rotational speed of pump.

4.2.1 Numerical Spatial Domain

Numerical spatial domain is a set of finite volumes in which discretised equations, that are included in the mathematical model, are solved.

The mesh of the OTA-1 pump is generated on the geometry that is presented in the previous section. All simulations are performed on a single mesh, including simulation with a fixed position of rotor and a dynamic mesh. The OTA-1 mesh consists of 3 cell zones, each made for one characteristic part of the pump geometry. Cell zone with most cells and the greatest effect on numerical results is the rotor cell zone coloured red in following figures.
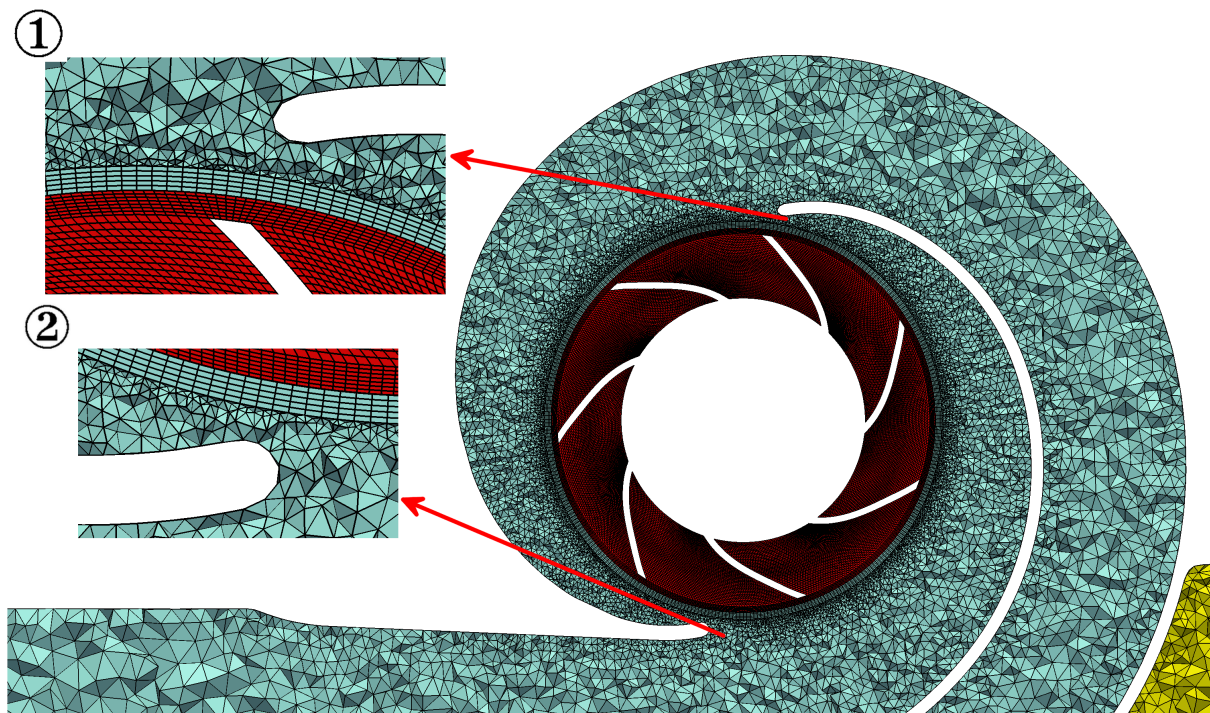
Figure 10: Numerical mesh on a cross-section of the OTA-1 pump.

Figure 10 shows the numerical spatial domain of the OTA-1 pump. It can be seen that the domain of the rotor is made in a structured mesh, while the domains of the inlet and the outlet pipe are made in an unstructured mesh, with an exception of the narrow zone around rotor-stator interfaces. Special attention is given to the meshing process of domains in the proximity of the rotor-stator interface. It is desired that all cells are equal in size and structured from both sides of the interface. In such way, problems connected to the transition from a structured to an unstructured mesh on the interface in a dynamic mesh simulations are avoided. In Figure

10, the interface is positioned between the rotor and the stator zone, what can be seen closely in details 1 and 2. Detail 1 gives a closer look at the zone which includes the mesh around the upper breakwater, the narrow zone around the rotor-stator interface and the tip of the rotor blade. Requirement in the meshing process is for interface patches to be axisymmetrical. If this is not the case, in the run-time of simulation, holes and overlapping of cells in the proximity of the interface appear. To avoid this problem, patches of the interface on the rotor outlet are projected onto a cylinder shell. The rotor zone with the interface patches on the side of the rotor domain, are shown in Figure 11.
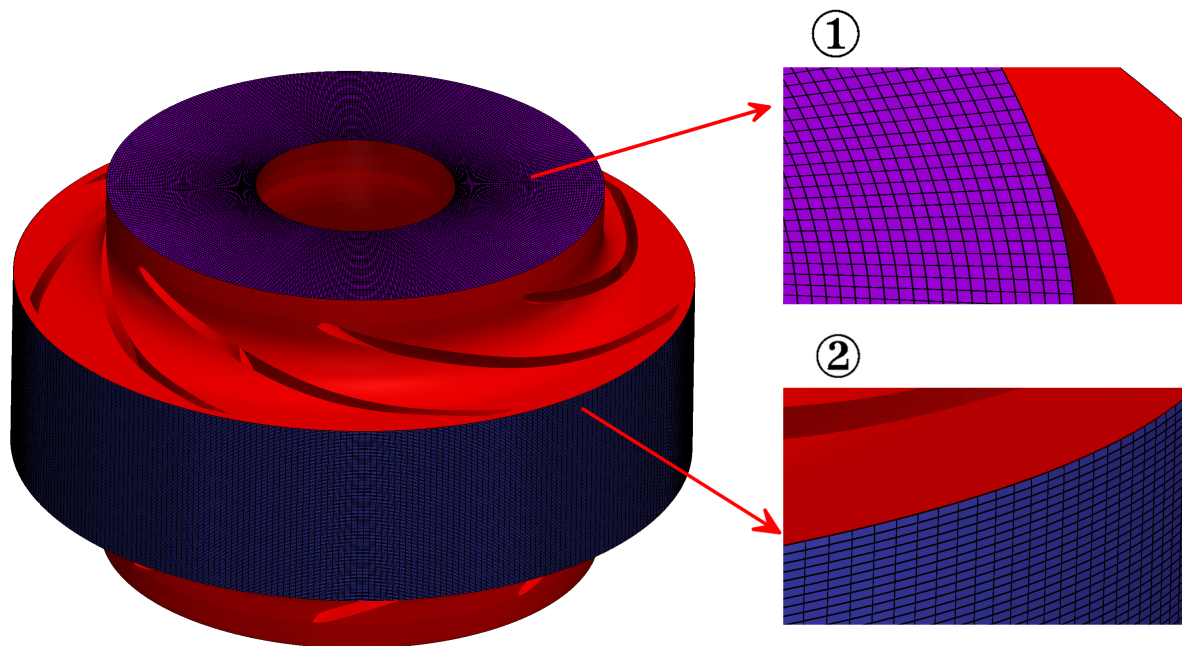
Figure 11: The rotor-stator interfaces of the OTA-1 pump.

From previous figures can be noticed that the mesh of the OTA-1 is combination of a structured and an unstructured mesh. This is called a hybrid mesh. In geometries similar to the geometry of the OTA-1 pump hybrid meshes are ideal for running a first simulation. Hybrid mesh is a compromise between the result accuracy, the number of cells and the time required for the mesh generation. Structured meshes provide best accuracy of numerical results and consist of less cells than equivalent unstructured mesh. It is desired to mesh parts that are of highest importance for numerical simulation in a structured mesh. On the other hand, complex geometry parts that have lower effect on results are meshed in an unstructured mesh what reduces the time required to mesh complicated parts of the geometry.

Table 1: The number of cells for characteristic cell zones of the OTA-1 pump.

Cell zone	Number of cells
Inlet pipe	1 033 347
Rotor	5 144 048
Outlet pipe	2 877 122
Total	9 054 517

Table 1 shows the number of cells for characteristic cell zones. Total number of cells of the OTA-1 mesh equals 9 054 517:

- 5 349 008 hexahedral cells,

- 44 352 pyramidal cells

- and 3 661 157 tetrahedral cells.

4.3 OTA-2 Pump

The OTA-2 pump is a vertical centrifugal pump with stator guiding blades in the section before rotor. The rotational speed of the pump for the nominal operating point equals 800 rpm. The geometry is shown in Figure 12.
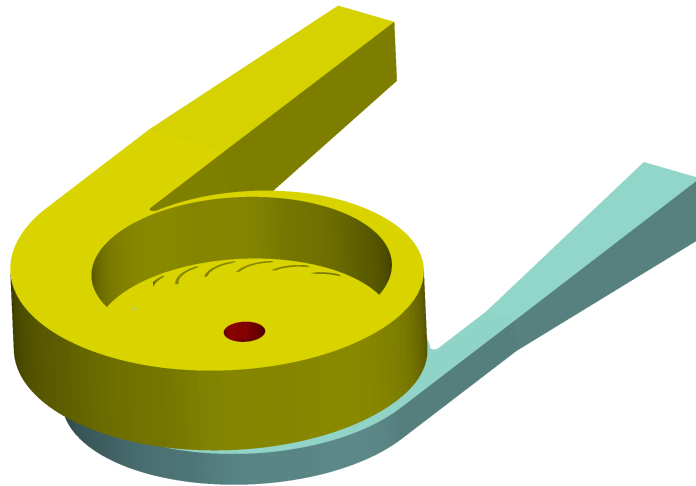
Figure 12: Geometry of the OTA-2 pump.

The rotor of the OTA-2 pump is radial what means that the direction of a fluid flow at the rotor inlet is axial and at the rotor outlet, the direction of the flow is completely radial. Figure 13 shows the rotor of the pump with 3 blades.
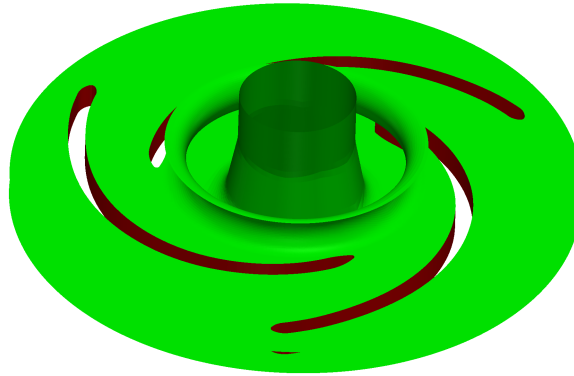
Figure 13: Geometry of the OTA-2 rotor.
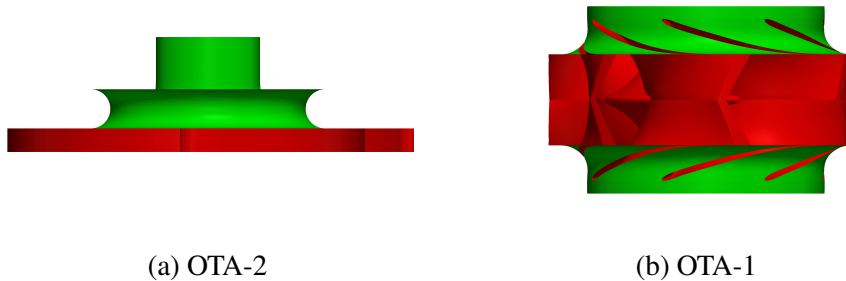
(a) OTA-2   (b) OTA-1

Figure 14: Rotor side views of both pumps.

Figure 14 shows rotor side views of both pumps. It can be seen that rotor of the OTA-2 pump has a lower height of the blades and a larger diameter than the rotor of the OTA-1 pump. The height of OTA-2 rotor blades equals 0.018 m, while the height of the OTA-1 rotor blades equals 0.086 m. The diameter of the OTA-2 rotor equals 0.348 m. This is also indicated by the specific speed of both pumps. For the nominal operating point the rotational speed of the OTA-2 equals 800 rpm, the volumetric flux equals 0.95 m^3/min and the head equals 7.8 m. According to these parameters and Eq. (81), the specific speed of the OTA-2 pump equals 21.6 min^{-1}. Such value of specific speed categorise the OTA-2 pump into radial pumps and indicates that the volumetric flux of the OTA-2 pump is lower and that the head is higher than for the OTA-1 pump, per unit of power.
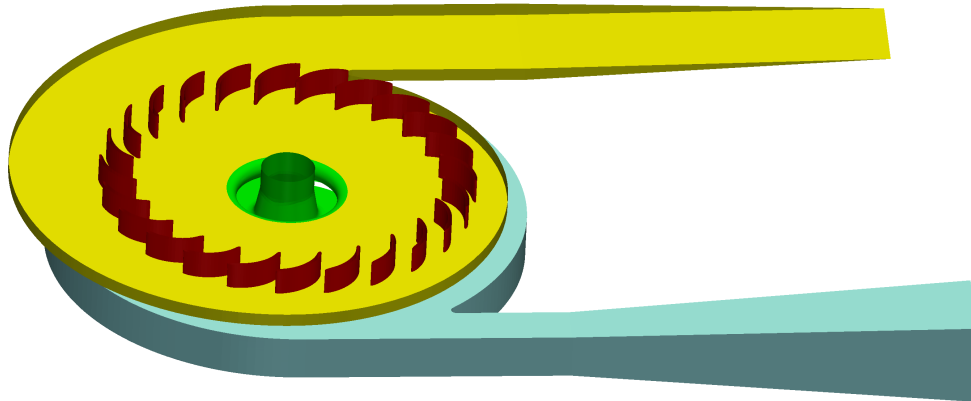
Figure 15: Stator blades of the OTA-2 pump.

In the section before the rotor of the OTA-2 pump, stator guiding blades are set, what is shown in Figure 15. The main purpose of stator blades is guiding of the flow in such a way that the flow enters rotor smoothly. Stator blades are designed for the nominal operating point and the efficiency of pump decreases when the operating point is changed. In the OTA-1 pump, the role of guiding blades has the inlet pipe casing.
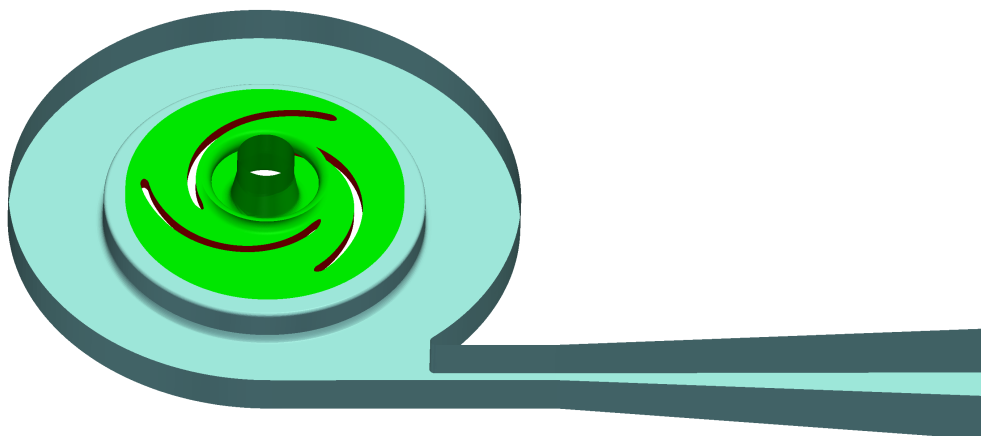

Figure 16: Position of the rotor in the outlet casing of the OTA-2 pump.

Figure 17: The shape of the OTA-2 outlet casing.

Figure 16 and Figure 17 show position of the rotor in the pump outlet casing. From Figure 17 can be seen that the spiral casing of the OTA-2 pump has a single outflow channel. This is equivalent of a pump with a single stator blade on the outlet of the pump. Influences on the frequency of transient phenomena are equivalent to the one presented in previous section with the difference in number of stator blades taken into account.

The inlet and the outlet pipes have rectangular cross-sections with the side dimension of 0.13 m and the cross-section area of 0.0169 m^2. Due to the equal cross-section areas of the inlet and the outlet pipe, the head is only a function of the pressure difference because the continuity equation has to be satisfied.

4.3.1 Numerical Spatial Domain

Numerical spatial domain of the OTA-2 pump is generated on the geometry presented in the previous section. The mesh consists of 3 cell zones, each created for a characteristic part of a pump geometry. Separately created zones are merged together into a single domain. Characteristic zones of the OTA-2 pump are as follows:

- the inlet pipe zone with the inlet stator casing,

- the rotor zone and

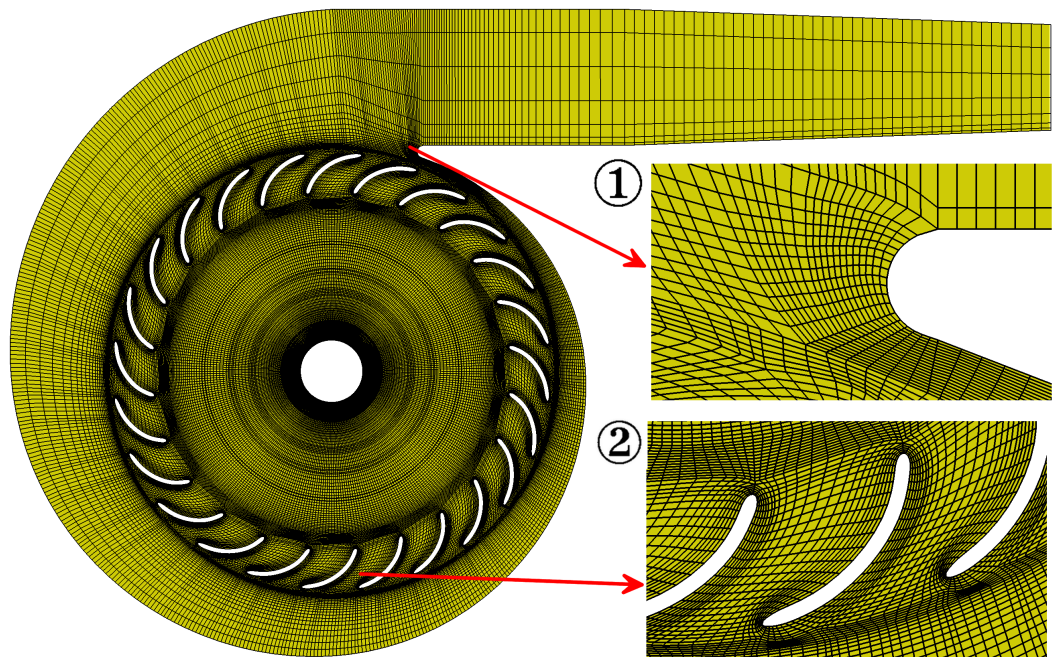- the outlet casing zone with the outlet pipe.

Figure 18: Numerical mesh on the inlet stator cross-section of the OTA-2 pump.

Figure 18 shows the cross section of the inlet pipe and the inlet stator casing cell zone. This cell zone has medium mesh resolution due to the importance of stator blade passages on results of numerical simulations. Details of mesh are also shown and denoted with numbers 1 and 2. Detail 1 shows the mesh on the connection between the inlet pipe and the stator casing. Higher resolution of mesh around the breakwater is a result of a structured mesh and the realization of the mesh in this area. Detail 2 shows the mesh around the stator blades. Detail shows that the resolution in the proximity of stator blade geometry is higher due to the effect a boundary layer has on results. The height of the first cell row is defined by desired y^+, which is in the presented numerical domain greater than 30 for all cells that define the stator blade geometry. The mesh in the cross section parallel to the side view of the pump is shown in Figure 19. In figure are also shown details of non-conformal parts of the mesh around rotor-stator interfaces. Detail 1 shows a part of the rotor-stator interface at the rotor inlet. This interface is different from other presented in the thesis because patches of this interface are projected onto cone shell for them to become axisymmetrical. Detail 2 shows a part of the rotor-stator interface at the rotor outlet. Figure 19 gives a better idea of how the flow enters and exits the rotor of the pump, while providing an information about the mesh in the proximity of rotor-stator interfaces.
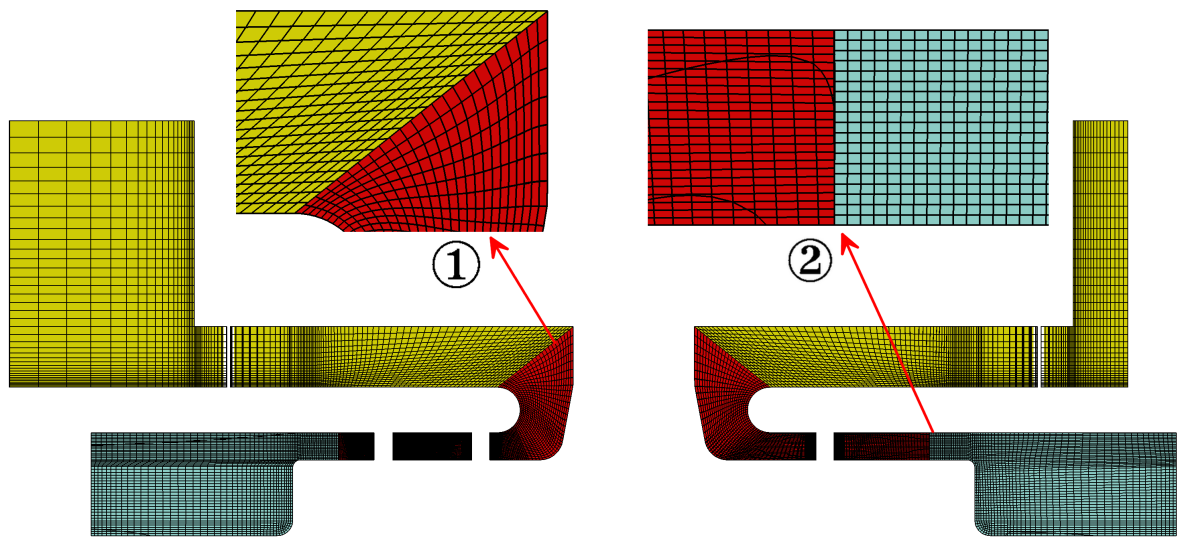
Figure 19: Numerical mesh in a cross section parallel to the side view of the OTA-2 pump.
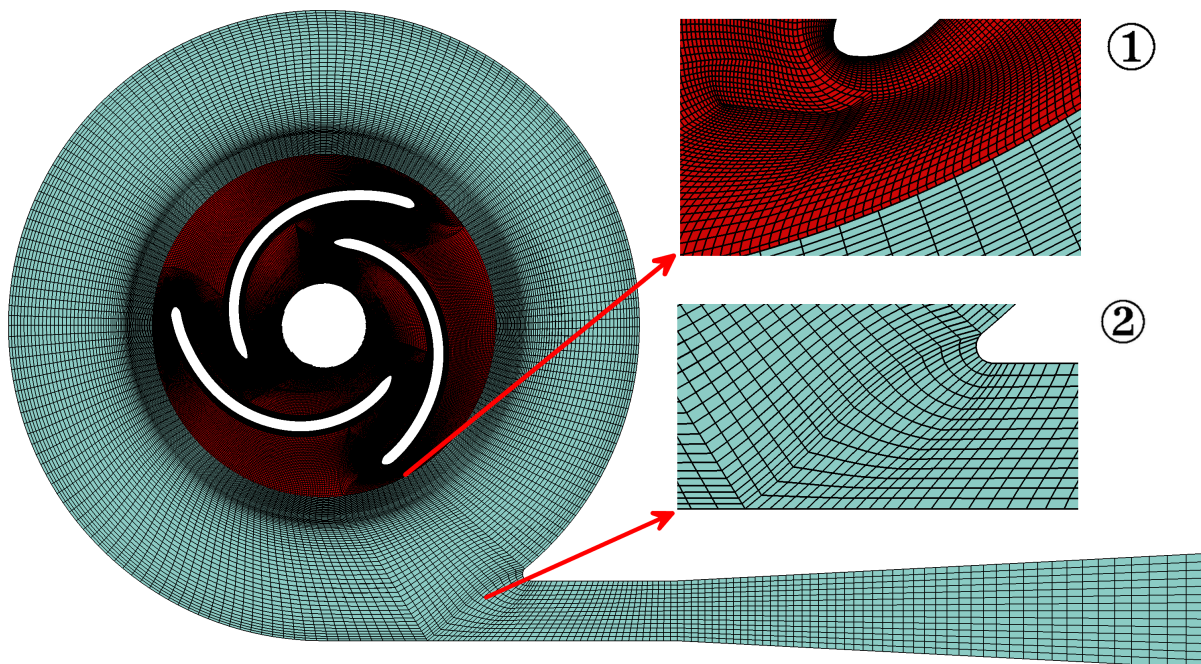

Figure 20: Numerical mesh on a rotor cross-section of the OTA-2 pump.

Figure 20 shows a part of the mesh used to discretise geometry part of the rotor casing and the stator casing with the outlet pipe. Whole figure is presenting resolution of the mesh, while also providing details of mesh parts in characteristic areas. Detail 1 shows a part of the mesh at the tip of the rotor blade and a part of the mesh around the rotor-stator interface which connects

mutually non-conformal meshes of the rotor and the stator zones. The rotor zone is a part of the mesh with the finest resolution due to its importance on simulation results. The zone in which boundary layer of the flow occurs is meshed in greater resolution, but taking into account to keep the height of the first cell row on values which result in y^+ greater than 30. Detail 2 gives an information about the realization of the mesh on the connection between the stator casing and the outlet pipe.

From previously presented figures can be noticed that segregated cell zones are mutually non-conformal and connected with the help of rotor-stator interfaces. It is also evident that all parts of the domain are made in a structured mesh and consist of only hexahedral finite volumes. In the meshing process, special attention was given to narrow zones around the rotor-stator interfaces due to requirement of axisymmetrical interfaces. Hence, all interfaces are projected onto cylinder and cone shell. Position of the interface patches is shown in Figure 21, where the conical interface at the rotor inlet is coloured purple, while the cylindrical interface at the rotor outlet is coloured blue. Details of the figure show the way interface meshes are realized.
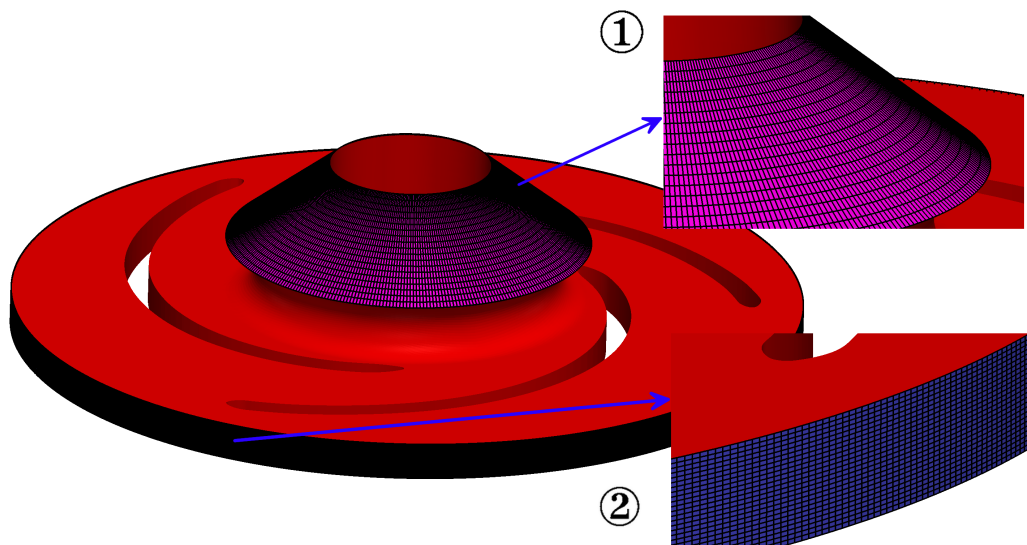

Figure 21: Rotor-stator interfaces of the OTA-2 pump.

Table 2 shows a number of cells for characteristic cell zones of the OTA-2 pump. The total number of cells equals 3 970 344 and all the cells are hexahedral.

Table 2: Number of cells for characteristic cell zones of the OTA-2 pump.

Cell zone	Number of cells
Inlet pipe and stator casing	1 118 796
Rotor	2 290 104
Outlet pipe and stator casing	561 444
Total	3 970 344

4.4   Closure

This section presents the generation process of numerical spatial domains. Meshes are used to discretise the spatial domain in which the equations defined in the mathematical model are solved. For the purposes of the thesis two meshes are manually created for two geometries of centrifugal pumps in the software called *Pointwise*.

5 Results

Simulations are performed on two meshes as described in the section 4.

5.1 Introduction

The section is divided into two main subsections considering two pumps: the OTA-1 and the OTA-2 pump. At the end of each section accuracy and CPU time performance from various numerical models are compared.

5.2 OTA-1 Pump

All simulations regarding the OTA-1 pump are performed for the same mesh. This section comprises results from additional numerical models:

- segregated and coupled solver,

- non-consistent and consistent solver and

- the effect of new general grid interface (GGI).

5.2.1 Transient Simulation

Transient simulation in this thesis is assumed to be the most accurate simulation yielding referent solution. Difference between transient and steady-state simulation is that in transient simulation all the equations of mathematical model are solved in their original form. On top of that, finite volumes of rotor cell zone are rotating with the angular velocity of the pump rotor.

The fixed value of velocity is set on the inlet patch and the fixed value of pressure is set on the outlet patch. Velocity is set in such way that the product of inlet patch surface area and velocity equals the specified volumetric flux. Pressure on the outlet is set to 0 Pa and the pressure field obtained by the numerical simulation is relative to value of pressure field specified at the outlet. Boundary conditions of turbulence parameters are calculated using empirical expressions for turbulence intensity and turbulence length scale. Turbulence length scale is calculated as:

$$l = 0.07D_h, \tag{83}$$

where D_h is hydraulic diameter which is, for a pipe flow, equal to inner pipe diameter. Turbulence intensity (I) is approximated with value of 3%. Inlet boundary condition for

turbulent kinetic energy is calculated using the expression:

$$k = \frac{3}{2}(I\mathbf{v}_{inlet})^2.$$

(84)

Inlet boundary condition for specific dissipation rate is calculated according to expression:

$$\omega = \frac{k^{0.5}}{C_\mu^{0.25}l},$$

(85)

where C_μ is a constant that is defined within the turbulence model.

Boundary conditions for for the OTA-1 pump are summarized in Table 3.

Table 3: Velocity and pressure boundary conditions for transient simulation of the OTA-1 pump.

Patch	Velocity boundary condition	Pressure boundary condition
inlet	fixedValue; uniform (U_x 0 0);	zeroGradient;
outlet	zeroGradient;	fixedValue; uniform 0;
rotorBlades	movingWallVelocity; uniform (0 0 0);	zeroGradient;
rotorCasing	movingWallVelocity; uniform (0 0 0);	zeroGradient;
shaft	movingWallVelocity; uniform (0 0 0);	zeroGradient;
inletCasing	fixedValue; uniform (0 0 0);	zeroGradient;
outletCasing	fixedValue; uniform (0 0 0);	zeroGradient;
rotor-stator interfaces	ggi;	ggi;

Inlet velocity, U_x is varied for each operating point as follows:

- first operating point: 4.778 $\frac{m}{s}$ for the volumetric flux 14.5 $\frac{m^3}{min}$,

- second operating point: 3.822 $\frac{m}{s}$ for the volumetric flux 11.6 $\frac{m^3}{min}$ and

- third operating point: 5.734 $\frac{m}{s}$ for the volumetric flux 17.4 $\frac{m^3}{min}$.

Initial condition of velocity is defined with the magnitude of inlet velocity and direction of the main flow for each cell, while the pressure initial condition is defined with the value of 0 Pa.

Initial conditions of turbulence parameters are defined for the whole spatial domain with the same values calculated for inlet boundary patch.

For dynamic mesh in transient simulation is required to define rotating cell zone that defines the rotor geometry. Assigned velocities depend on rotational speed, which for the OTA-1 pump equals 1300 rpm. Maximum velocity depends on tangential velocity that occurs at the tip of the rotor blade with high mesh resolution. Hence, maximum Courant number that occurs in a simulation is defined by phenomena around a tip of the rotor blade. In all simulations of this thesis, maximum Courant number is below 5. Taking into account maximum value of Courant number of 5, time step for transient simulation of the OTA-1 pump equals 10^{-4} s. In one time step, finite volumes defining rotor cell zone rotate for approximately $2°$. For the purpose of this thesis, pimpleDyMFoam in foam-extend 4.0 is used and is compared to the older version implemented in foam-extend 3.2. Main difference between the two is that the former is consistent.

Rotor-stator interface used in this simulation is GGI which is used to couple non-conformal rotor and stator cell zone when rotor cell zone is rotating.

Results

results of transient simulation consist of two parts:

1. time-averaged field of pressure, velocity and turbulence parameters.

2. Performance curves of head, power and efficiency as a function of time.

To create time-averaged fields new averaging application had to be developed because function object implemented in OpenFOAM does not take into account rotation of cell zones when averaging is performed on a vector field. Each cell has the same ID when a cell zone is rotating and because of that, velocity or any other vector variable will change its direction in respect to global coordinate system. If vectors of velocity defined in such way are taken into process of averaging, wrong values of averaged velocity field is obtained because tangential velocities of a flow in a rotor cell zone cancel out mutually. Application that is made for averaging is based on rotating the rotor cell zone to a referent position which is defined with the position of rotor in a first time-step taken into process of averaging according to Eq. (86). Direction of vectors in a vector field have to be rotated for the same angle as the rotation of a rotor cell zone.

$$\mathbf{u}_{\text{mean}} = \alpha \mathbf{u}_{\text{mean}} + \beta \mathbf{u}, \tag{86}$$

where $\mathbf{u}_{\text{mean}}$ is averaged field of velocity, $\mathbf{u}$ is new value of vector velocity field taken into

process of averaging. Coefficients α and β change for each time step and are defined as:

$$\alpha = \frac{t_{i-1}}{t_i},$$ (87)

and

$$\beta = 1 - \alpha = \frac{\Delta t}{t_i}.$$ (88)

In expressions Eq. (87) and Eq. (88) t_i represents current time-step that is taken into averaging.

Transient simulation of the OTA-1 pump is performed for three operating points which are defined with the inflow volumetric flux. Parameters of the pump that are obtained as a result are pump head and pump power. Function object used to calculate mentioned parameters is called turboPerformance. This tool enables the calculation of pump power, head and efficiency during run-time of a both transient and steady-state simulations. Head is calculated as a difference of total energy on inlet and outlet patch using the following expression:

$$H = \frac{E_o - E_i}{\rho\,g},$$ (89)

where E_o is a fluid energy at the outlet patch and E_i is a fluid energy at the inlet patch. Fluid energy is defined with three characteristic terms in the same way as in the Bernoulli equation:

1. potential energy: $E_p = \rho g h$,

   where h is the height of a patch for which fluid energy is calculated. This term is neglected because mass forces are not taken into account in the calculation.

2. kinetic energy: $E_k = \frac{1}{2}\rho\mathbf{v}^2$.

   Difference of kinetic energy for both pumps observed in this thesis is equal to zero due to the same areas of inlet and outlet pipe cross-sections.

3. pressure energy: $E_p = p$.

Hence, in following simulations head is only the function of a pressure difference at the inlet and outlet patch. Power of the pump is calculated using the following expression:

$$P = M\omega,$$ (90)

where M is a torque with respect to the axis of rotor rotation and ω is angular velocity. Combination of head, power and volumetric flux results in an expression for calculation of efficiency:

$$\eta = \frac{\rho g H\,Q}{P}.$$ (91)

In transient simulation, performance curves comprising head, power and efficiency need to be

quasi-stationary (periodic), thus yielding convergence.

Time-averaged flow fields and turbulence parameters

Legends of all figures representing time-averaged fields are in a standard SI units. All the following figures in this subsection represents time-averaged fields for first operating point that has maximum efficiency.
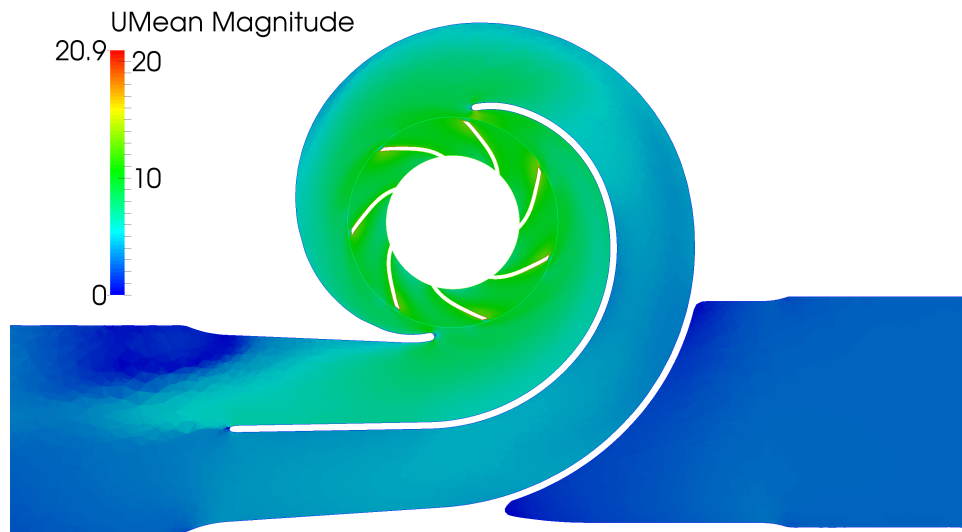
Figure 22: Time-averaged velocity field of the OTA-1 pump.

Figure 22 shows velocity field around the rotor. It can be seen that the highest velocity magnitudes occur in proximity of rotor blades due to tangential velocity of the rotor. Fluid exits the pump through two outlet channels used to convert kinetic energy of a fluid into the pressure energy. The rise in the pressure value in the outlet channels can be seen in Figure 23 which shows the pressure distribution in the rotor cell zone and in the outflow channels.
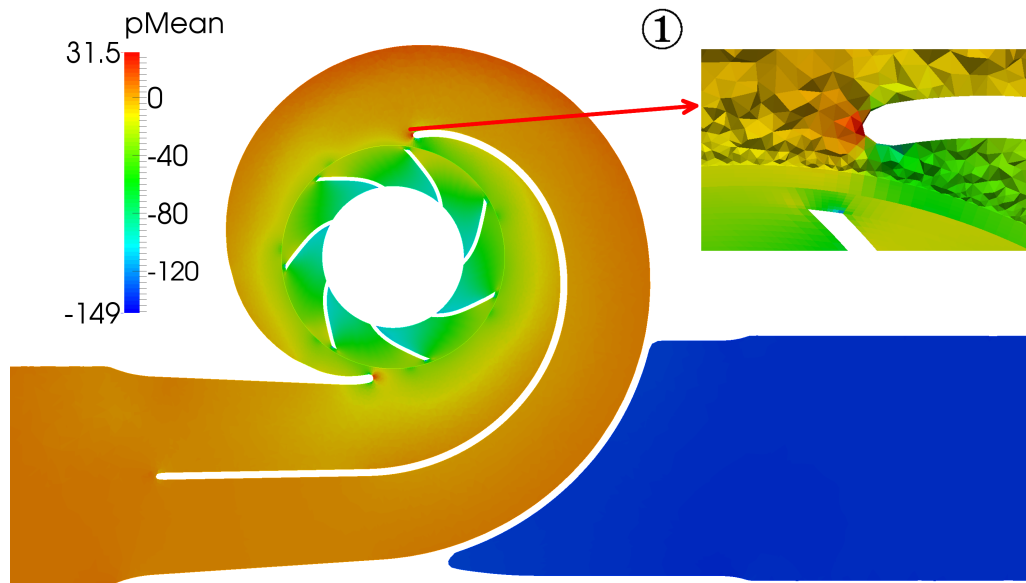
Figure 23: Time-averaged pressure field of the OTA-1 pump.

Higher and lower pressure zones between the rotor blades in Figure 23 indicate the rotation direction of the rotor because the higher pressure side is always in front of the rotor blades what is also evident from the position of the outflow channels. At the entrance of the outflow channels are zones of the highest pressure because in this zones stagnation pressure occurs what can be seen in the detail of the Figure 23.
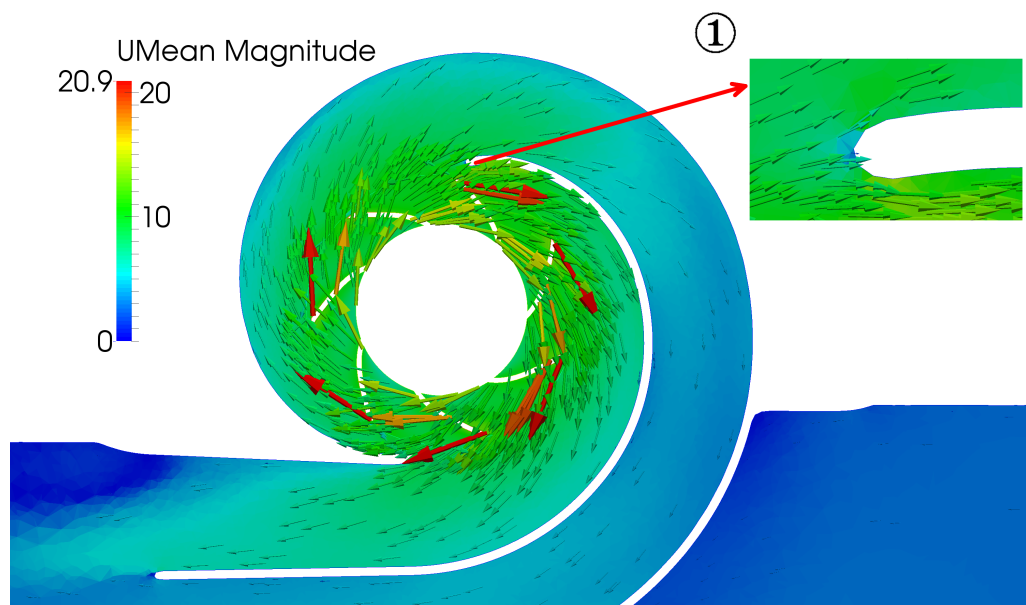
Figure 24: Distribution of time-averaged velocity vectors of the OTA-1 pump.

Distribution of time averaged velocity is shown in Figure 24. Larger vectors, coloured red, have the origin at the tip of the rotor blades where maximum velocity magnitudes occur. Detail of the figure shows distribution of a velocity field around the upper breakwater. For optimal

operating point the inflow into the outflow channels is smooth.
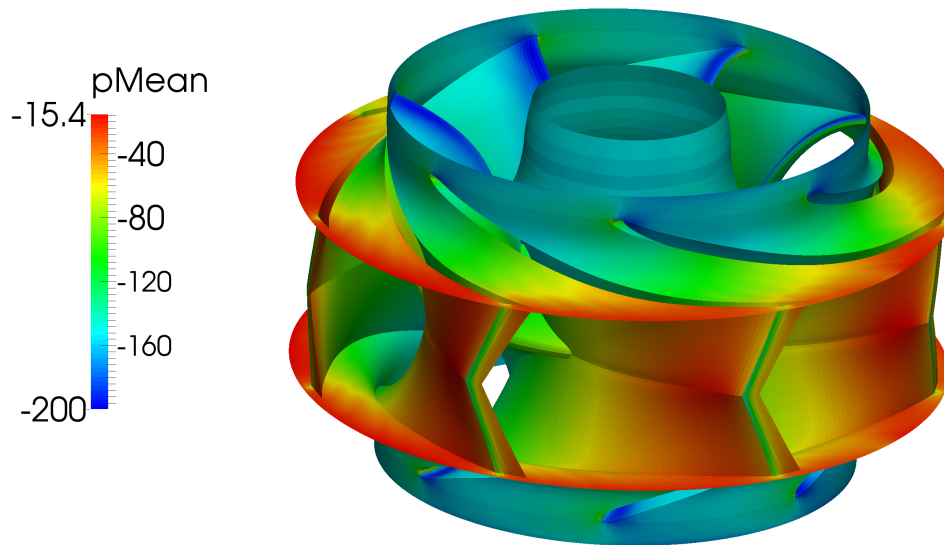
Figure 25: Distribution of time-averaged pressure on rotor of the OTA-1 pump.

Pressure distribution on rotor blades, casing and shaft is shown in Figure 25. Zones of higher pressure occur at the outlet parts of the rotor with highest values at the tip, before the rotor blade is cut. Sharp edges of the rotor blades are causing flow separation at the end of the blades and because of that drop of the pressure occurs at the tip of the blades where blades are cut. The lowest pressure in the whole domain occurs at the leading edge of the rotor blades. This information may be important in order to assess cavitation probability.

Flow separation from the tip of the blade results in highly turbulent flow. Due to separation all turbulent parameters are increased in the wake of the rotor blades. Distribution of turbulent kinetic energy can be seen in Figure 26 where the zones of higher turbulent kinetic energy occur in the wakes of the rotor blades and in the outflow channels. Detail of the figure shows recirculation in the outlet pipe. Dissipation rate of turbulent kinetic energy has the highest values around the rotor blades as shown in the Figure 27.
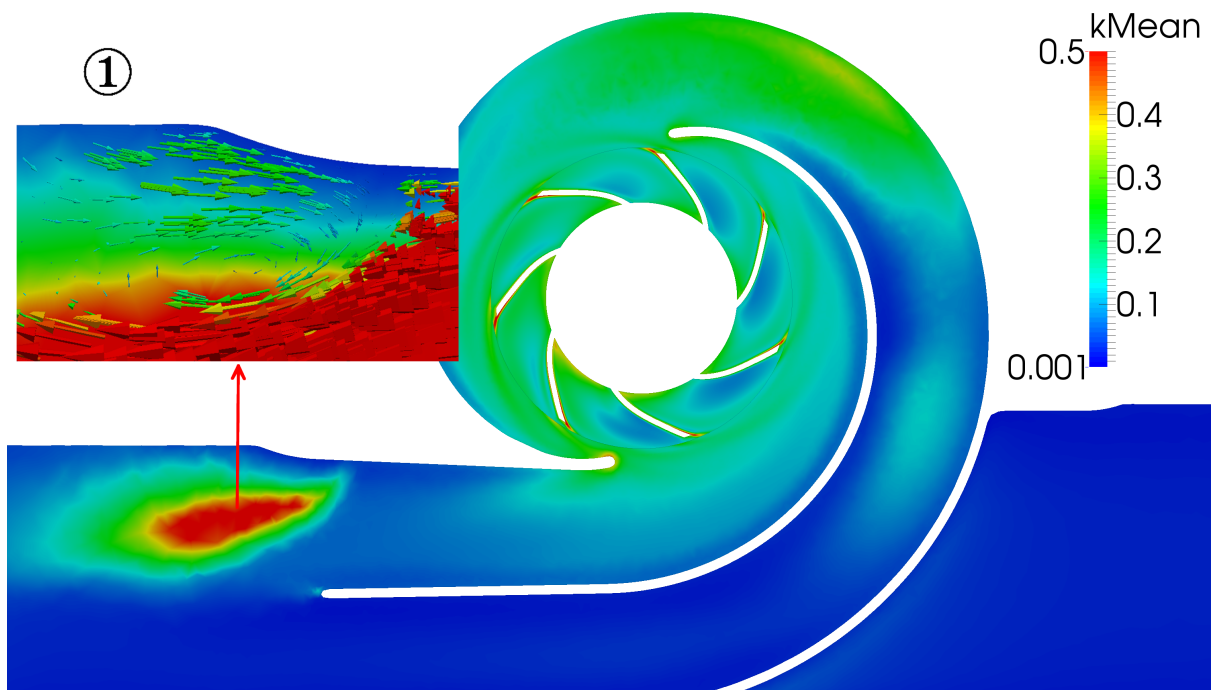
Figure 26: Distribution of time-averaged turbulent kinetic energy.
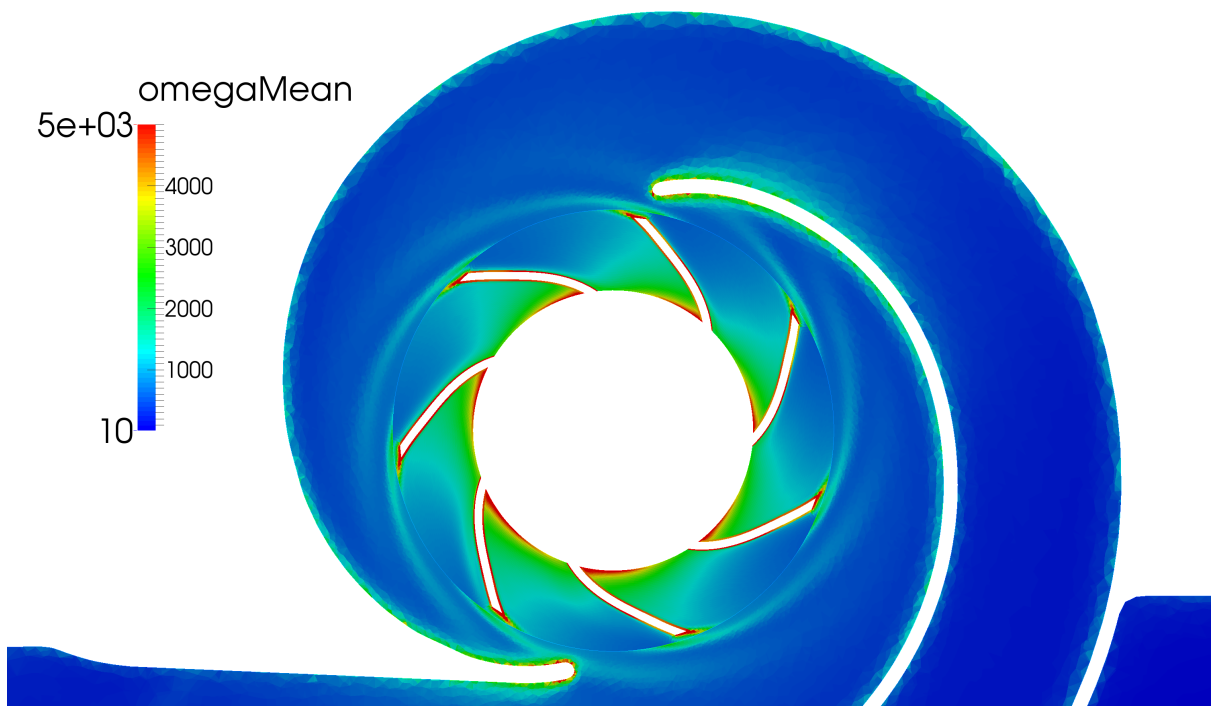
Figure 27: Distribution of time-averaged specific turbulent kinetic energy dissipation rate on rotor of the OTA-1 pump.

Power curves for different operating points

Performance curves presenting power, head and efficiency are obtained by a function object called turboPerformance for three operating points. Figure 28 shows graphs of pump power as a function of time for first operating point defined by volumetric flux 14.5 m^3/min. For this operating point efficiency of pump is highest. In a lower subfigure an end detail of a pump power is shown, in which oscillation for one revolution of rotor can be seen. Required time for one revolution of rotor equals 0.046 s. In this period of time seven rotor blades pass near the two breakwaters creating oscillations in power graphs. Upper subfigure shows power for whole simulated time. It can be seen that pump power repeats periodically in time what is one of the indicators that simulation results have converged to periodic steady-state.
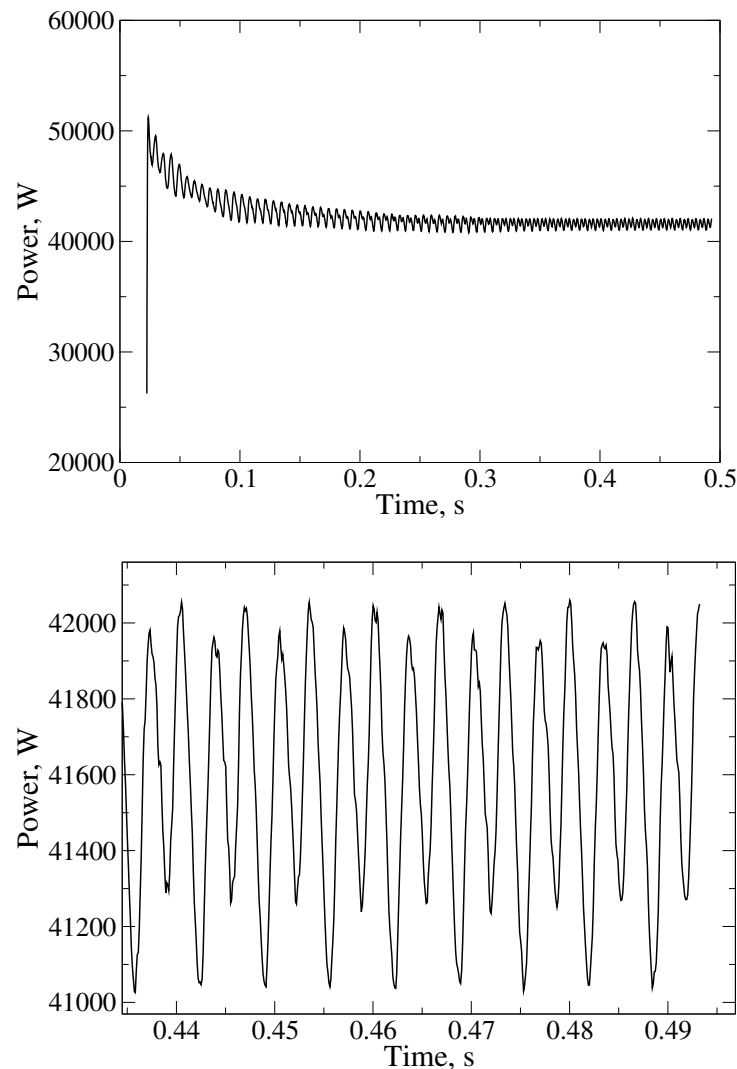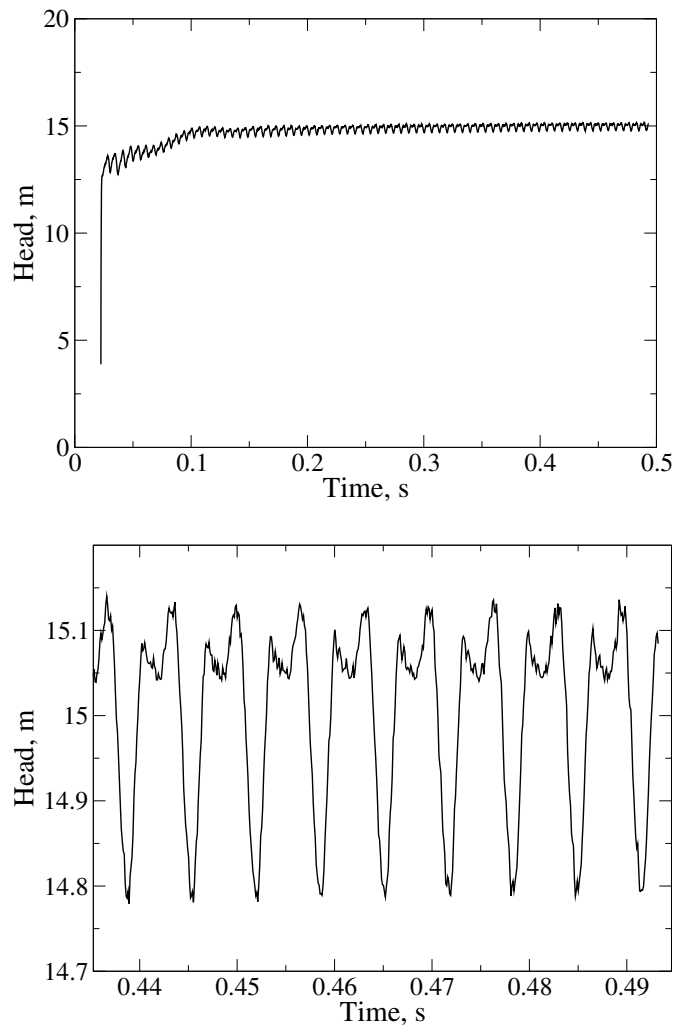

Figure 28: Power as a function of time for first operating point.

Second operating point is defined by a lower volumetric flux of 11.6 m^3/min, resulting in a lower efficiency. Figure 29 shows graphs of a pump power for second operating point. It can be seen that simulation for second operating point was performed for shorter period of time than simulation of first operating point due to limited computational resources. It can also be seen that the periodic steady-state is not fully achieved. First operating point is studied thoroughly, while the other operating points are studied to obtain $Q - H$, $Q - P$ and $Q - \eta$ curves and to present differences in a flow for nominal and partial load.
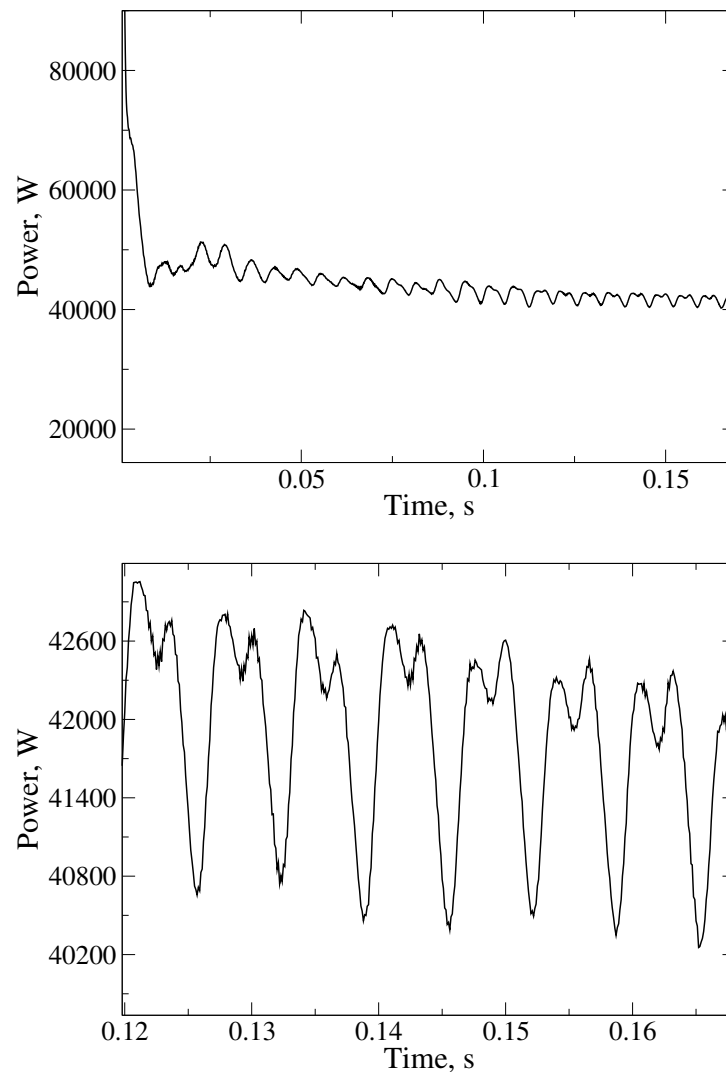
Figure 29: Power as a function of time for second operating point.

Pump power for third operating point is shown in Figure 30. This operating point is defined with volumetric flux that is greater than the first operating point and equals 17.4 m^3/min. It can be seen, that the simulated period of time is not sufficient for results to become quasi-stationary for this operating point. From presented graphs of power in this section can be seen that the power oscillates around the value of 40 kW.
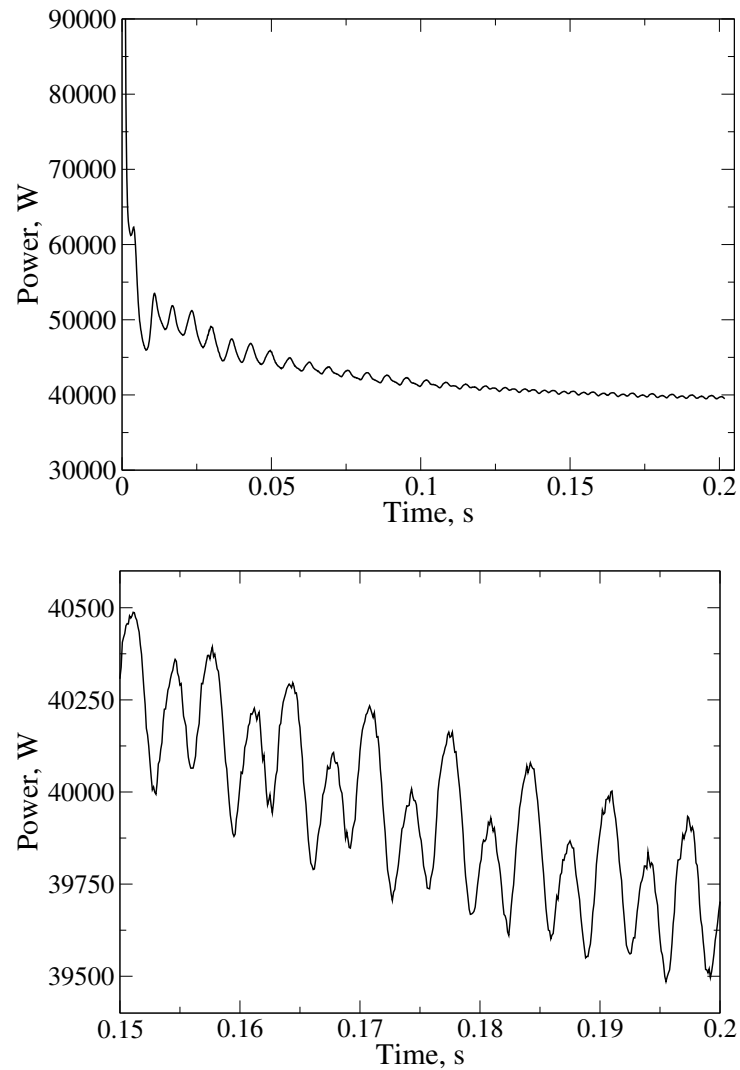
Figure 30: Power as a function of time for third operating point.

Head curves for different operating points

Figure 30 shows a pump head as a function of time for the first operating point which is defined by volumetric flux of 14.5 m^3/min. Oscillation of pump head is also effected by a rotational speed of rotor, number of rotor blades and a number of outflow channels in the same way as power. Upper subfigure shows a change of head for the whole period of simulated time. Oscillations for one revolution of rotor are given in the lower subfigure and it is evident that the results are quasi-stationary and therefore convergence is achieved. Average head for first operating point equals 15 m.

Figure 31: Head as a function of time for first operating point.

Second operating point is defined by a lower volumetric flux of 11.6 m^3/min. Hence, pump head for second operating point should be higher, as demonstrated in Figure 32. According to lower subfigure, average head for second operating point equals 17.4 m.
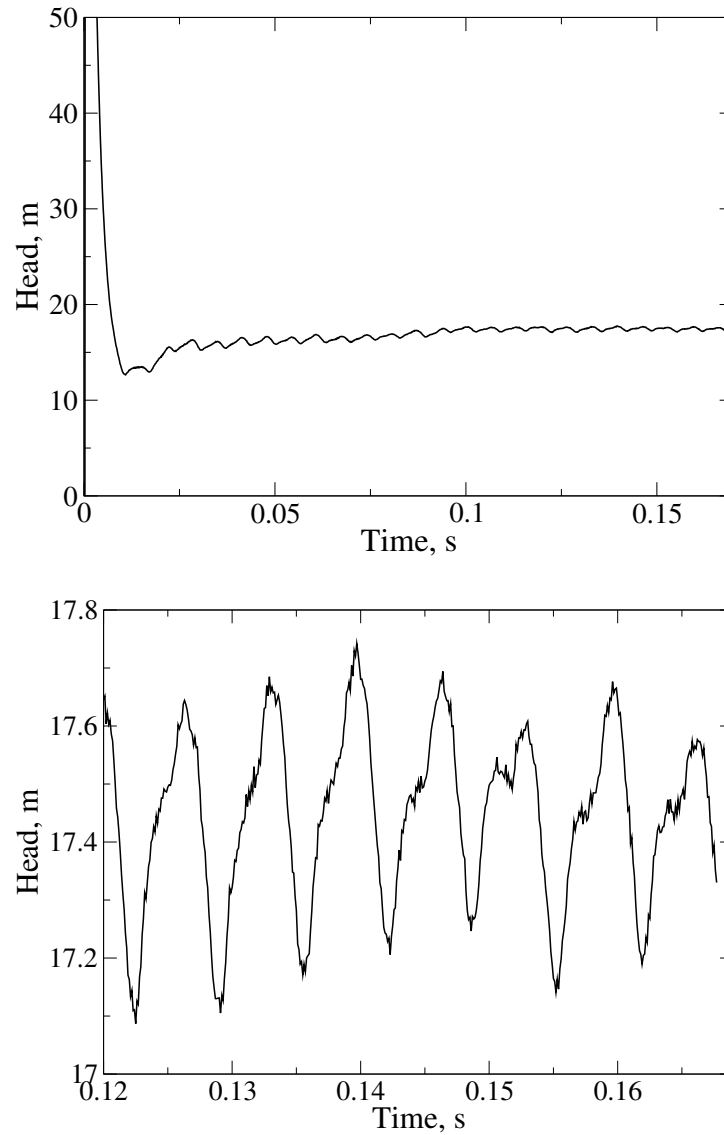
Figure 32: Head as a function of time for second operating point.

Third operating point is defined with greater volumetric flux than first operating point. Volumetric flux equals 17.4 m^3/min and therefore head is lower. Graph of head can be seen on Figure 33 and according to lower subfigure average head equals 11 m. Simulated period of time is not sufficient to obtain converged simulation results, as evident from lower subfigure, but results give approximation of head on which operating points of pump can be compared.
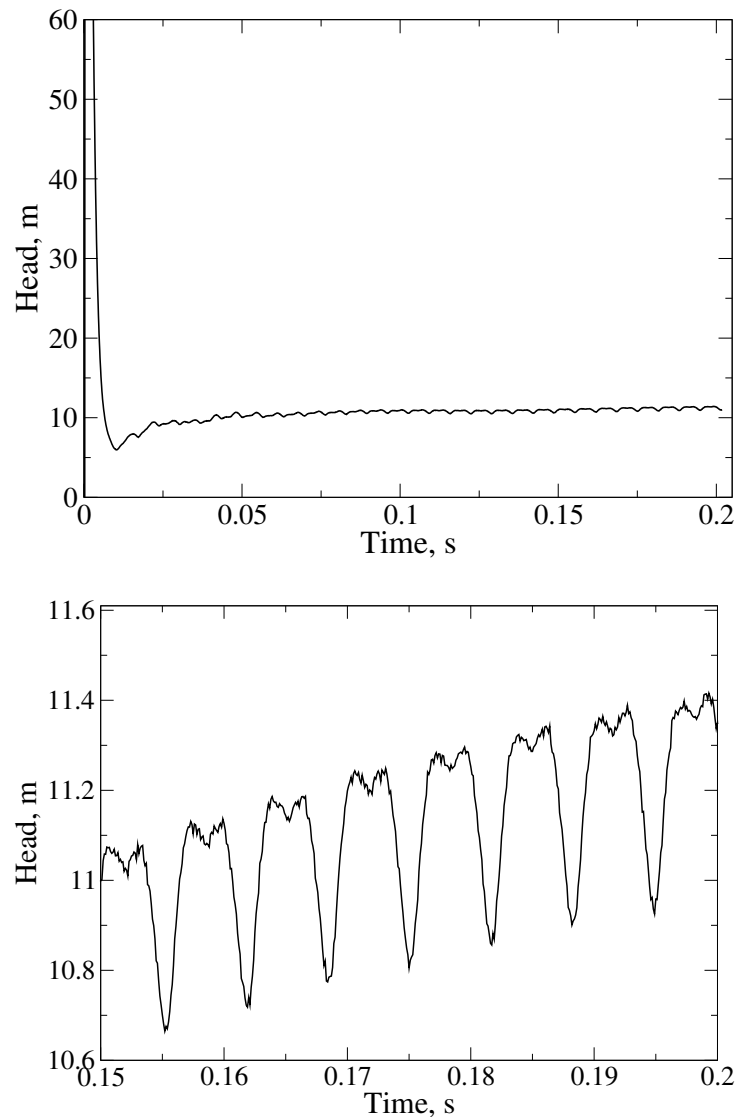
Figure 33: Head as a function of time for third operating point.

Efficiency curves for different operating points

First operating point has highest efficiency because all the parts of the geometry that affect fluid flow are designed for this operating point. Hence, all the other simulated operating points will have lower efficiency due to non-optimal geometry of pump for partial load. In Figure 34 efficiency graphs as a function of time are shown for the first operating point. Oscillation of efficiency is also effected by rotational speed, number of rotor blades and number of outflow channels. Average efficiency, according to lower subfigure, equals 85%.
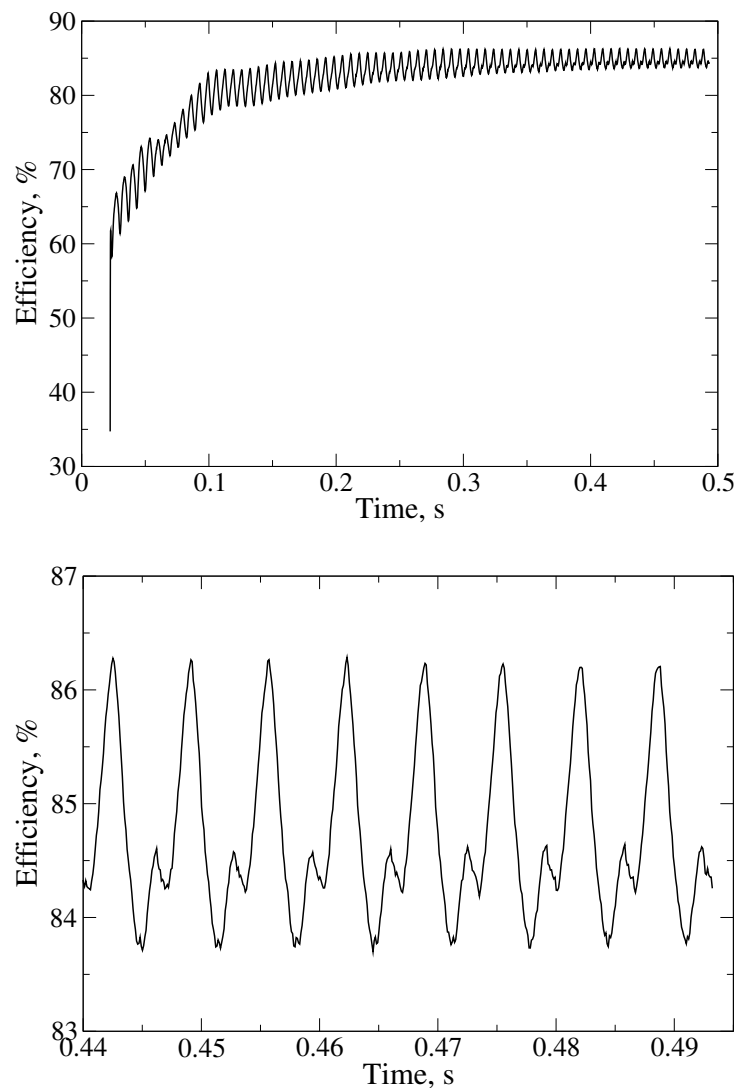
Figure 34: Efficiency as a function of time for first operating point.

Second operating point is a partial load operating point and therefore efficiency is lower. Graphs of efficiency for second operating point are shown in Figure 35. According to graph shown in lower subfigure, average efficiency equals 79%.
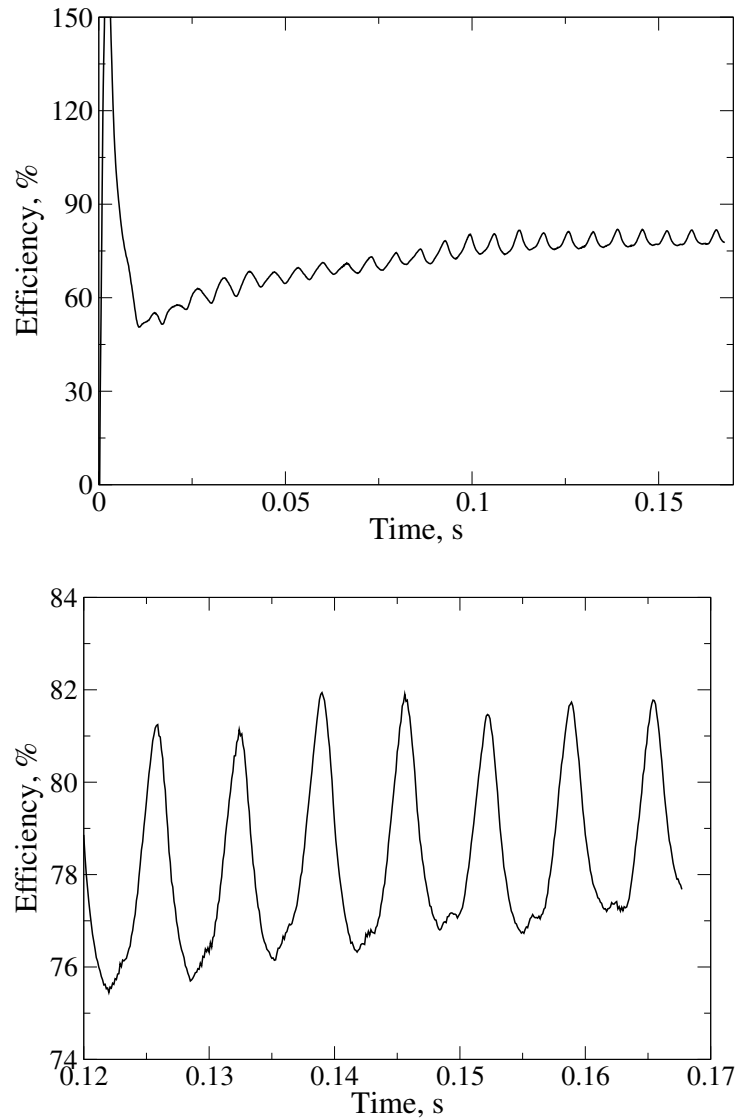
Figure 35: Efficiency as a function of time for second operating point.

Third operating point is also a partial load. Graphs of efficiency are shown on figure 36 and according to lower subfigure average efficiency is 78%. Simulated period of time is not sufficient to obtain quasi-steady state results but they provide information on whose basis different operating points can be compared.
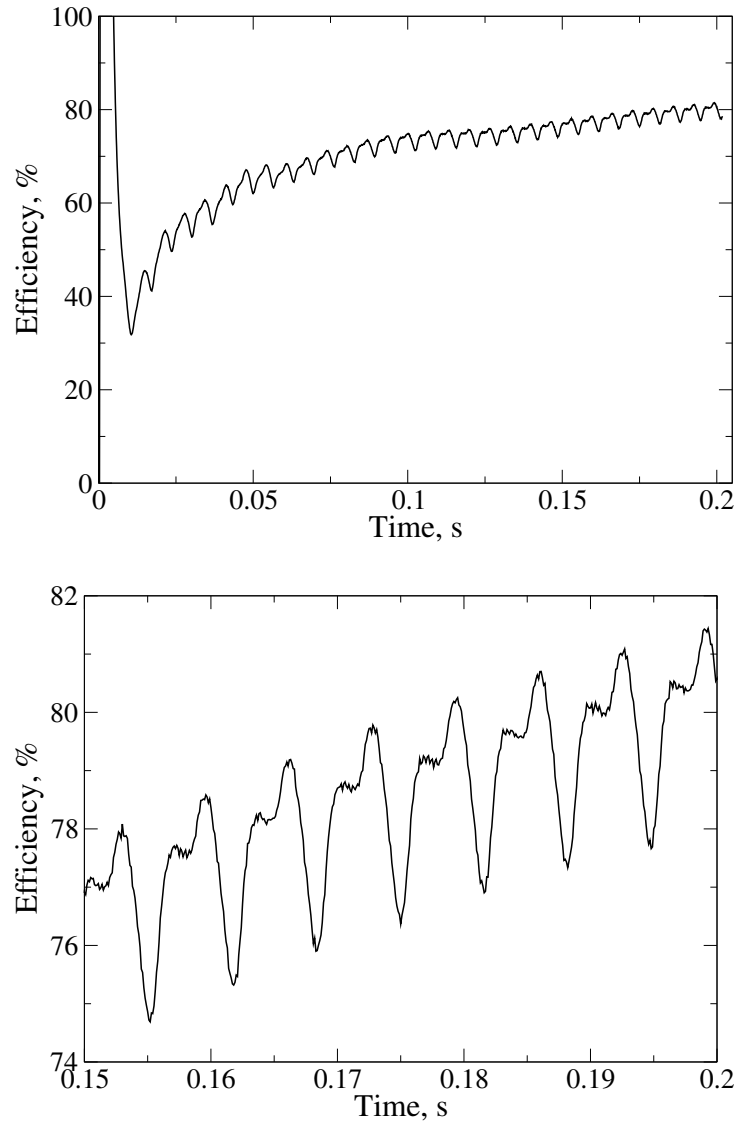
Figure 36: Efficiency as a function of time for second operating point.

5.2.2   Multiple Reference Frame Simulation with General Grid Interface

Oscillation of power, head and efficiency are not always important in engineering applications and sometimes it is more important to obtain approximate results in a shorter period of real time required for simulation. For such cases Multiple Reference Frame (MRF) model is better than transient simulation. MRF model simulates fluid flow in a pump with fixed position of rotor where the time derivative term in a mathematical model is ignored. Ignoring the time derivative term and assuming fixed position of rotor in a pump have negative effect on the simulation results, but the time required to obtain such results is significantly lower. MRF simulations for three operating points are presented in this section. Generation process of $Q - H$ and $Q - \eta$ operating curves is also covered. These operating curves are important for practical application of pump because they help user to predict what will be amount of volumetric flux, efficiency and the power of a pump for a given resistance of pipeline.

To set-up a case for MRF simulation boundary and initial conditions are specified in the same way as for transient simulation with an exception in velocity boundary conditions for patches that are rotating in the transient simulation. Boundary condition for such patches are changed from movingWallVelocity to fixedValue with the uniform value of (0, 0, 0). MRF simulation is a steady-state simulation and therefore initial conditions do not influence simulation results, but they have effect on required time for result convergence. As a convergence indicator pump head is monitored and the convergence is assumed to be achieved if oscillations in head are lower than 1%. Another difference in case set-up is that cell zone with assigned angular velocity is not moving. Hence, dynamicMeshDict is replaced with MRFZonesDict with angular velocity corresponding to 1300 rpm. Rotor-stator interface used in MRF simulations is GGI.

Flow fields and turbulence parameters

Figure 37 shows velocity field around rotor blades and in the outflow channels of the pump. Difference between transient simulation is that the wakes behind the rotor blades can be seen. In transient simulation this is not the case due to time-averaging of results what causes smearing of the fields. Detail of the figure shows a velocity distribution in a wake which is, due to ignoring of time derivative term and assumption of fixed rotor zone, unphysical. A silver circular sector that occurs in a figure represents GGI interface between rotor and stator. It can also be seen that velocity distribution has a jump in the value from rotor to stator cell zone due to numerical error introduced by the interface.
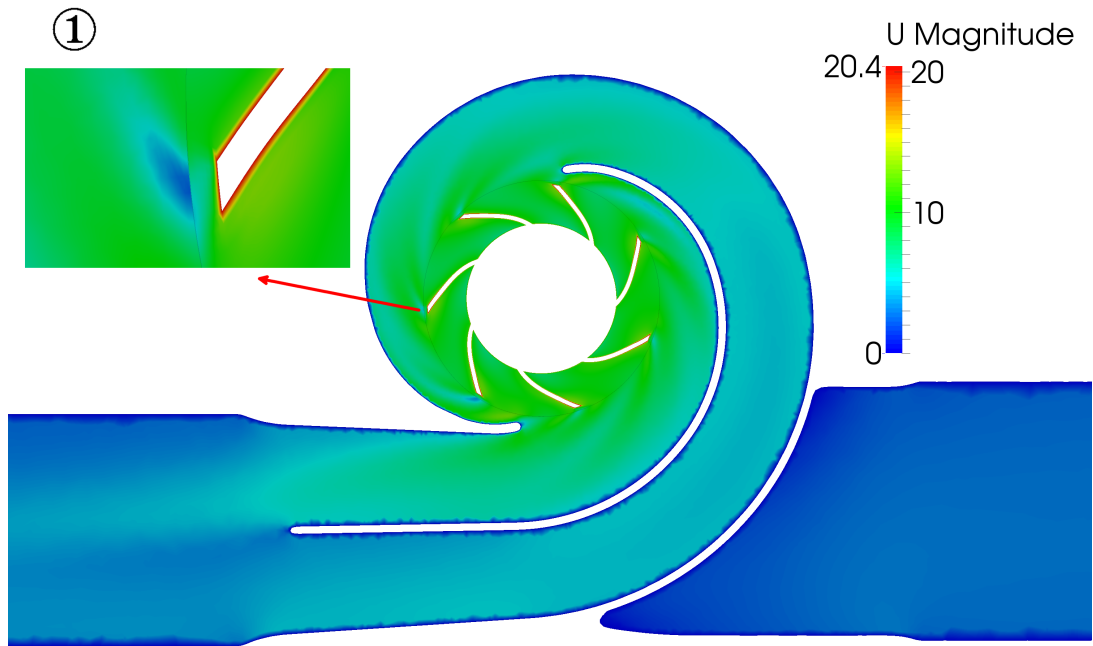
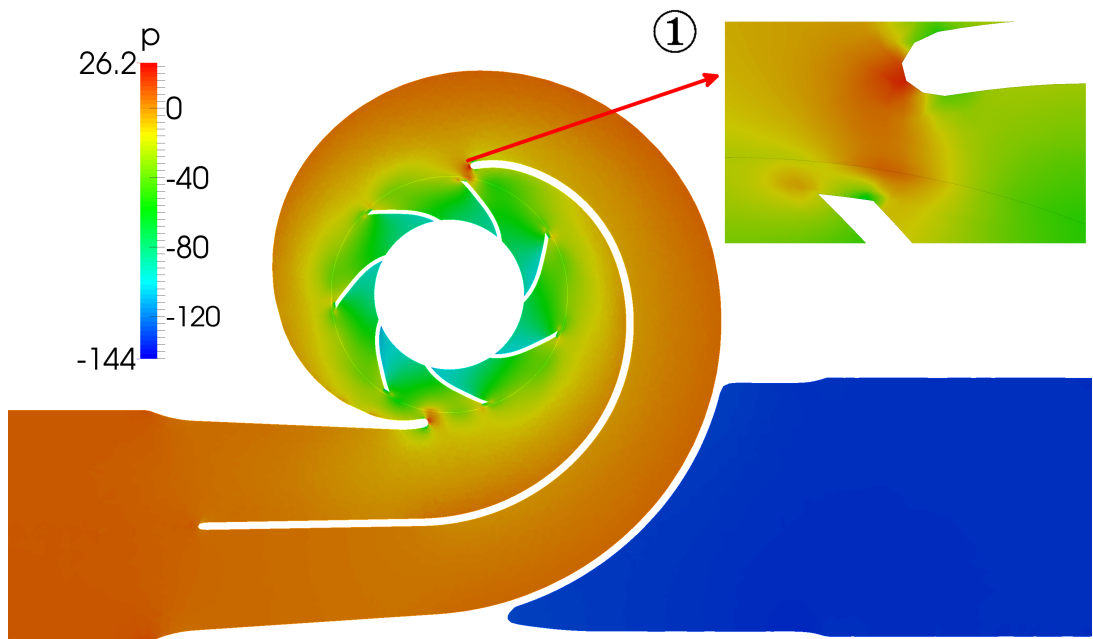Figure 37: Velocity field of the OTA-1 pump obtained by MRF simulation.

Figure 38: Pressure field of the OTA-1 pump obtained by MRF simulation.

Pressure field around the rotor is shown in Figure 38. Detail of the figure shows a pressure distribution around the upper breakwater of the pump. From the detail, it can be seen that the transition between the rotor and stator cell zone is smoother for pressure than for velocity field. Pressure maximum and minimum values occur in the same places as for transient simulation. Maximum values occur at the breakwater due to stagnation pressure and minimum values occur at the leading edge of the rotor blades.

Flow distribution around the rotor is shown in Figure 39. Larger vectors, coloured red, have the origin at the tip of the rotor blades due to rotation of the rotor cell zone. The detail of the figure shows a smooth flow over the upper breakwater for operating point with maximum efficiency.
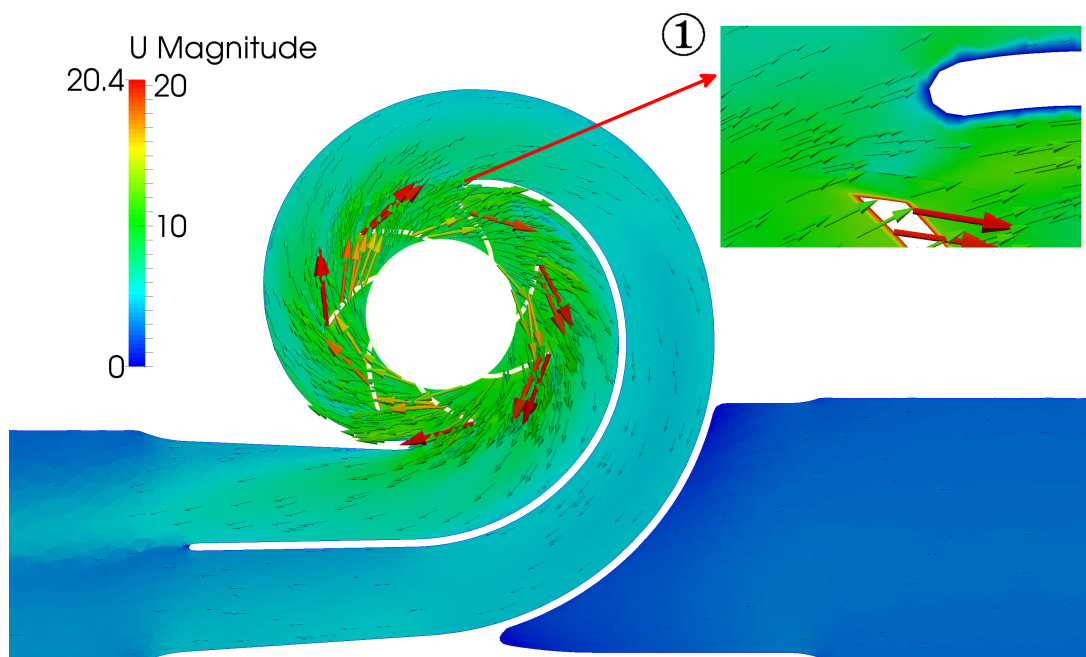
Figure 39: Flow distribution around rotor of the OTA-1 pump obtained by MRF simulation.

Pressure field distribution on rotor can be seen in Figure 40. If the pressure field is compared to one obtained by transient simulation it can be seen that the lowest value of pressure is the same, while the maximum value on rotor is lower for MRF simulation. Separation of the flow occurs due to sharp edges of rotor blades.
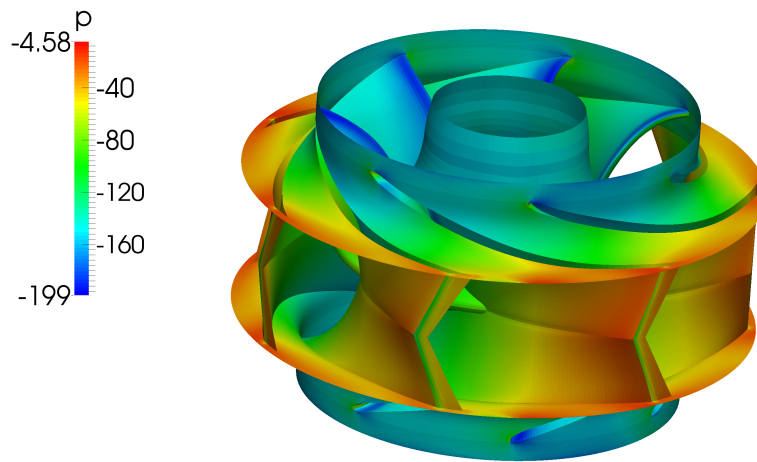
Figure 40: Pressure field on rotor of the OTA-1 pump obtained by MRF simulation.

Vortical structures in the flow can be indicated by the Q-contour which is one of the vortex identification schemes. Q-contour is defined by following expression:

$$Q = \frac{1}{2}(|\mathbf{A}|^2 - |\mathbf{S}|^2|), \tag{92}$$

where $\mathbf{A}$ is antisymmetric and $\mathbf{S}$ is symmetric part of the velocity gradient tensor. According to Eq. (92), Q-contour is a scalar which represents a difference between magnitudes of antisymmetric and symmetric part of the velocity gradient. Antisymmetric part represents rotation, while the symmetric part represents deformation of a fluid particle. Criterion for vortex appearance in the fluid flow is for the antisymmetric part to be greater than symmetric part of velocity gradient. Greater the Q-contour value, higher the energy of vortex that occurs in the area around the observed fluid particle. In Figure 41, Q-contour at the rotor blades is shown where the value of Q equals 150,000. If the value of Q-contour decreases, more vortices appear due to smaller energy of vortices that satisfies defined Q-contour. As an example, in Figure 42 is shown a field of Q-contour with the value of 2,000. Besides the tip vortices that have the axis parallel to the rotation axis of the rotor, vortices with radial axis appear at the outlet of the rotor. From Figure 43, is can also be seen that the turbulence has higher intensity at the breakwaters where the flow is separated.
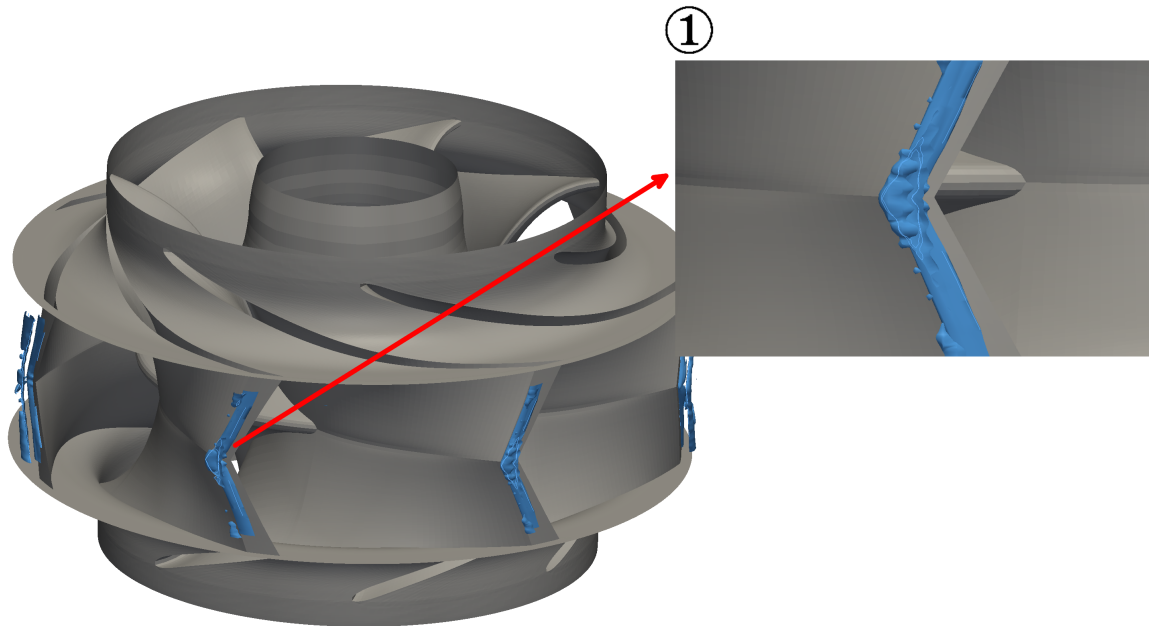
Figure 41: Q=150,000; for indication of tip vortices.
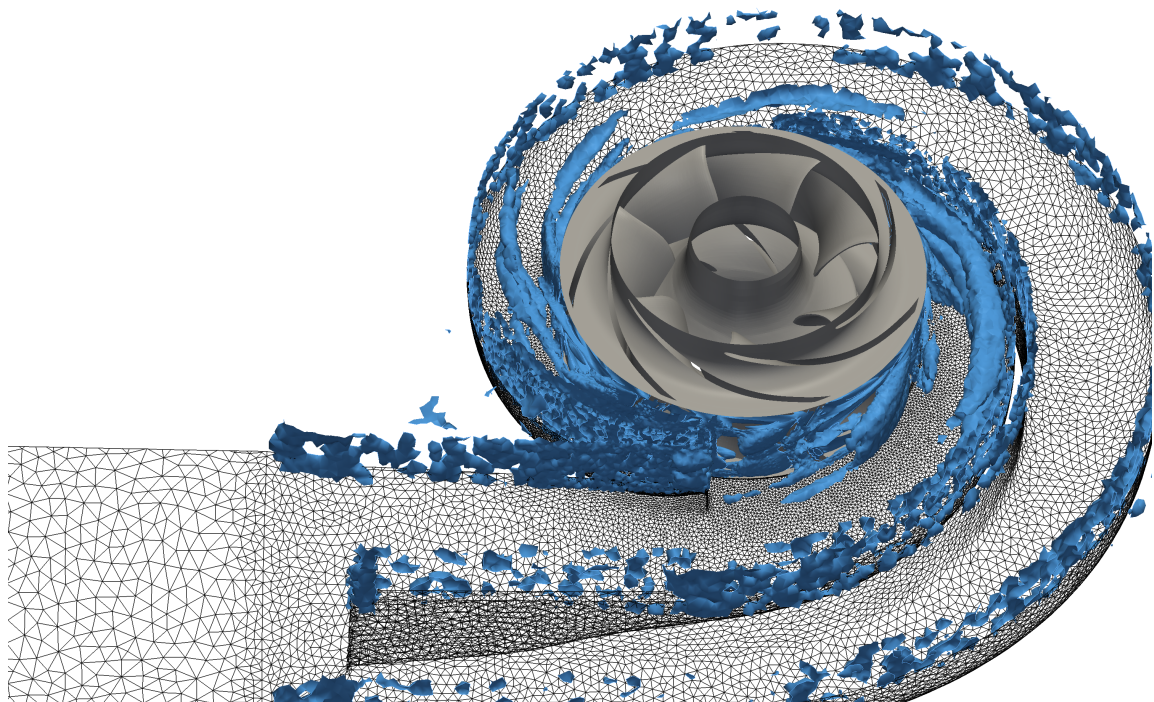
Figure 42: Q=2,000; for indication of other vortical structures.

Indication of vortices shown by Figure 42 can be also viewed by distribution of turbulence parameters around the rotor and in the outflow channels. In Figure 43 turbulence kinetic energy is shown, where higher values of turbulent kinetic energy indicate the zone of vortices with higher kinetic energy.
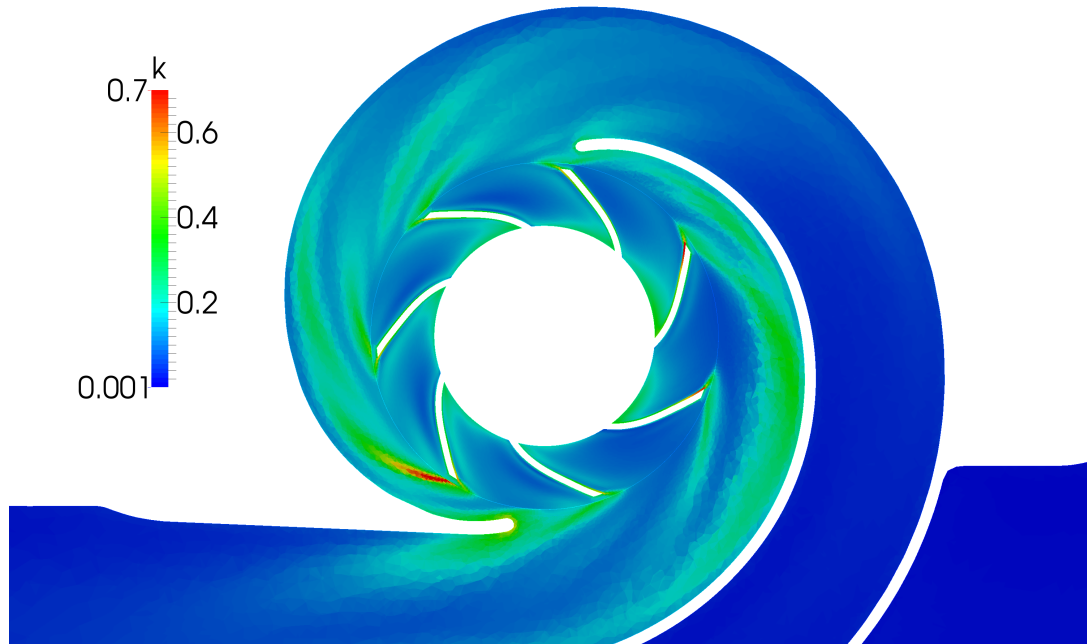

Figure 43: Turbulence kinetic energy of the OTA-1 pump obtained by MRF simulation.

Performance curves

In Figure 44, graphs of pump head for first operating point are shown. From second subfigure can be concluded that the oscillation of head equals 0.05%. Value of the head equals 14.47 m, power is 39013.9 W and efficiency is 87.1% for 1600th iteration.
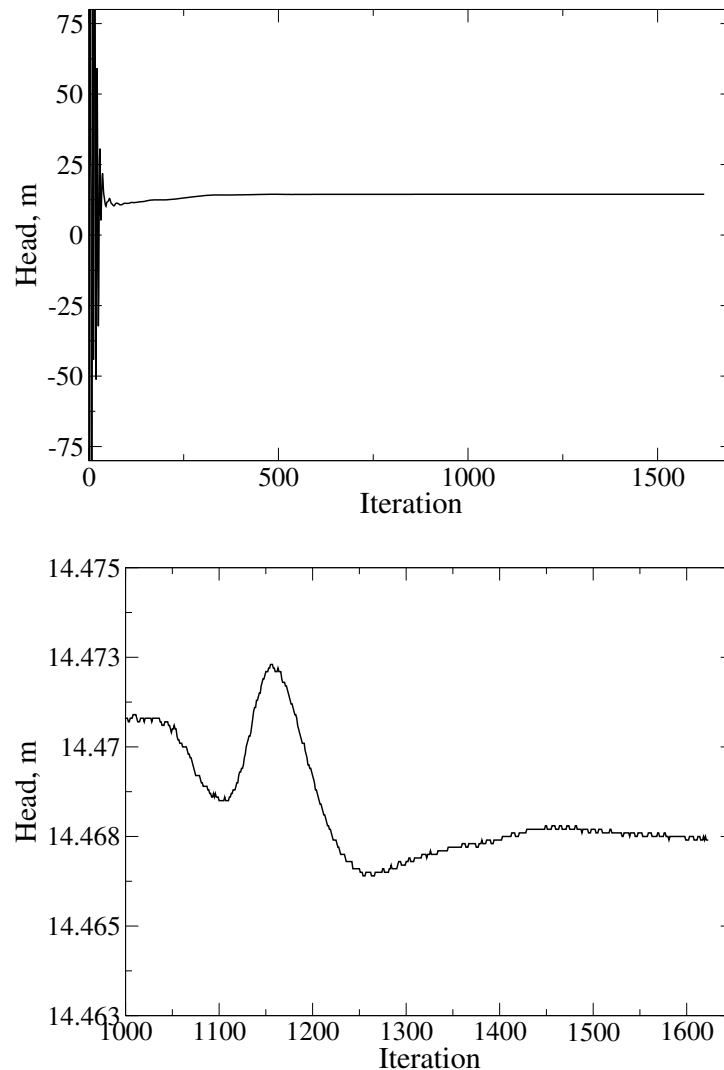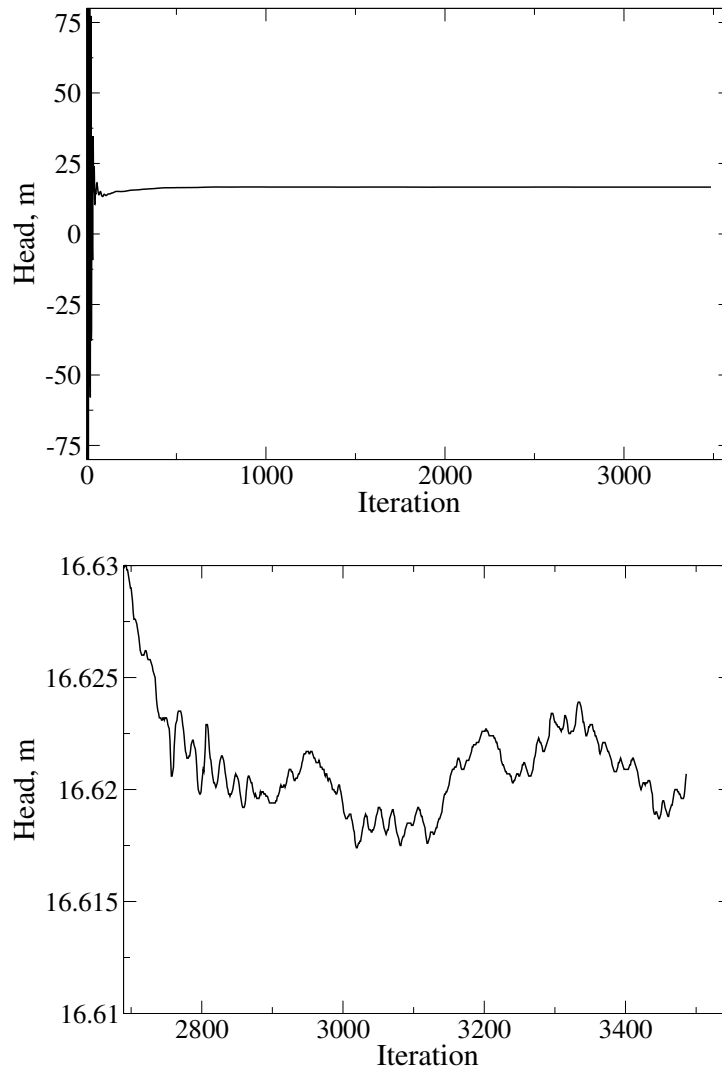

Figure 44: Convergence graphs for MRF simulation of the OTA-1 pump for first operating point.

Second operating point is defined with lower volumetric flux than the first operating point and therefore, obtained value of head is greater. Lower subfigure of Figure 45 shows that the relative error of head equals 0.06%. Value of the head equals 16.62 m, power is 37710.7 W and efficiency is 82.8% for 3500th iteration.
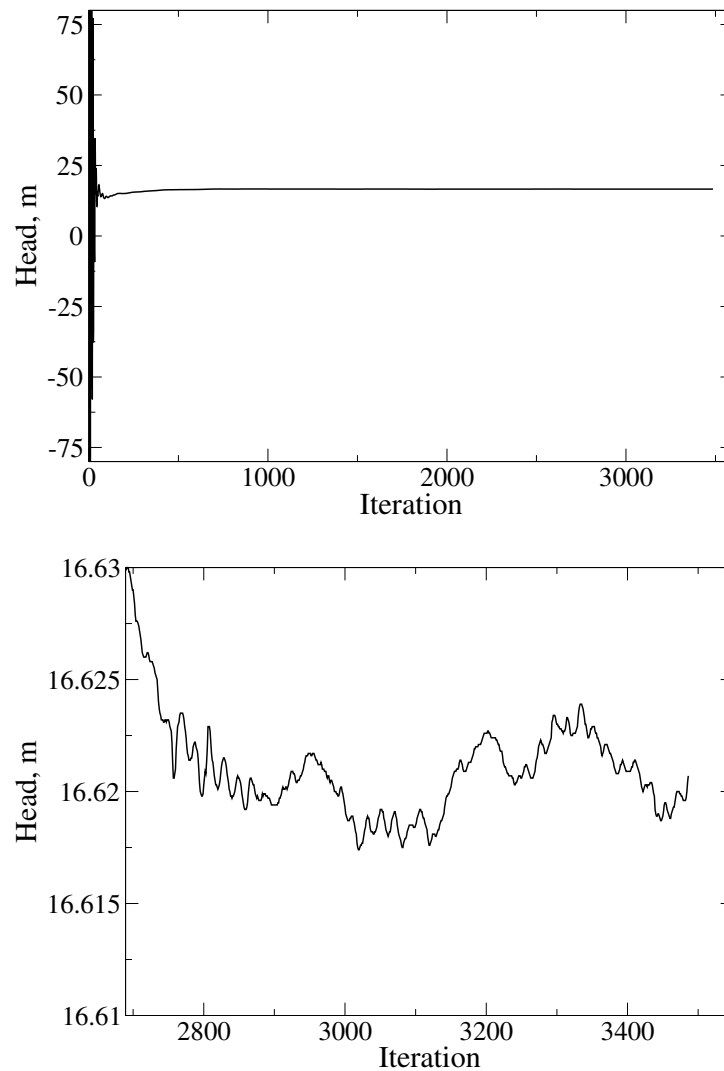
Figure 45: Convergence graphs for MRF simulation of the OTA-1 pump for second operating point.

Third operating point is defined with higher volumetric flux than the first operating point and therefore obtained value of head is lower. Lower subfigure of Figure 46 shows that the oscillation of head equals 0.02%. Value of the head equals 11.17 m, power is 37623.8 W and efficiency is 83.7% for 2600th iteration.

Figure 46: Convergence graphs for MRF simulation of the OTA-1 pump for third operating point.

From the results of head and efficiency obtained by simulations of different operating point, $Q - H$ and $Q - \eta$ curves are generated by an approximation of the points with a parabola. Both curves are shown in a single diagram, as shown in a Figure 47.
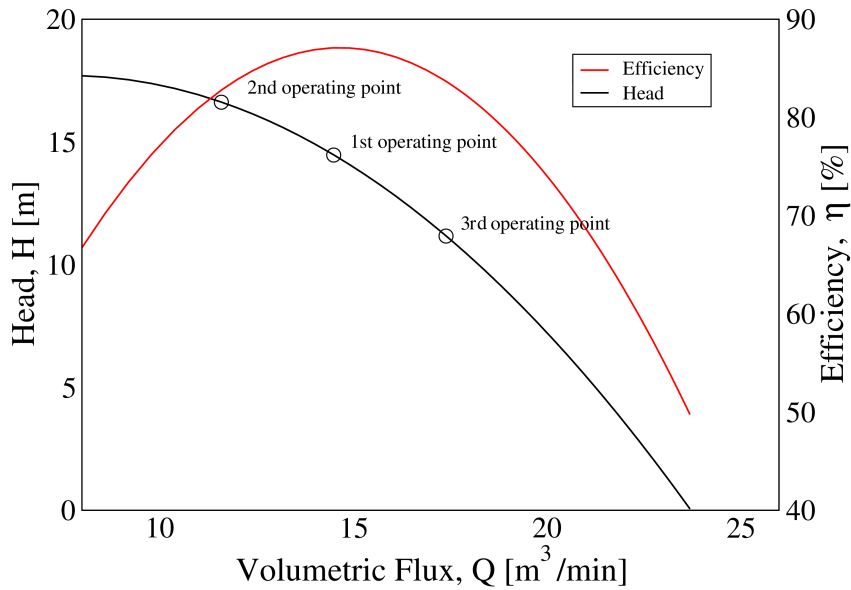
Figure 47: $Q-H$ and $Q-\eta$ performance curve of the OTA-1 pump.

5.2.3   Multiple Reference Frame Simulation with Mixing Plane Interface

Second method to couple rotor and stator cell zones is mixing plane interface. Mixing plane interface is based on circumferential averaging of flow variables in one or more stacked ribbons. One of the criterion which indicates if the obtained results are valid is circular distribution of the variable field over the master and shadow patch of the interface. End time of simulation was declared when oscillations of the head became lower than 2%.

To set up a case for MRF simulation with mixing plane interface boundary and initial conditions are defined in the same way as for previous simulations with an exception of boundary condition at the interface. For interface patches GGI boundary condition is replaced with mixingPlane. To define a mixing plane, ribbon and stack axis have to be specified. Ribbon axis defines the direction in which circumferential averaging is performed and the stack axis defines in which direction ribbons of averaged fields are stacked. Another difference for this simulation compared to MRF simulation with GGI is the linear solver set for pressure calculation. In MRF simulation with GGI, AMG solver is used with the Gauss-Seidel smoother, while in the simulation with mixing plane interface BiCGStab is used. AMG solver, in the official version of OpenFOAM used in this thesis, is not implemented to work with mixing plane interface. This highly effected the time required for simulation to be performed because AMG solver makes the results converge faster. Effect on the results should not be present due to change in linear system solver.

Flow fields and turbulence parameters

Simulation with mixing plane is performed only to show differences between GGI and mixing plane interface and therefore, only operating point with maximum efficiency is simulated. This operating point is defined with the volumetric flux value of 14.5 m^3/min. Figures presented in this subsection show details of results around rotor and in outflow channels.
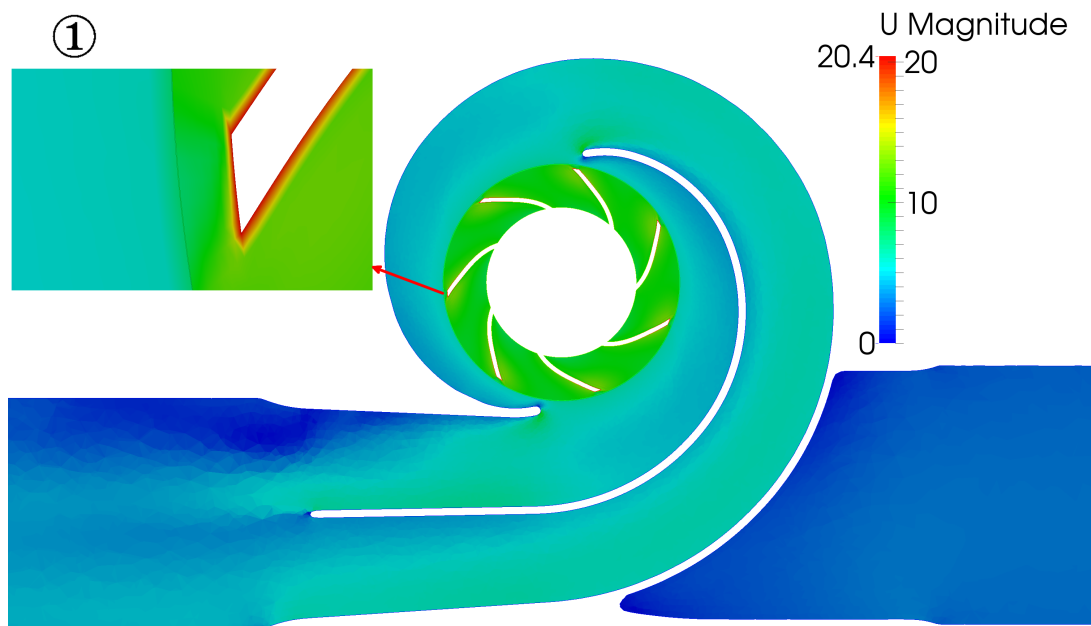

Figure 48: Velocity field of the OTA-1 pump with mixing plane interface.

In Figure 48 is shown a velocity distribution around rotor and in the outflow channels with the detail showing the velocity distribution around the rotor-stator interface. Wakes of the rotor blades acting upon stator do not occur in simulation with mixing plane interface due to circumferential averaging at the end of the rotor cell zone. It can also be seen that the maximum velocity is equal to the one obtained with GGI due to the same rotational speed.

Pressure field distribution is shown in Figure 49 with detail showing distribution around the upper breakwater and around the rotor-stator interface. Jump in pressure field in transition from rotor to stator cell zone is due to circumferential averaging and introduced numerical error of mixing plane interface. The detail also shows that the distribution of the pressure over the breakwater is similar to pressure distribution in flow over an arbitrary airfoil. Similar behaviour can be observed around the lower breakwater.
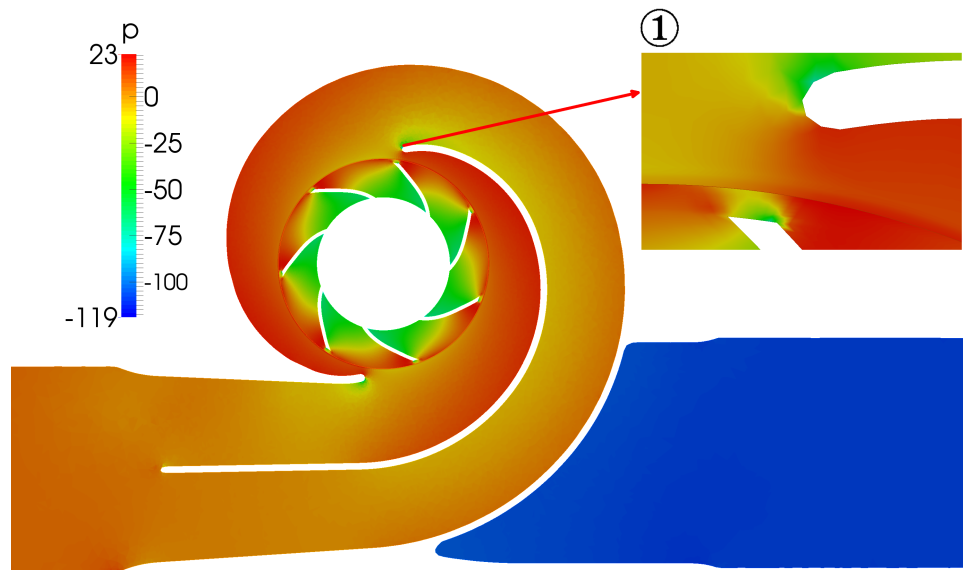
Figure 49: Pressure field of the OTA-1 pump with mixing plane interface.

Distribution of velocity vectors at the interface is the reason why this method is not suitable for flow calculation of this pump. As shown in the detail of Figure 50, velocity vectors do not have desired angle at the outlet of the rotor cell zone. This results in a flow over the breakwaters and in the outflow channel flow which is not smooth.
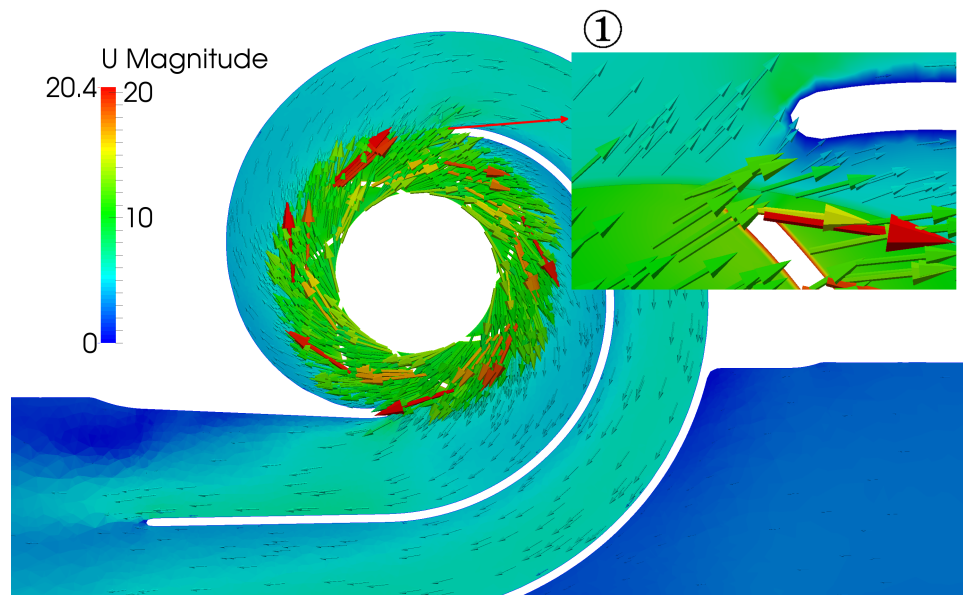

Figure 50: Velocity vectors of the OTA-1 pump with mixing plane interface.

Comparison with MRF with GGI is shown in Figure 51. Subfigure 51a shows a flow distribution over a breakwater, when the rotor-stator interface is GGI, while the subfigure 51b shows a flow distribution over a breakwater with mixing plane interface. Such flow distribution over breakwaters and inflow channels results in severe head, and thus efficiency

drop.

(a) GGI   (b) Mixing plane interface
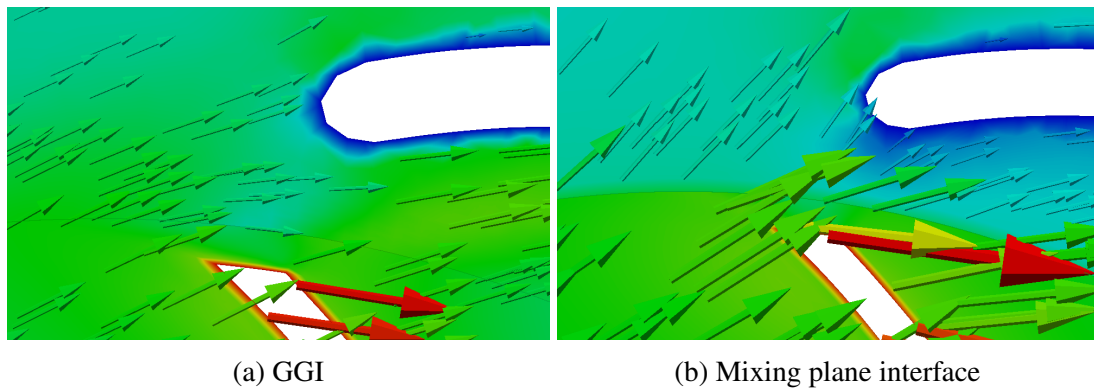
Figure 51: Comparison of flow around the breakwater.

Even though mixing plane gives non-physical results of a flow at the transition between rotor and stator cell zone, recirculation in the outlet pipe is in the same spot as for the transient simulation. In Figure 52, turbulent kinetic energy field can be seen with the detail showing the recirculation in the area of high turbulent kinetic energy.
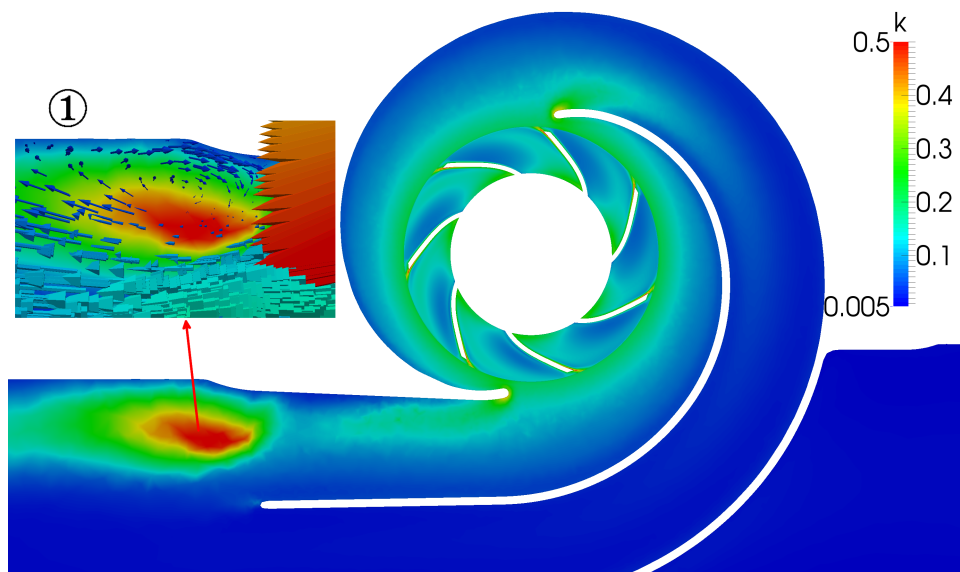
Figure 52: Turbulent kinetic energy field of the OTA-1 pump with mixing plane interface.

Distribution of pressure over the mixing plane interfaces is shown in the Figure 53. Subfigure 53a shows a pressure distribution at the inlet of rotor, while the subfigure 53b shows a pressure distribution at the outlet of rotor. Velocity distribution over the interfaces is similar to pressure distribution as shown in Figure 54. In the left subfigure, velocity distribution at the rotor inlet is shown, while in the right subfigure shows a velocity distribution over the rotor outlet.

(a) Rotor inlet

(b) Rotor outlet
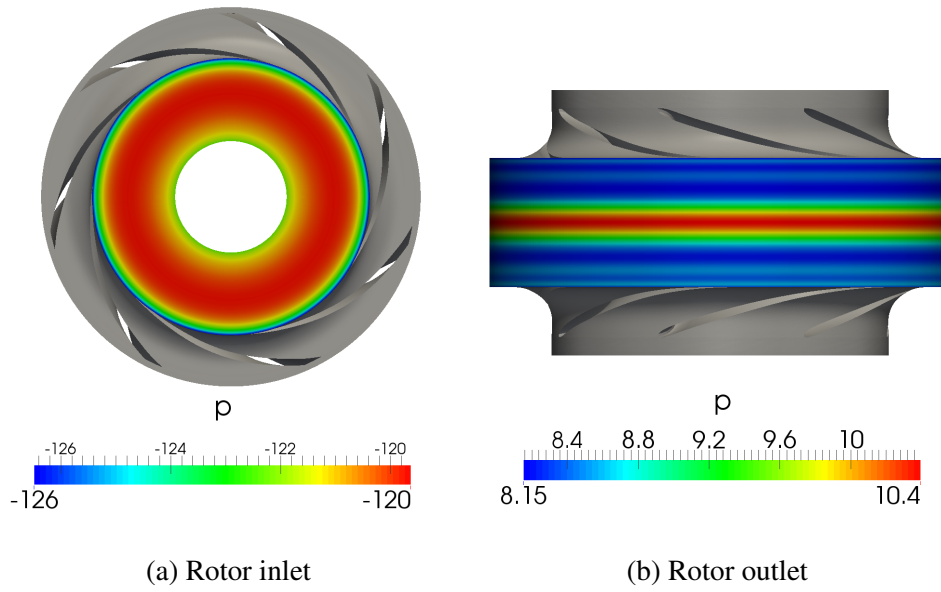
Figure 53: Distribution of pressure at the mixing plane interfaces.

(a) Rotor inlet

(b) Rotor outlet
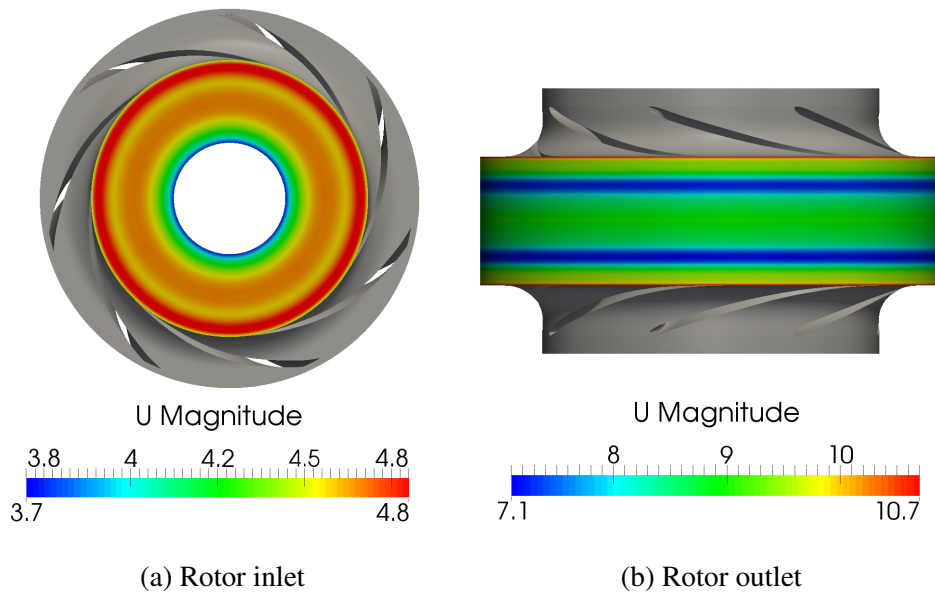
Figure 54: Distribution of velocity at the mixing plane interfaces.

Convergence of results

Convergence of results is monitored using the head graph. Criterion for the converged results is the maximum oscillation of head equal to 2%. In Figure 55 convergence graphs are shown, where from the lower subfigure can be seen that the maximum oscilation of head equals 1.7%. For the 3400th iteration pump head equals 11.92 m, power is 46918.1 W and efficiency is 59.7%. Compared to MRF simulation with GGI for first operating point it can be seen that efficiency of the pump dropped by 27.4% due to circumferential averaging of mixing plane. Therefore, mixing plane interface is not recommended for simulation of turbomachinery with geometry where the stator blades or stator casing is close to the rotor blades.
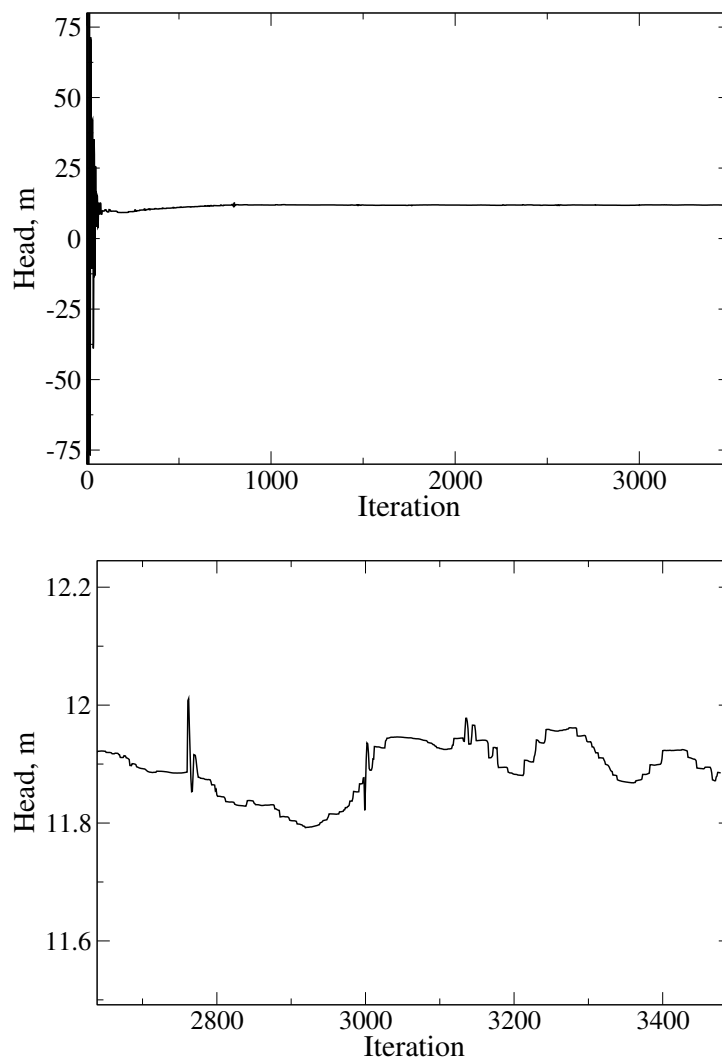
Figure 55: Convergence graphs for MRF simulation of the OTA-1 pump with mixing plane interface.

5.2.4   Comparison Between Segregated and Coupled Solver

Advantage of coupled solver is that momentum and pressure equation are solved at the same time and therefore convergence of the results is faster. On the other hand, solving both equations at the same time requires more memory for computer to be able to run the simulation. Coupled solver tested for the purposes of this thesis solves the MRF model with the GGI interface between the rotor and stator interface. In this subsection, only the number of iterations required for convergence of results for the first operating point is presented and compared to equivalent results obtained by the segregated solver.
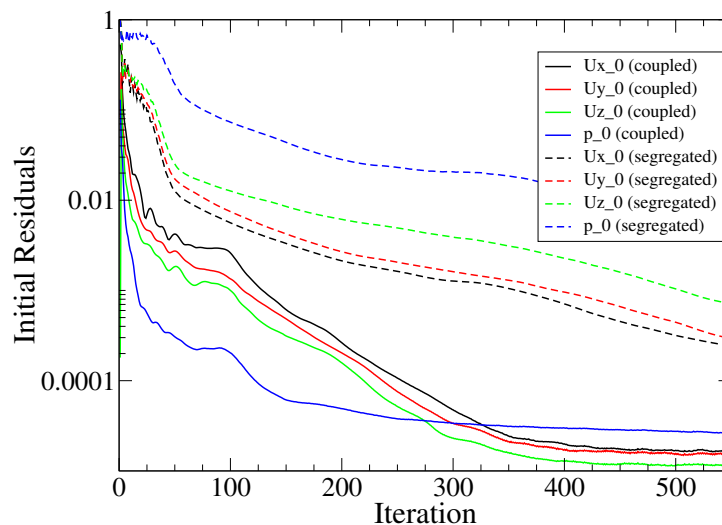
Figure 56: Comparison of initial residuals of segregated and coupled solver.

Figure 56 shows residual graphs for pressure and velocity fields for both segregated and coupled solvers. It can be seen that the fields obtained by coupled solver converge significantly faster than ones obtained by segregated solver. Pressure field, causing the biggest convergence problems in the segregated solver, converges the fastest in coupled solver. In 100th iterations, residual of pressure drops under 10^{-4}. To obtain such value of initial residual in the segregated solver, 1600 iterations are required. Although the convergence of pressure is improved the most according to the figure, other fields also converge significantly faster.

Figure 57 shows convergence of turbulence parameters. It can be seen that the turbulence parameters, with the coupled k and ω, converge faster than with segregated solver.
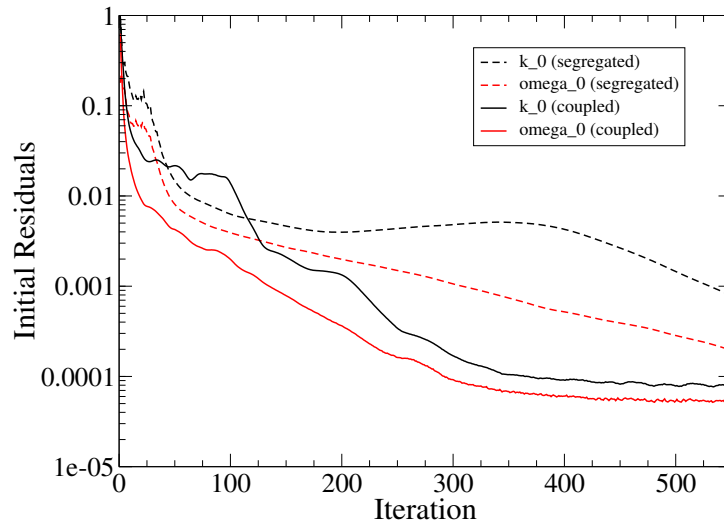
Figure 57: Comparison of turbulence parameters initial residuals of segregated and coupled solver.

Results for operating point with maximum efficiency

With faster convergence of the presented fields, head, power and efficiency also converge faster. Figure 58 shows comparison between convergence of head obtained by coupled and segregated solver. Figure 59 shows the power, while Figure 60 shows convergence of efficiency. From the figures, it can be seen that the convergence is faster for the parameters obtained with coupled solver.
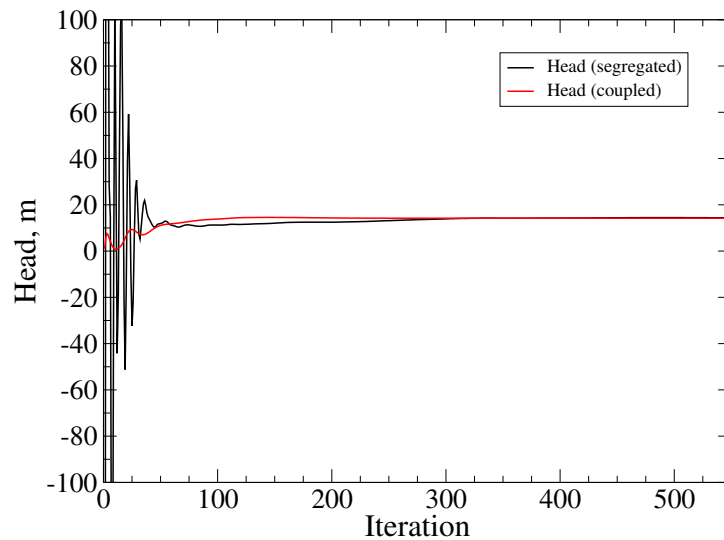
Figure 58: Comparison of head convergence between coupled and segregated solver.
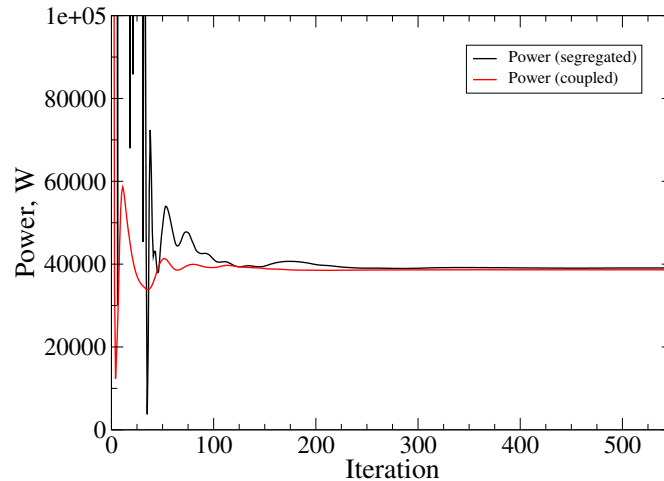
Figure 59: Comparison of power convergence between coupled and segregated solver.
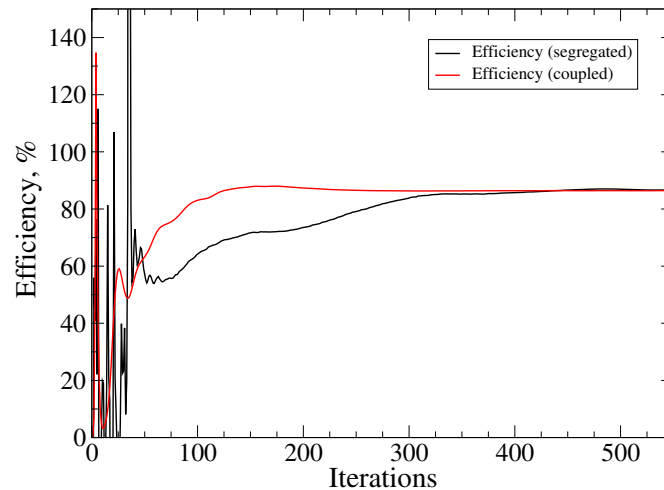
Figure 60: Comparison of efficiency convergence between coupled and segregated solver.

5.2.5   Comparison Between Non-consistent and Consistent Transient Solver

In the following figures head, power and efficiency graphs as a function of time for the first operating point are shown. Start time of the simulation is not zero, but the last time step from the simulation with consistent solver which is presented in section 5.2.1. Hence, initial conditions for all the parameters are the values from the last time step from consistent solver. In subfigures of Figure 61, oscillations of the measured items can be seen, indicating that the consistent solver converges smoother than the non-consistent solver. Consistent solver is also robust enabling the user to run simulations with greater time step. To show the behaviour of the non-consistent solver, simulation was performed with the time-step set 5 times lower than in simulation with consistent solver, yielding Courant number smaller than 1. Obtained values of the head, power and efficiency are not representative due to small period of time simulated.
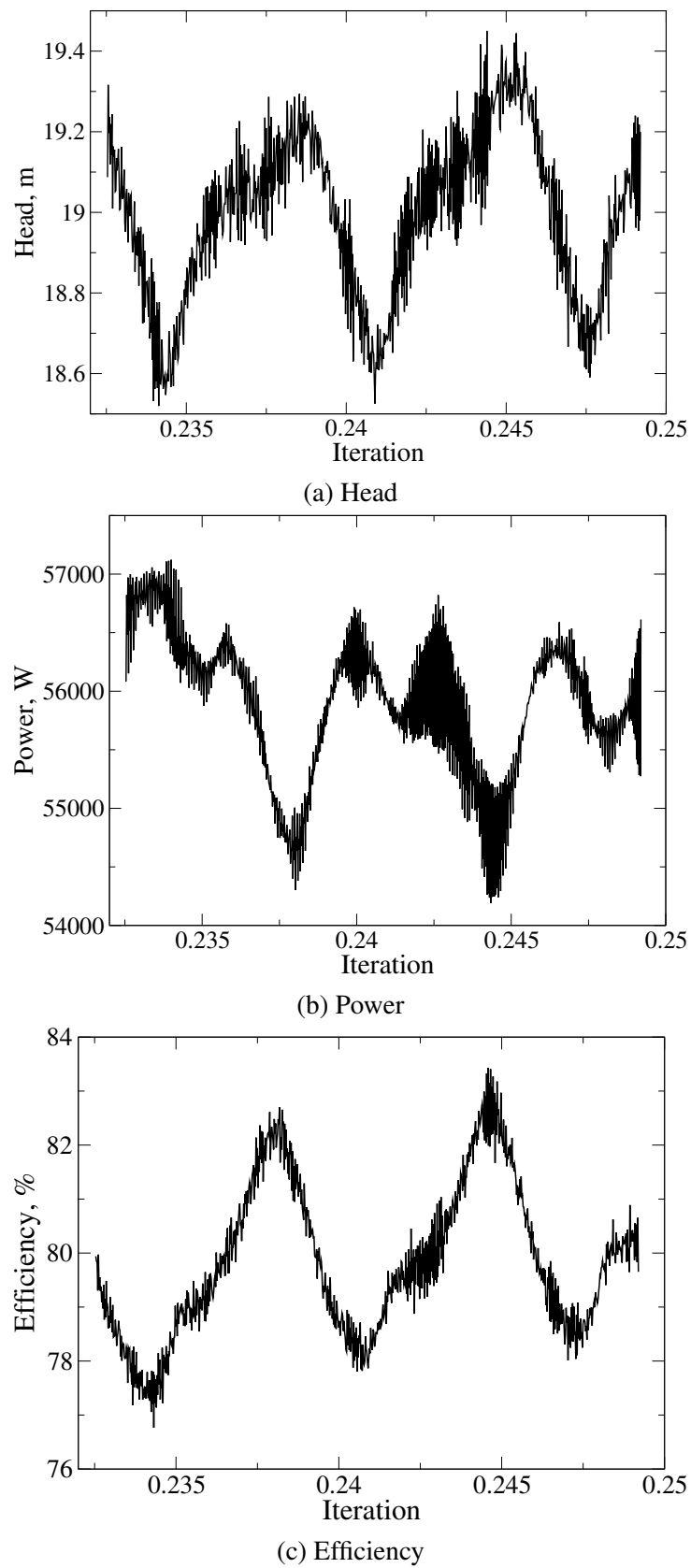
(a) Head

(b) Power

(c) Efficiency

Figure 61: Graphs obtained with non-consistent solver.

5.2.6   Time comparison

Table 4 shows the information concerning required time to perform the simulation. Given time for transient simulation represents the time required to simulate one revolution of the rotor, equivalent to 0.046 s.

Table 4: Time comparison.

Simulation	Iterations	CPU	Initial residuals	Simulation time, min
Transient	1 rev	i7, 3.7 GHz, 4 cores	10^{-4}	407
MRF (GGI)	1600	i7, 3.7 GHz, 4 cores	10^{-5}	995
MRF (mixing plane)	3400	i7, 3.7 GHz, 1 core	10^{-4}	5293
MRF (coupled)	300	i7, 3.7 GHz, 4 cores	10^{-5}	187
MRF (coupled + new GGI)	200	E7, 3.5 GHz, 56 cores	10^{-5}	75

New GGI mentioned in the table will be implemented in the new version of foam-extend. Convergence graphs of the head, power and efficiency obtained with the simulation with new GGI are shown in the subfigures of Figure 62.
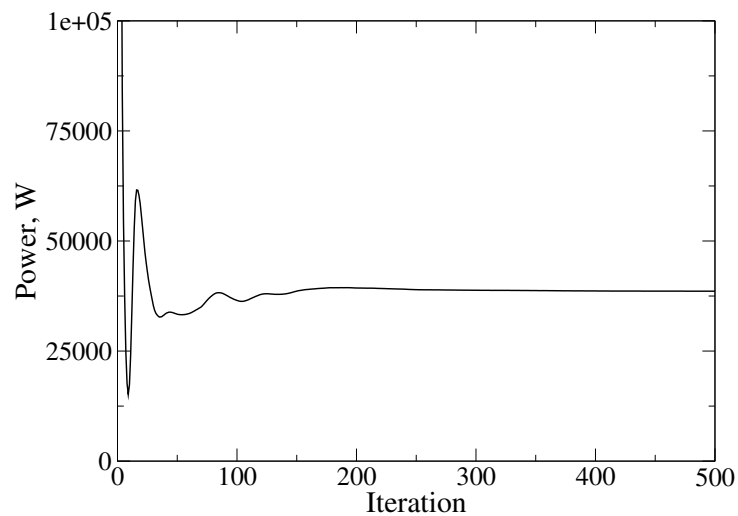
(a) Power
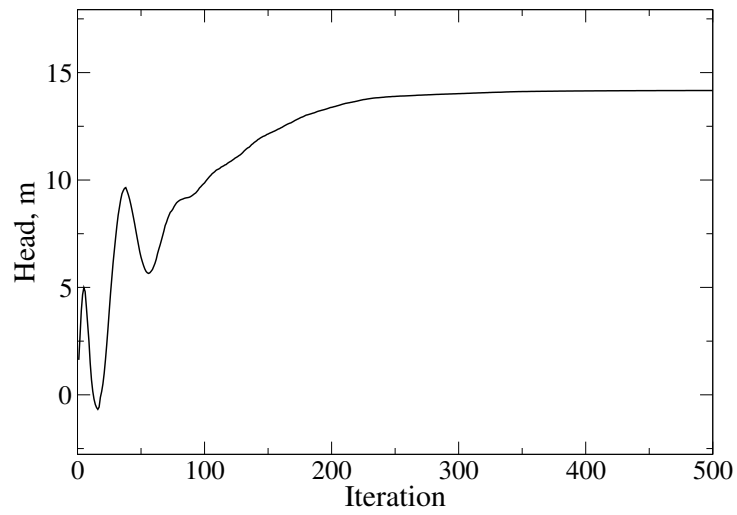
(b) Head
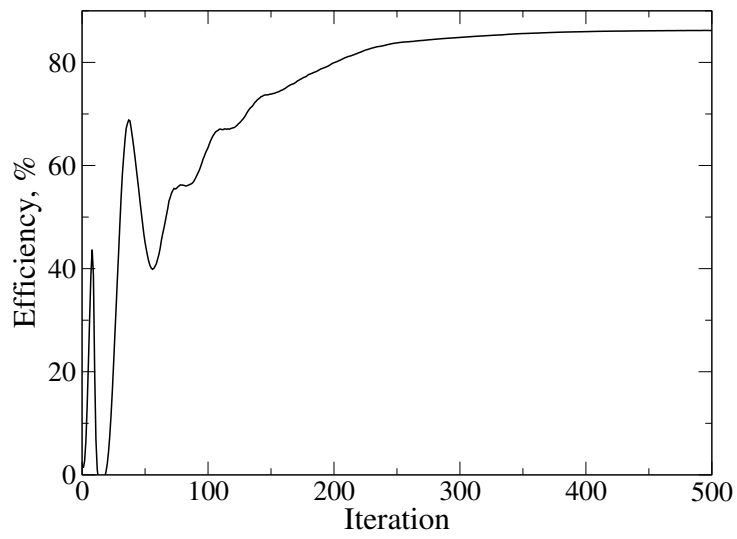
(c) Efficiency

Figure 62: Power, head and efficiency graphs with the new GGI.

5.2.7   Accuracy of Results

Results for first operating point are compared relative to the referent results obtained with the transient simulation. Table 5 shows results of head, efficiency and power for all the simulations. Relative errors represented in the table are calculated with respect to the transient simulation. As mentioned before, greatest error in results occurs in the MRF simulation with the mixing plane interface. All the simulations with the GGI show similar error but theoretically they should all converge to the same solution due to the same mathematical model.

Table 5: Result comparison for the OTA-1 pump.

Simulation	Head, m	H_{Err} , %	η , %	η_{Err} , %	Power, W	P_{Err} , %
Transient	15.0	-	85	-	41,600	-
MRF (GGI)	14.47	3.53	87.1	-2.47	39,013.9	6.2
MRF (mixing plane)	11.92	20.53	59.7	29.76	46,918.1	-12.78
MRF (coupled)	14.21	5.26	86.4	1.65	38,632.5	7.13
MRF (coupled + new GGI	14.16	5.6	86.2	1.41	38,600	7.21

5.3   Closure

This section presents results obtained with different numerical methods for the simulation of the OTA-1 pump. Transient simulation is assumed to be the most accurate, while other results are assessed relatively to the transient simulation results. It is shown that mixing plane cannot be used in turbomachinery simulations where the effects of the wakes behind the rotor blades are important. Simulations with GGI provide reasonable results and therefore, they are used to generate $Q - H$ and $Q - \eta$ curves. CPU times required for the simulation using different methods are also compared. It can be concluded that the usage of new solvers and numerical methods can provide the simulation results in significantly reduced CPU time.

5.4 OTA-2 Pump

For the simulation purposes of the OTA-2 pump two meshes are used. Mesh presented in the section 4 is used in all simulations except for the MRF simulation with the GGI. The initial mesh consists of too many cells what would require a few months of CPU time for transient simulation with the available computational resources.

5.4.1 Transient Simulation

Transient simulation of the OTA-2 pump is assumed to be the most accurate simulation of the pump and is used as a reference in the comparison of the results. Case set up is similar to one presented for the OTA-1 pump with the difference in values of initial and boundary conditions. Inlet values of boundary conditions are different for different operating points. Table 6 shows types of boundary conditions for the patches that define geometry.

Table 6: Velocity and pressure boundary conditions for the OTA-2 pump.

Patch	Velocity boundary condition	Pressure boundary condition
inlet	fixedValue; uniform (U_x 0 0);	zeroGradient;
outlet	zeroGradient;	fixedValue; uniform 0;
rotorBlades	movingWallVelocity; uniform (0 0 0);	zeroGradient;
rotorCasing	movingWallVelocity; uniform (0 0 0);	zeroGradient;
statorBlades	movingWallVelocity; uniform (0 0 0);	zeroGradient;
inletCasing	fixedValue; uniform (0 0 0);	zeroGradient;
outletCasing	fixedValue; uniform (0 0 0);	zeroGradient;
rotor-stator interfaces	ggi;	ggi;

Each operating point is defined by corresponding volumetric flux, from which the inlet velocity is calculated:

- inlet velocity U_x for first operating point equals 0.933 $\frac{\text{m}}{\text{s}}$ for the volumetric flux 0.95 $\frac{\text{m}^3}{\text{min}}$,

- for second operating point U_x equals 0.786 $\frac{\text{m}}{\text{s}}$ for the volumetric flux 0.8 $\frac{\text{m}^3}{\text{min}}$ and

- for third operating point U_x equals 1.228 $\frac{\text{m}}{\text{s}}$ for the volumetric flux 1.25 $\frac{\text{m}^3}{\text{min}}$.

Initial conditions for velocity and pressure are calculated using potential flow, while the initial conditions for turbulence parameters are calculated in the same way as for the OTA-1 pump.

Rotor-stator interface used in this simulation is GGI in order to couple non-conformal rotor and stator cell zone when rotor cell zone is rotating.

Results

Results of transient simulation consist of two parts:

1. time-averaged field of pressure, velocity and turbulence parameters.

2. performance curves of head, power and efficiency as a function of time.

Transient simulation is performed for three operating points which are defined with the volumetric flux. Convergence of the simulations is monitored using the head, power and efficiency graphs and results have converged when the values become quasi-stationary.

Time-averaged flow fields and turbulence parameters

Velocity field in upper stator section is shown in Figure 63. It can be seen that the velocity increases as the fluid approaches the rotor inlet due to decreasing of geometry cross-section. Flow across the stator blades is similar to flow around an airfoil. On the suction side of the blade, velocity is higher and vice versa. For the operating point with highest efficiency the stator blades are guiding the flow smoothly on the rotor blades in order to ensure the highest possible efficiency. Figure 63 also shows velocity field with the detail of the flow around the stator blades and the entrance of the rotor. Vectors indicate how the stator blades are guiding the flow and that the flow at the end of the stator blades has swirling component. In the first detail of the figure, velocity vectors around the stator blades are shown, while the closer look at the spiral flow is given in the second detail.
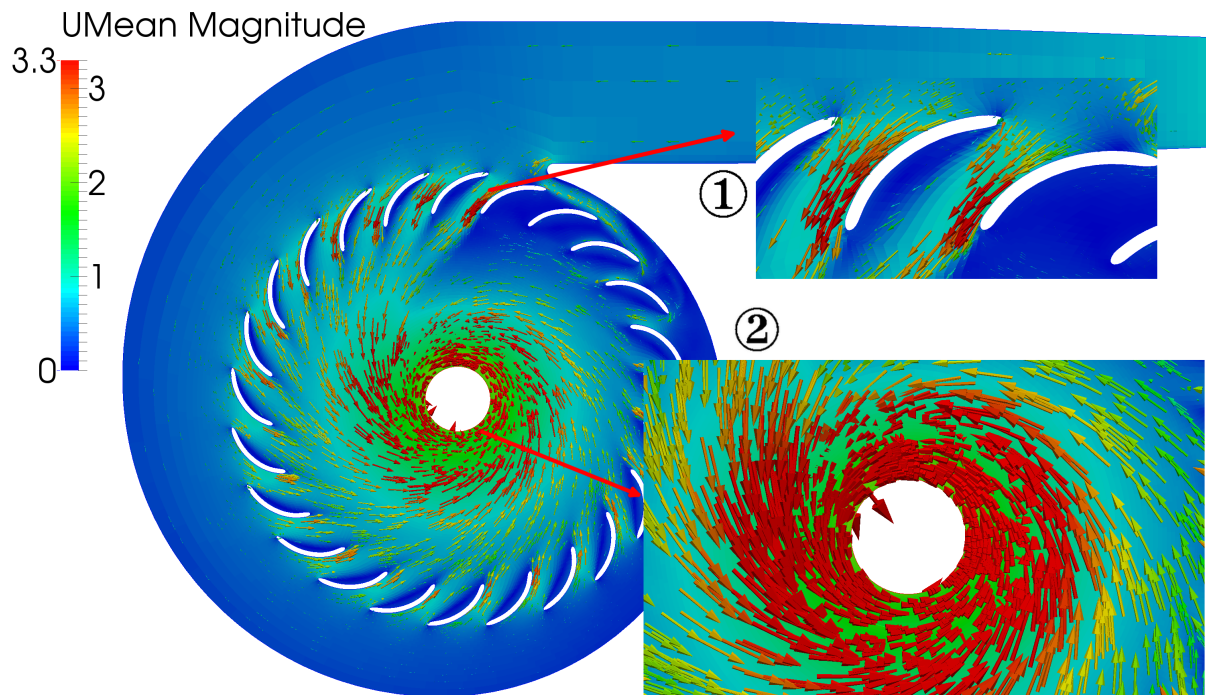
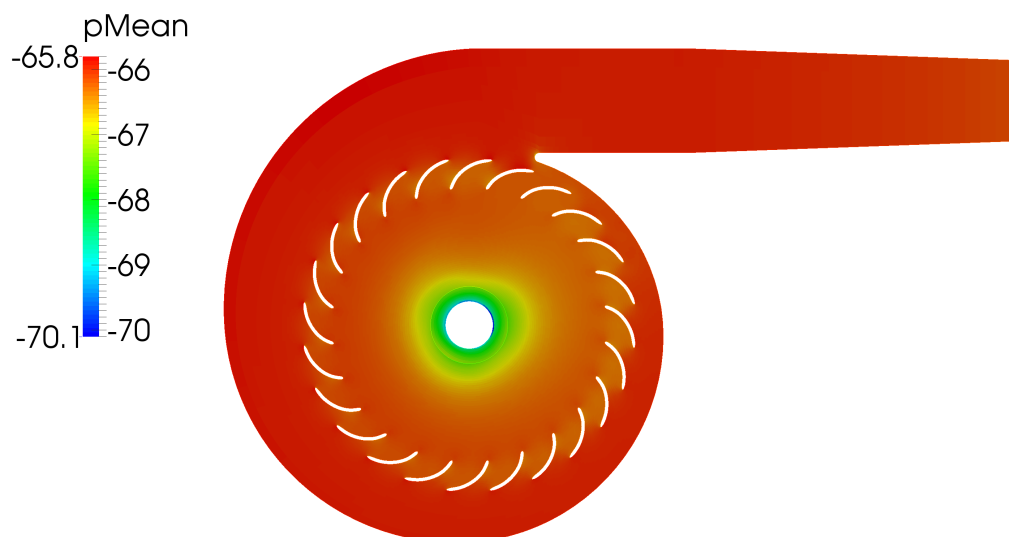Figure 63: Time-averaged velocity vectors in stator of the OTA-2 pump.

Figure 64: Time-averaged pressure field in stator of the OTA-2 pump.

Figure 64 shows a distribution of pressure in the stator. The drop of pressure in the stator casing is the result of increase of the fluid velocity and the friction that occurs.

In the Figure 65 turbulent kinetic energy distribution over the stator blades and the casing is shown. It can be seen that the intensity of turbulence is higher in the area around the suction side of the blades. Higher field of turbulent kinetic energy can indicate the area in which recirculation occurs what can be seen in the detail of the figure. The figure also shows that the turbulence is increased in the wakes of the stator blades.
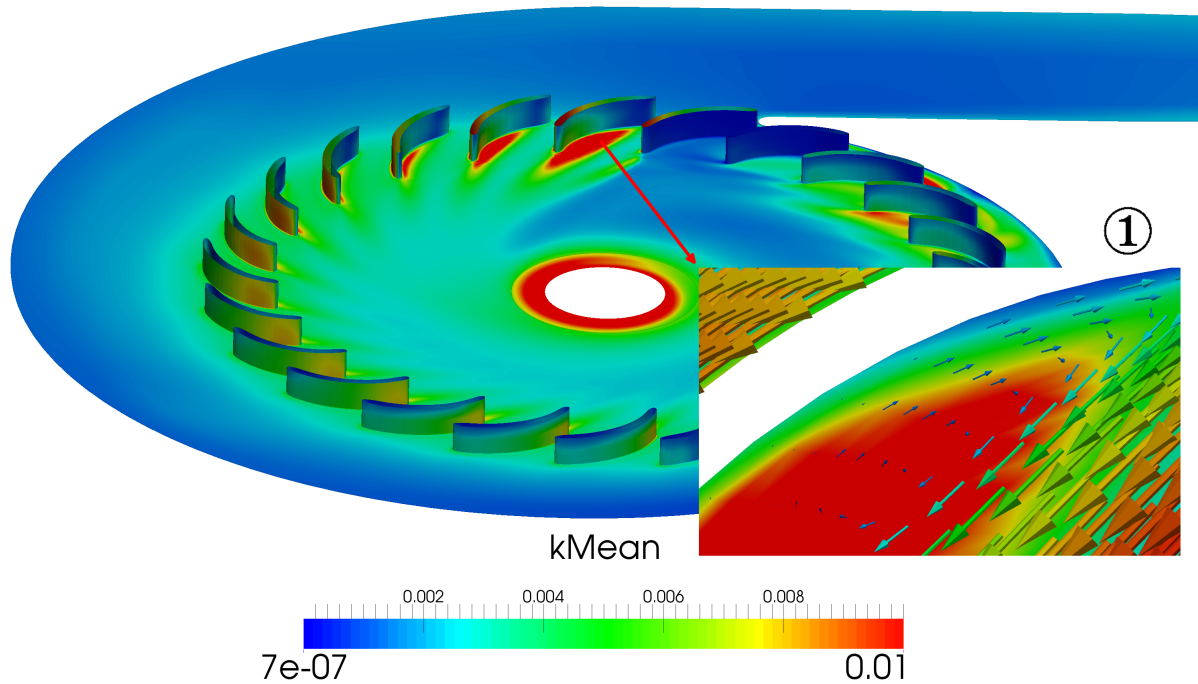
Figure 65: Time-averaged turbulent kinetic energy field in stator of the OTA-2 pump.

At the end of the stator cell zone rotor-stator interface is positioned through which flow enters the rotor. The way the transition happens is shown in the Figure 66. Transition is shown in the cross-section of the pump parallel to the axis of the rotation with the details of the flow around the inlet interface and the outlet casing. It can be seen that the velocity has its maximum at the exit of the rotor and that it decreases away from the rotor.
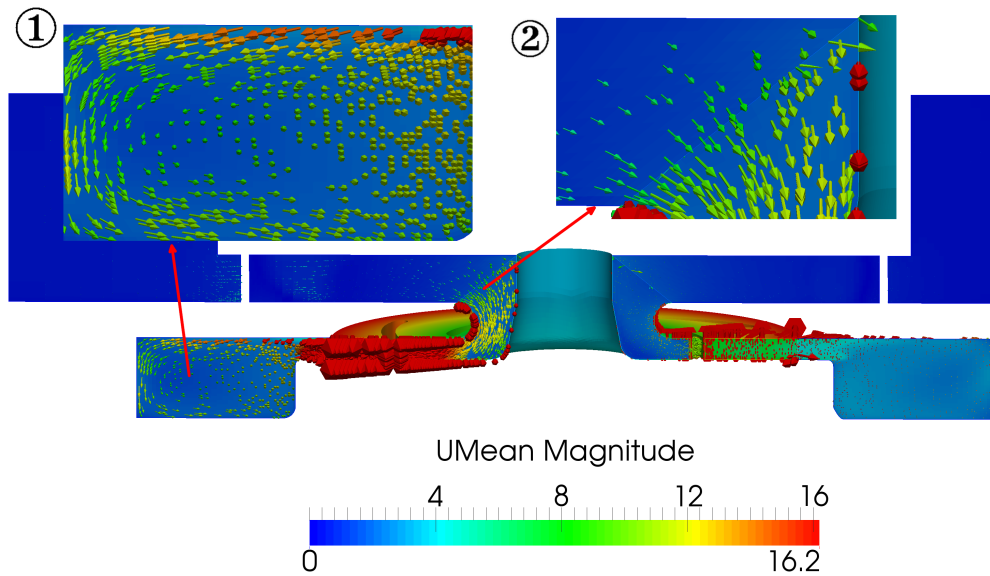
Figure 66: Transition of the flow between the zones of the OTA-2 pump.

Most important part of the pump operation is the behaviour of the flow in the rotor and it has to be operated in the nominal operating point in order to achieve highest efficiency. Every other operating point will result in the decrease of the efficiency. Figure 67 shows a distribution of velocity field around the rotor blades and in the outlet casing. First detail of the figure gives a closer look at the velocity distribution around the trailing edge, while the second shows a velocity distribution around the leading edge.
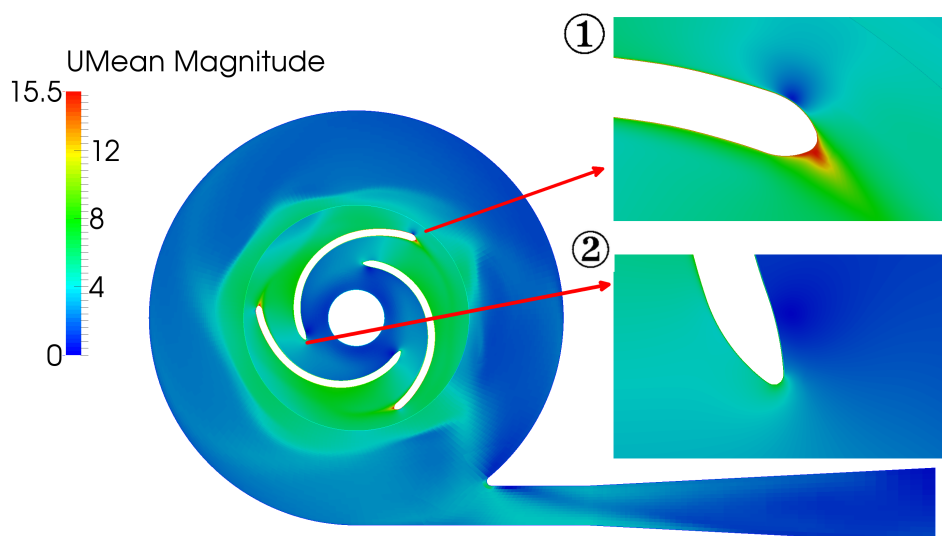
Figure 67: Time-averaged velocity field distribution in rotor of the OTA-2 pump.

Pressure field around the rotor blades is shown in figure 68 with the details of pressure around the leading, detail 2, and the trailing edge of the blade, detail 1. Jump in the value of fields shown in the Figure 67 and 68 is due to numerical error introduced by rotor-stator interface and due to the time-averaging of the results. Distribution of the pressure over the rotor blades and rotor casing is shown in the Figure 69.
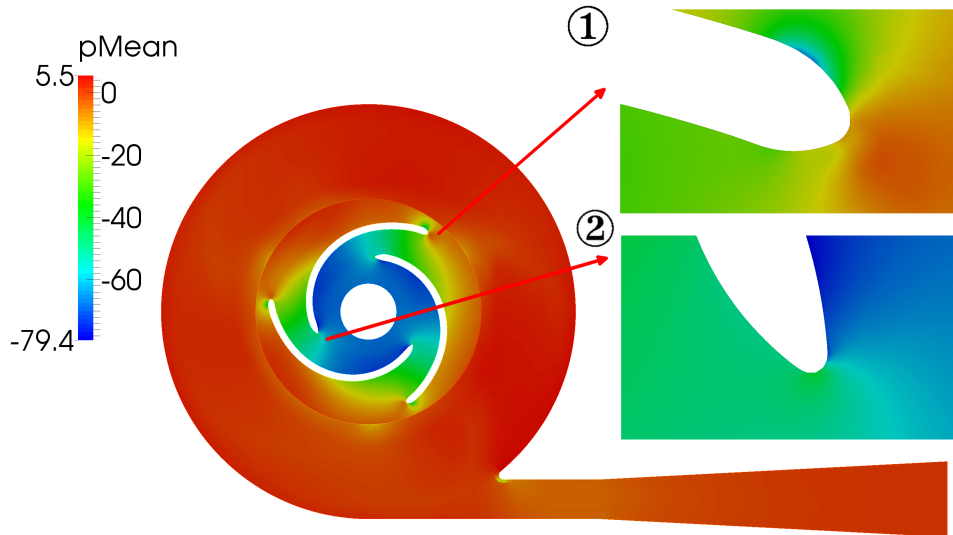
Figure 68: Time-averaged pressure field distribution in rotor of the OTA-2 pump
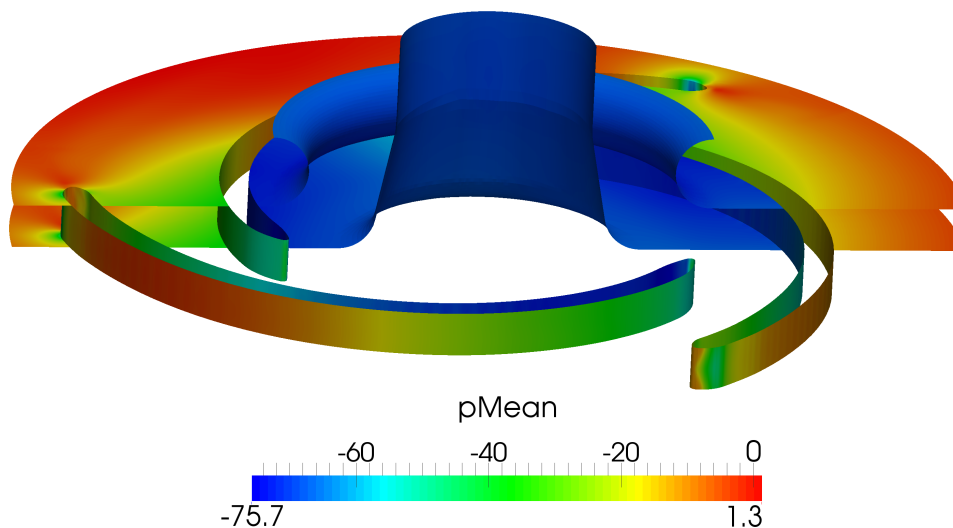
Figure 69: Time-averaged pressure field distribution over the rotor of the OTA-2 pump

Power curves for different operating points

Performance curves presenting power, head and efficiency are obtained using a function object called turboPerformance for three operating points in the same way as for the OTA-1 pump. Figure 70 shows graph of pump power as a function of time for first operating point defined by volumetric flux of 0.95 m^3/s. For this operating point efficiency of pump is the highest. Upper subfigure shows a graph for whole simulated time. This graph gives an idea of result convergence. It can be seen that pump power repeats periodically in time what is one of the indicators that simulation results have converged. In a lower subfigure an end detail of a pump power is shown, in which oscillation for one revolution of rotor can be seen. Required time for one revolution of rotor equals 0.075 s.
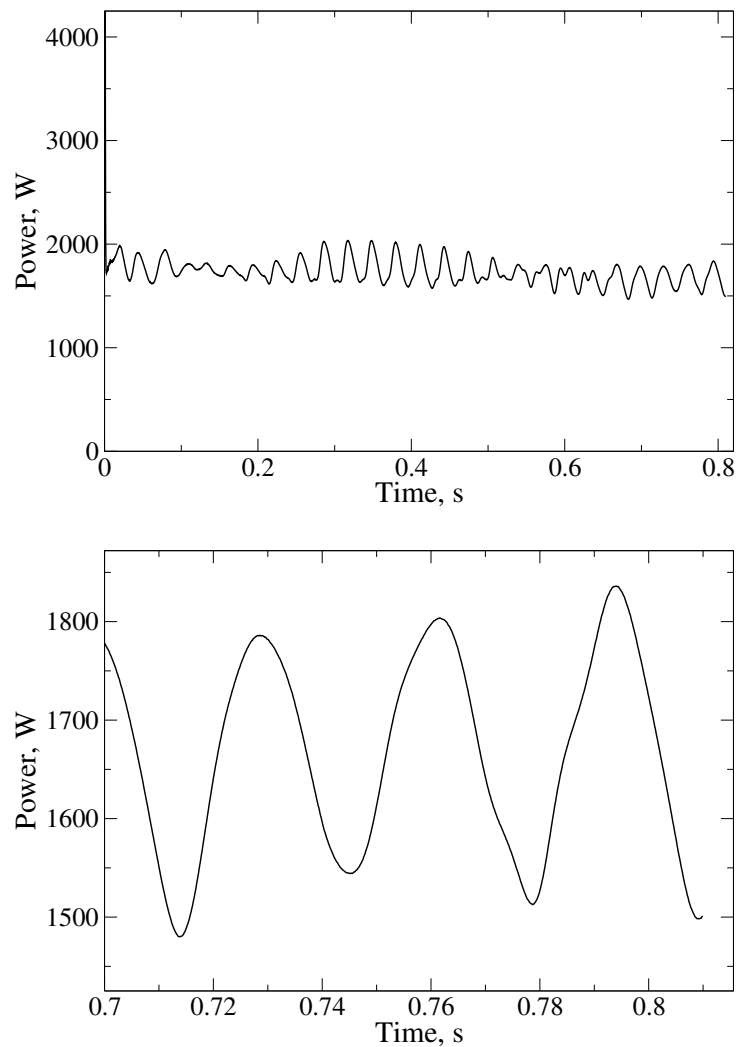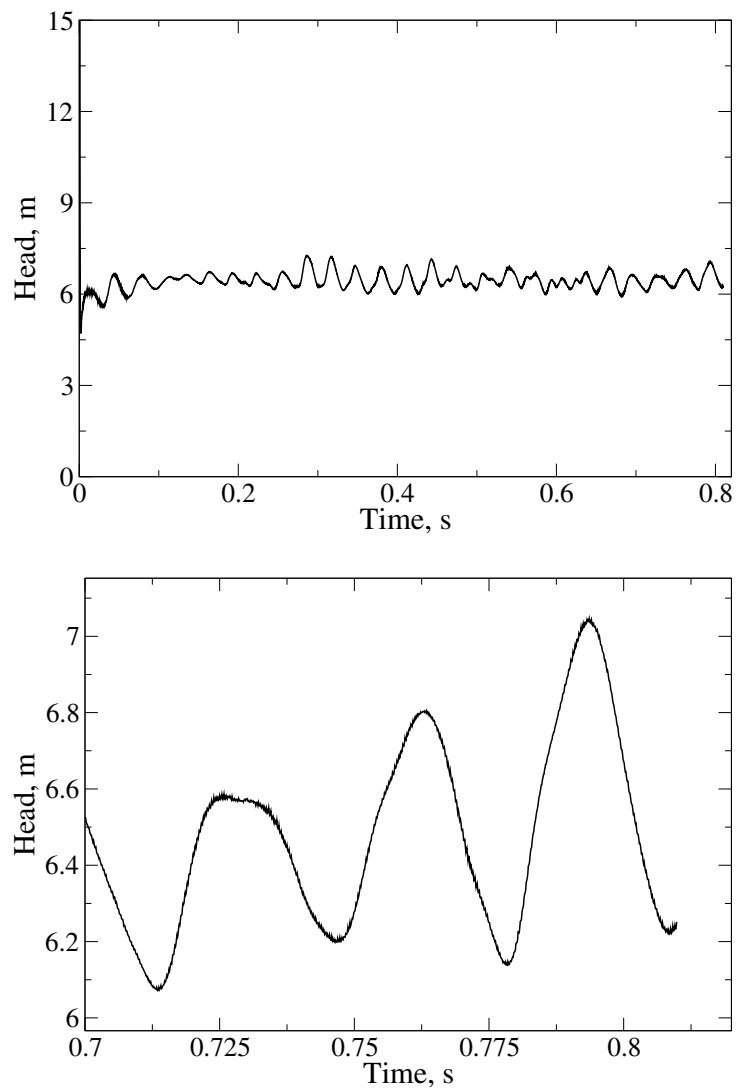

Figure 70: Power as a function of time for the first operating point of the OTA-2 pump.

Second operating point is defined by a lower volumetric flux which equals 0.8 m^3/s. Moving away from nominal operating point results in a lower efficiency. Figure 71 shows graph of a pump power for second operating point. First operating point is studied thoroughly, while the other operating points are studied to obtain $Q - H$, $Q - P$ and $Q - \eta$ curves and to present differences in a flow for nominal and partial load.
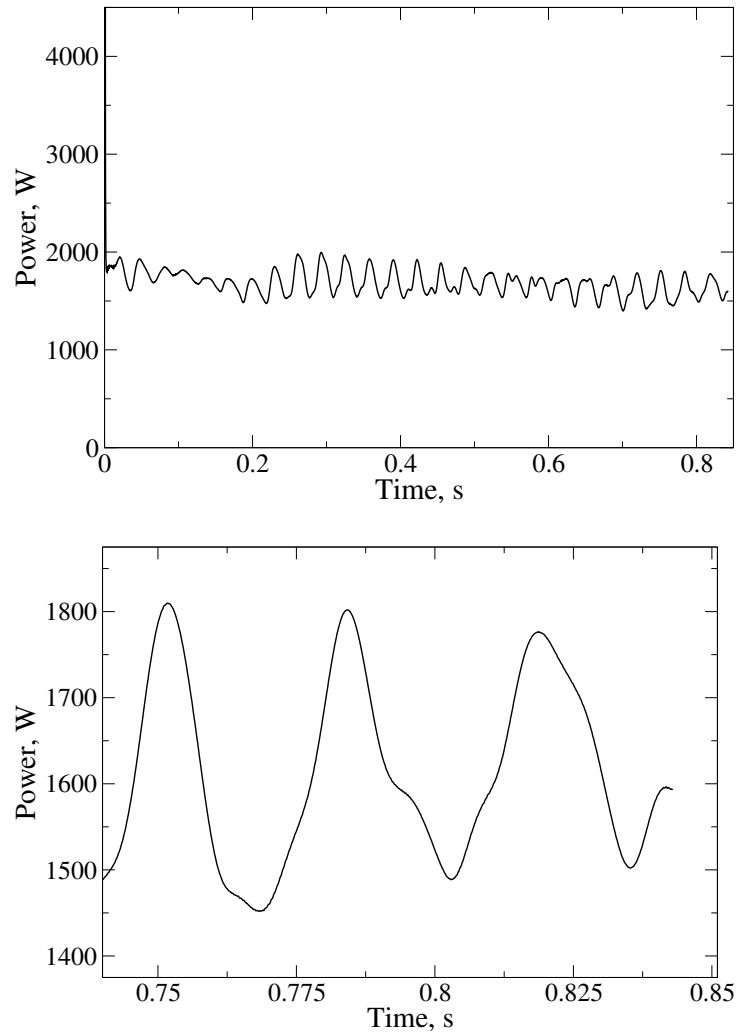
Figure 71: Power as a function of time for the second operating point of the OTA-2 pump.

Pump power for third operating point is shown in Figure 72. This operating point is defined with the volumetric flux that is greater than for the first operating point and equals 1.25 m^3/s. It can be seen from lower subfigure that the simulated period of time is greatest for the third operating point what resulted in a better convergence of the results

From the presented figures, it can be seen that the power of the pump oscillates around the value of 1600 W for different operating points.
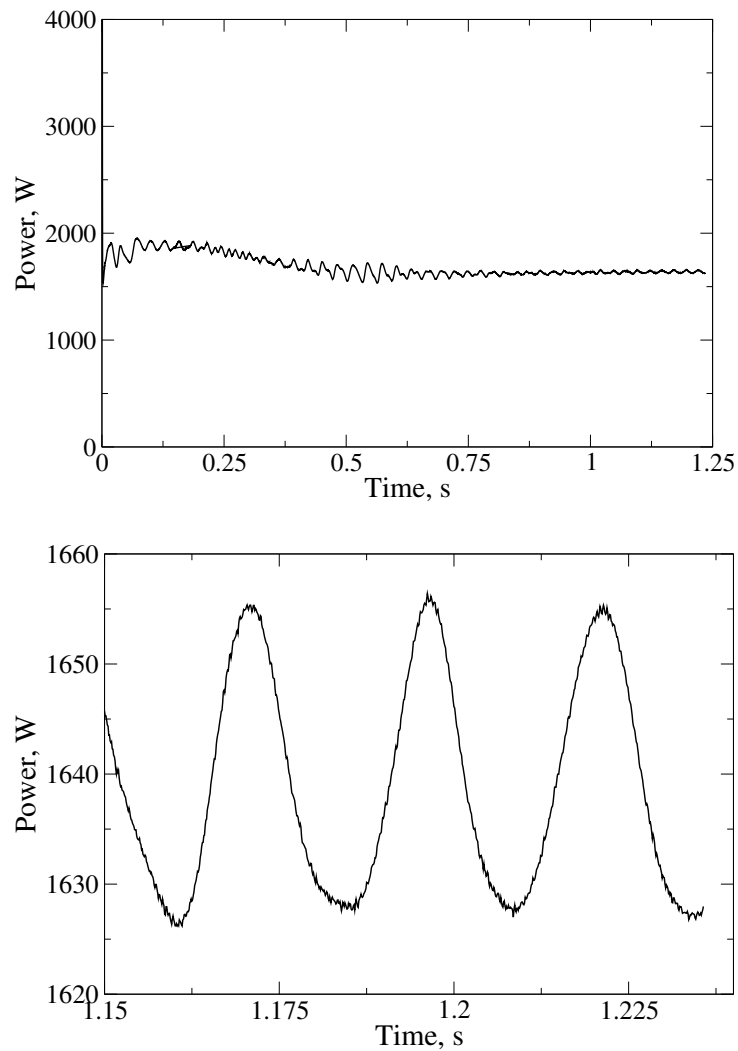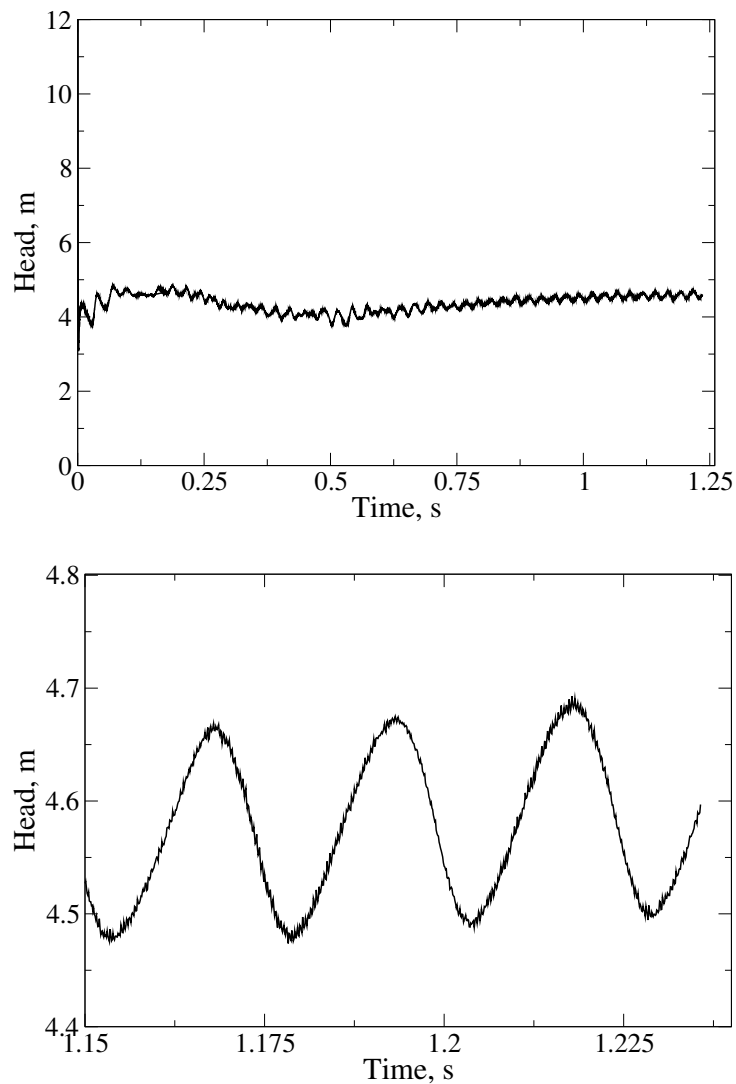

Figure 72: Power as a function of time for the third operating point of the OTA-2 pump.

Head curves for different operating points

Figure 73 shows a pump head as a function of time for the first operating point which is defined by volumetric flux of 0.95 m^3/s. Upper subfigure shows a change of head for the whole simulated time interval, while the lower subfigure shows the oscillations for one revolution of rotor. Average head for first operating point equals 6.5 m.

Figure 73: Head as a function of time for the first operating point of the OTA-2 pump.

Second operating point is defined by a lower volumetric flux with the value of 0.8 $\frac{m^3}{s}$ and therefore, pump head for this operating point is higher, as seen in Figure 74. According to lower subfigure, average head for second operating point equals 7.5 m.
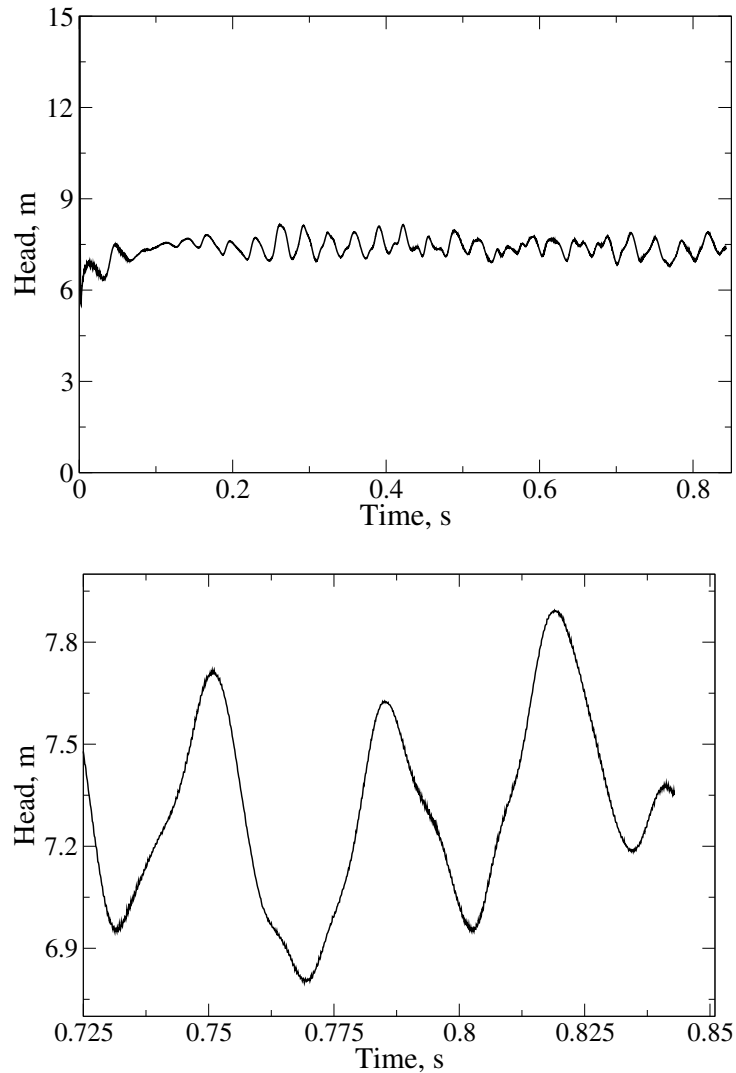
Figure 74: Head as a function of time for the second operating point of the OTA-2 pump.

Third operating point is defined with greater volumetric flux than the first operating point. Volumetric flux equals 1.25 m^3/s and therefore head is lower than nominal. Graph of head can be seen in Figure 75 and according to lower subfigure average head equals 4.6 m.

Figure 75: Head as a function of time for the third operating point of the OTA-2 pump.

Efficiency curves for different operating points

Figure 76 shows efficiency graphs as a function of time for the first operating point. Average efficiency, according to lower subfigure, equals 60%.
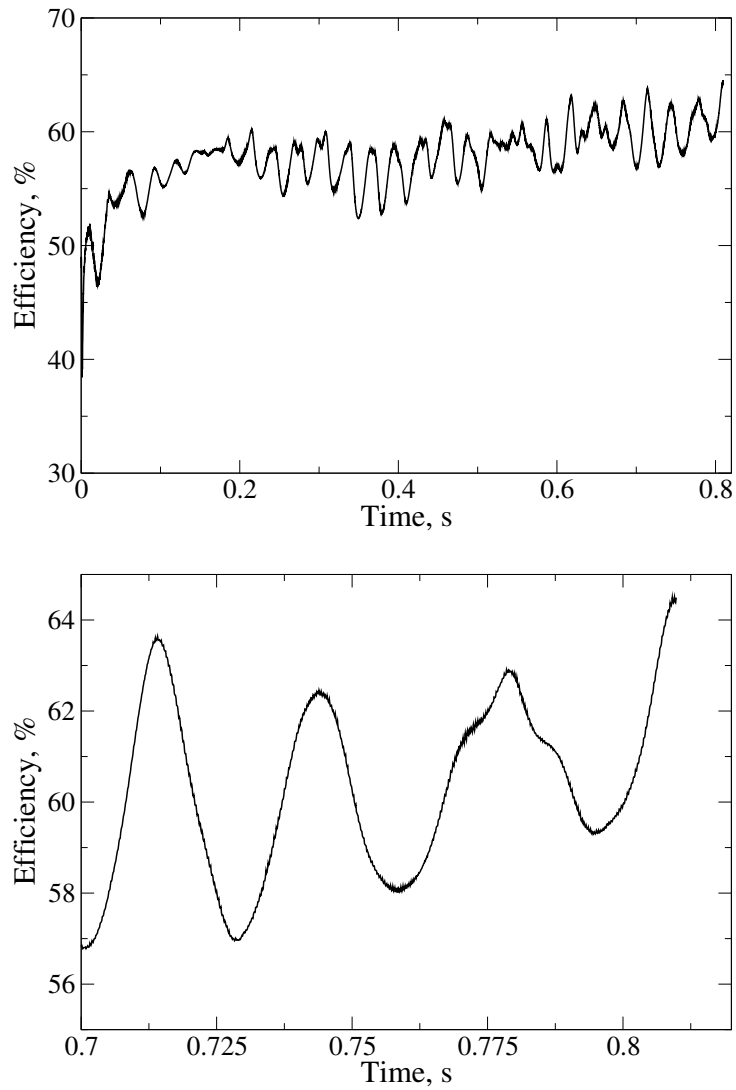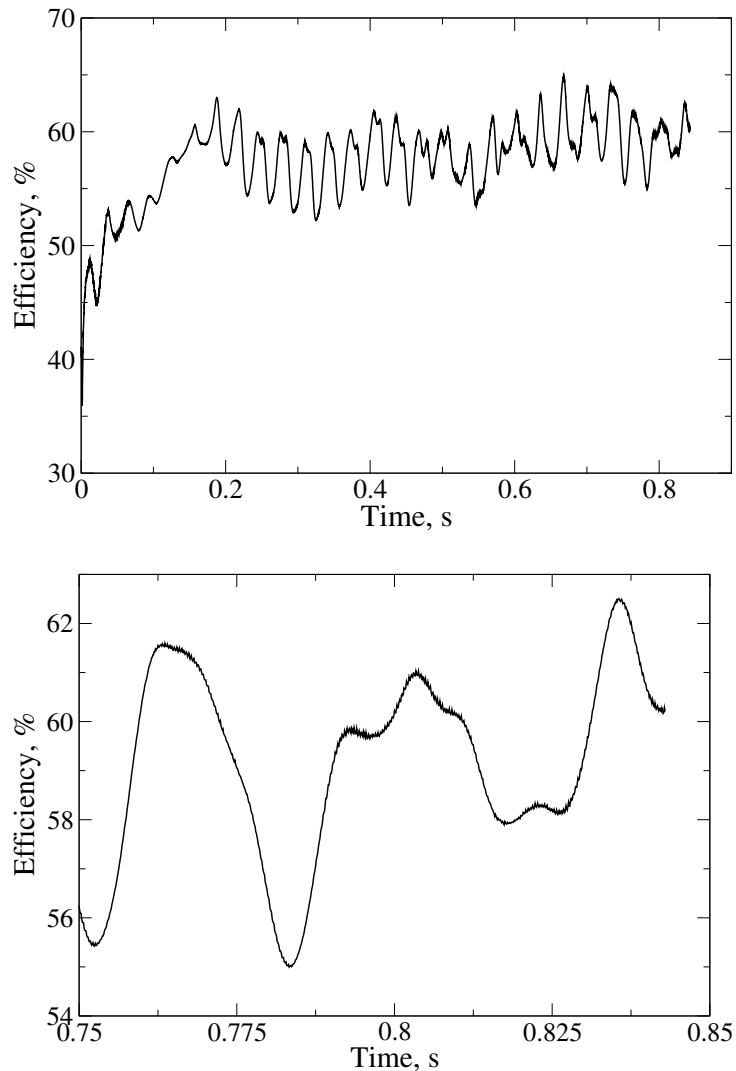

Figure 76: Efficiency as a function of time for the first operating point of the OTA-2 pump.

Second operating point is a partial load operating point and therefore efficiency is lower. Graphs of efficiency for second operating point are shown in Figure 77. According to graph shown in lower subfigure, average efficiency equals 59%. It can be seen that the drop in efficiency is not large when the volumetric flux is lowered from the nominal operating point.

Figure 77: Efficiency as a function of time for the second operating point of the OTA-2 pump.

Third operating point is also a partial load. Graphs of efficiency are shown in Figure 78 and according to lower subfigure average efficiency equals 57%.
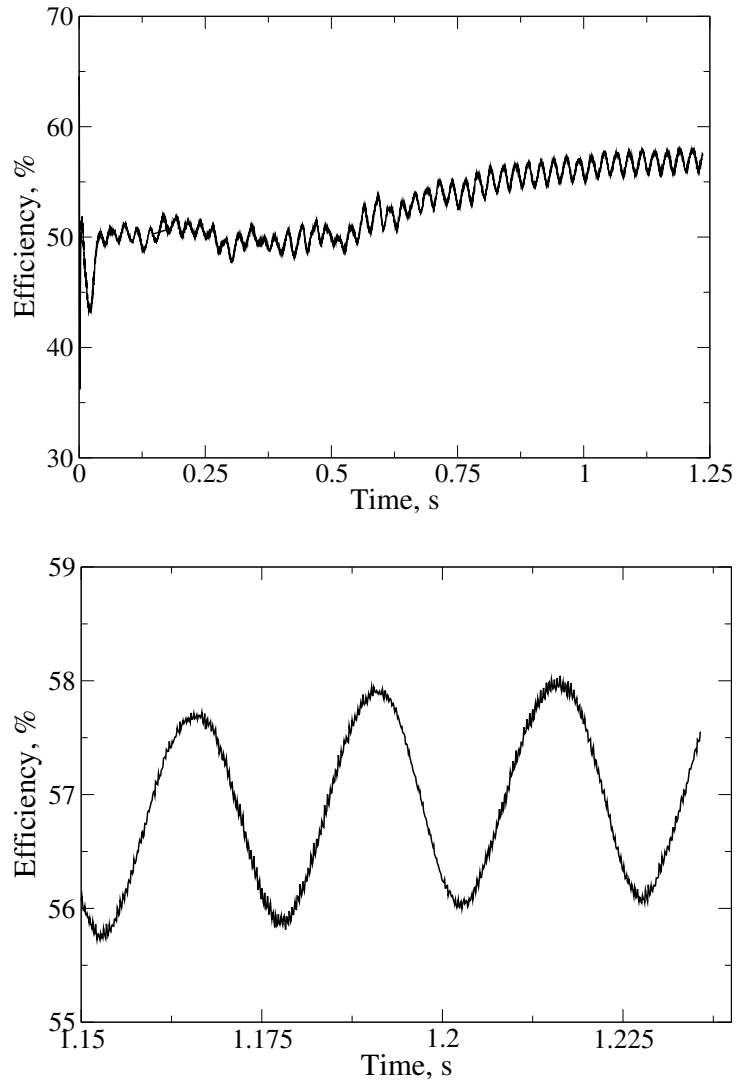
Figure 78: Efficiency as a function of time for the third operating point of the OTA-2 pump.

5.4.2 Multiple Reference Frame Simulation with General Grid Interface

This subsection deals with the MRF simulation of three operating points for the OTA-2 pump defined in the same way as for the transient simulation. Using the simulation results $Q - H$ and $Q - \eta$ curves are approximated.

To set up a case for MRF simulation, boundary and initial conditions are specified in the same way as for the transient simulation with the exception for the velocity boundary condition. MovingWallVelocity boundary condition is replaced with uniform value of (0 0 0). For the convergence criterion, pump power, head and efficiency are monitored as a function of iterations. End time of the simulation was declared when the oscillations of power, head and efficiency became lower than 1%.

Flow fields and turbulence parameters

All the simulated operating points presented in this subsection are the result of a simulation on a different mesh than presented in the section 4.3. The main difference is the number of cells. For the purposes of MRF simulation mesh consists of 14 million cells. This is due to the fact that the MRF simulation was performed before the mesh presented in the previous section was created. Another difference is that the inlet and outlet pipes have been modified. For MRF simulation cross-sections of pipes are circular. This was changed for other simulation due to complicated topology of mesh when the transition is made to rectangular cross-section of the stator casing. Mentioned differences between the meshes significantly increas the CPU time required to perform the MRF simulation and therefore can not be compared with the required CPU time for other simulations.
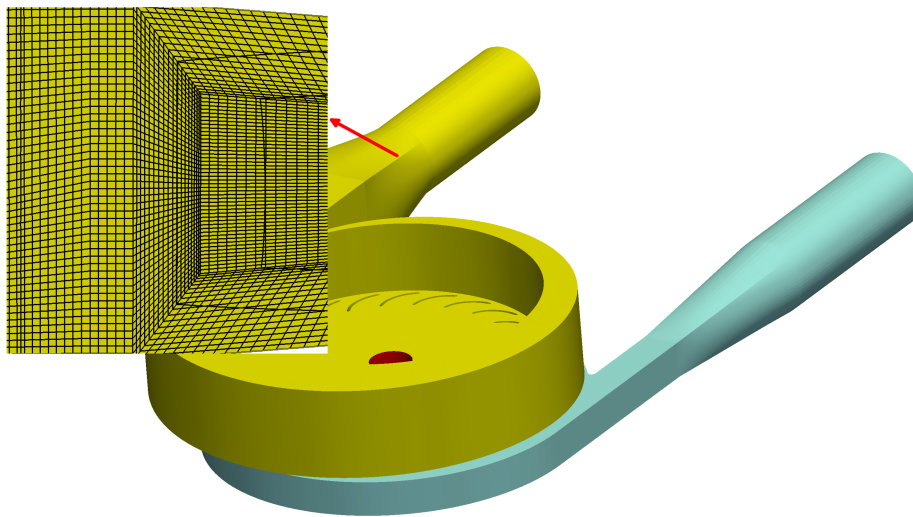
(a) 14 million cells
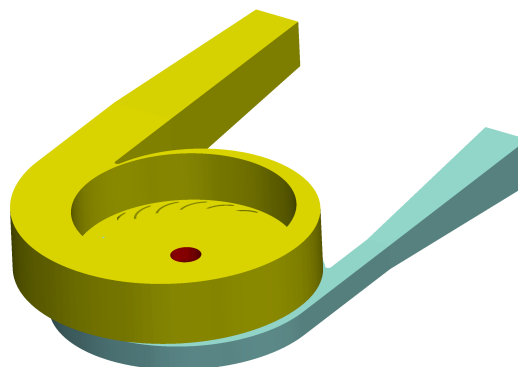
(b) 4 million cells

Figure 79: Comparison of the OTA-2 meshes.

Figure 79 shows both numerical meshes used in this thesis. In the first subfigure the mesh used only for MRF simulation is presented. Detail of the first subfigure shows a mesh cross-section parallel to the axis of rotation where the complicated transition in the mesh topology can be seen.

Figure 80 shows a velocity distribution in the stator casing. It can be seen that the flow composition is spiral after the stator guiding blades. It can also be seen that the velocity distribution obtained by the MRF simulation is almost the same as one obtained by the transient simulation. The detail of the figure gives a closer look at the flow around the stator blades. Higher resolution of the mesh also allows better resolving of the phenomena in the boundary layer of the stator casing. This can be noticed if the field around the wall of the stator casing for the MRF and transient simulations are compared. Vectors of velocity at the entrance of the rotor, coloured red, can not be seen completely because they are oriented in the direction of rotation axis (into the paper).
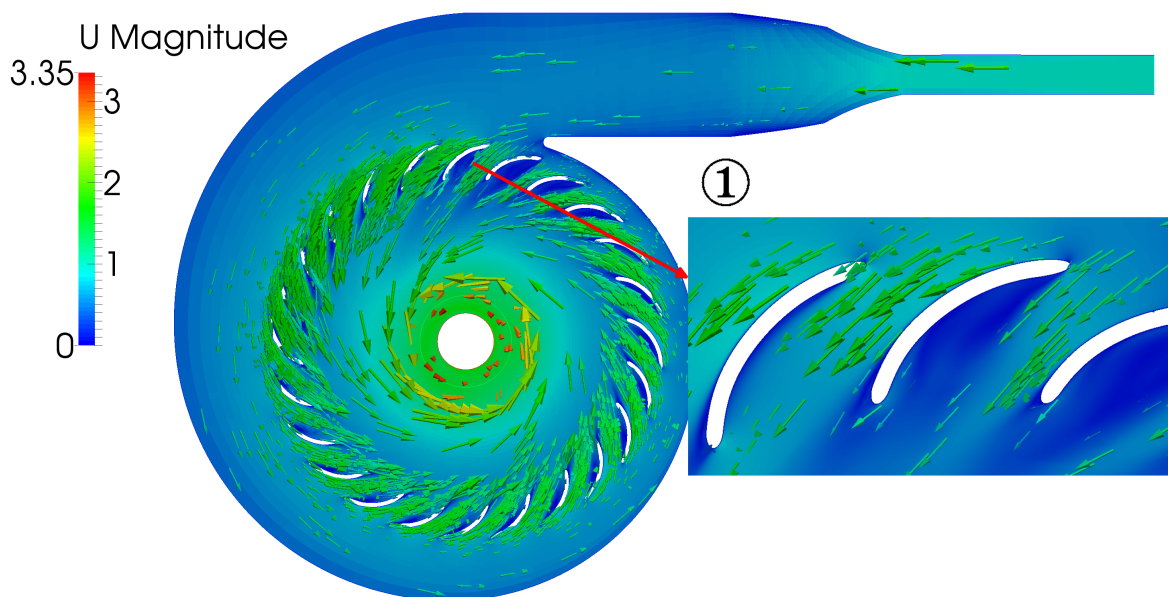

Figure 80: Velocity field in the stator casing of the OTA-2 pump obtained by MRF simulation.

Pressure field distribution in the stator casing is shown in the Figure 81. It can be seen that the results obtained by MRF approximate the transient simulation well. Even though inlet pipe geometry was modified and MRF simulation is steady-state, pressure drop in the stator is similar to the one obtained by transient simulation.
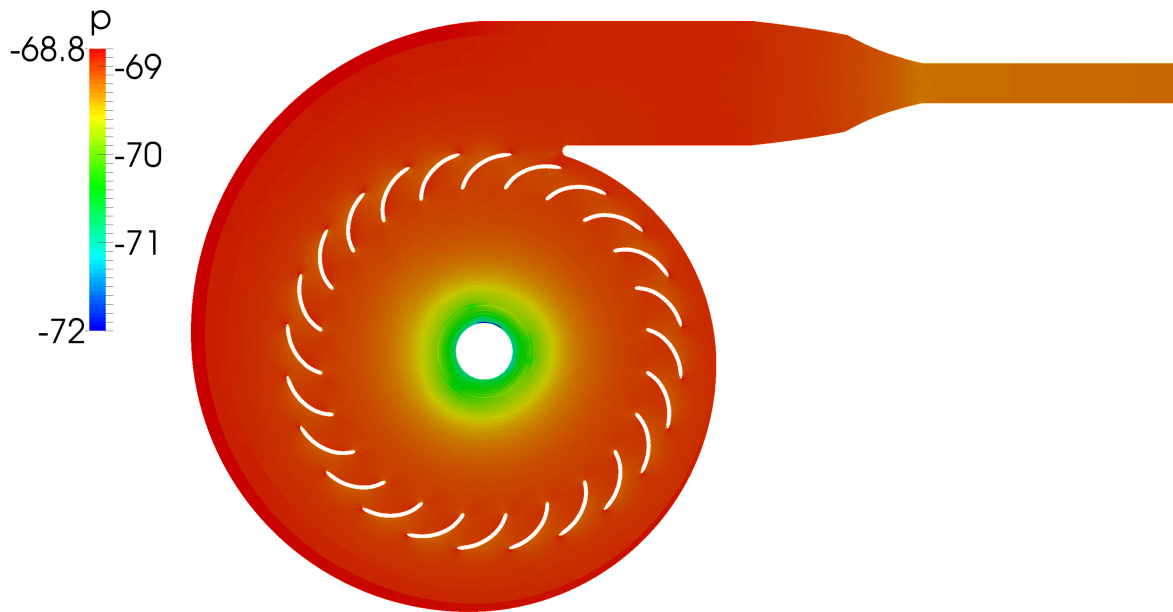
Figure 81: Pressure field in the stator casing of the OTA-2 pump obtained by MRF simulation.

Transition between stator and rotor cell zone is carried out with the aid of rotor-stator interface. Figure 82 shows the flow entering and leaving the rotor, where the detail 1 shows the entering and the detail 2 shows the distribution of the flow in the outlet pipe in the proximity of the rotor. Highest values of the velocity occur in the rotor, especially in the area near the wall of the rotor casing and blades.
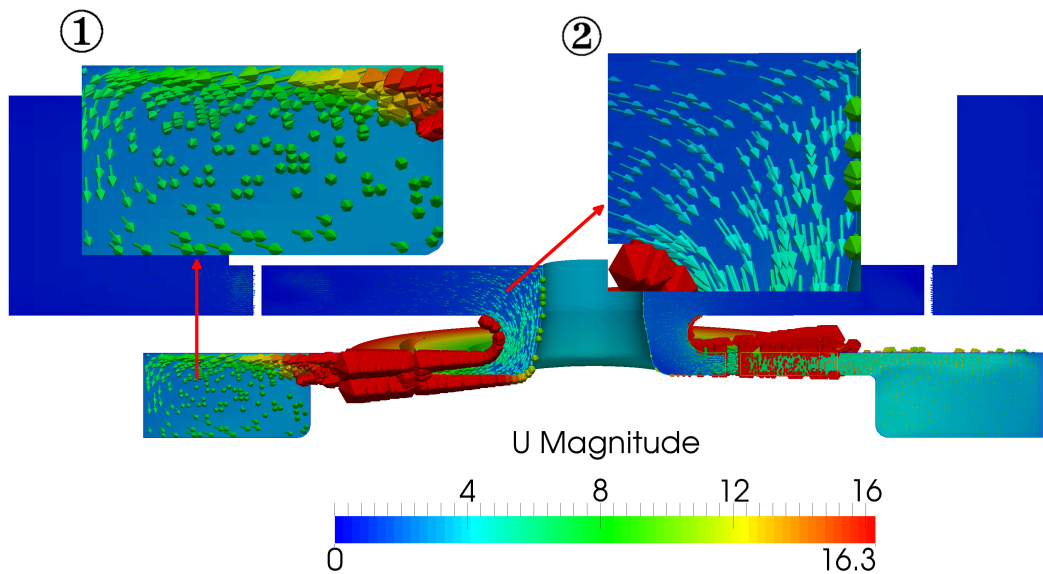
Figure 82: Transition of the flow between the rotor and stator cell zone.

Distribution of the velocity around the rotor blades is shown in the Figure 82, while the Figure 83 shows the pressure distribution. This is shown on the cross-section that is perpendicular to the cross-section shown in the Figure 81. Detail 1 of both figures shows the field distribution around the trailing edge of the blade, while the detail 2 shows the field distribution around the leading edge of the blade. Pressure distribution on the rotor casing and blades is shown in the Figure 85.
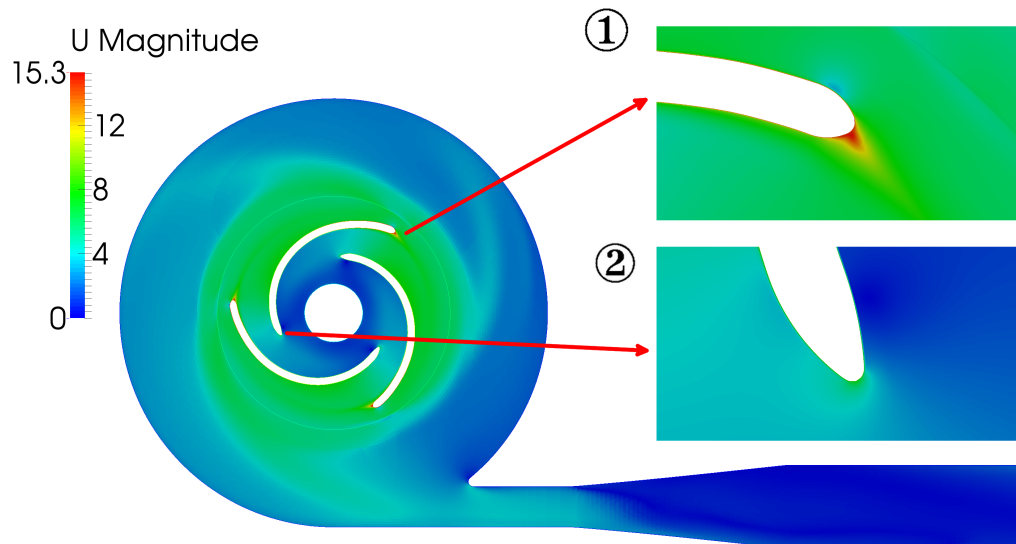

Figure 83: Velocity field in the rotor zone of the OTA-2 pump obtained by MRF simulation.
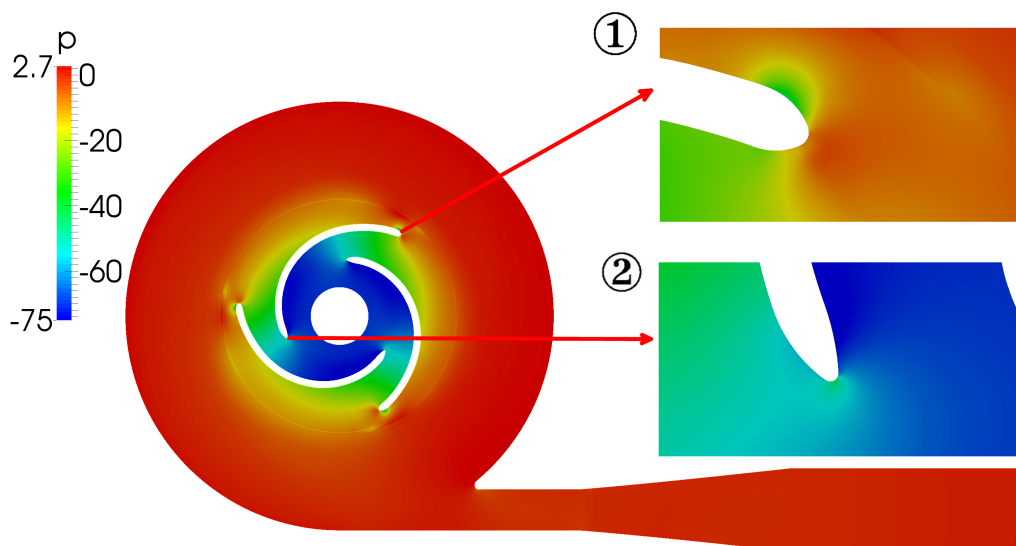
Figure 84: Pressure field in the rotor zone of the OTA-2 pump obtained by MRF simulation.
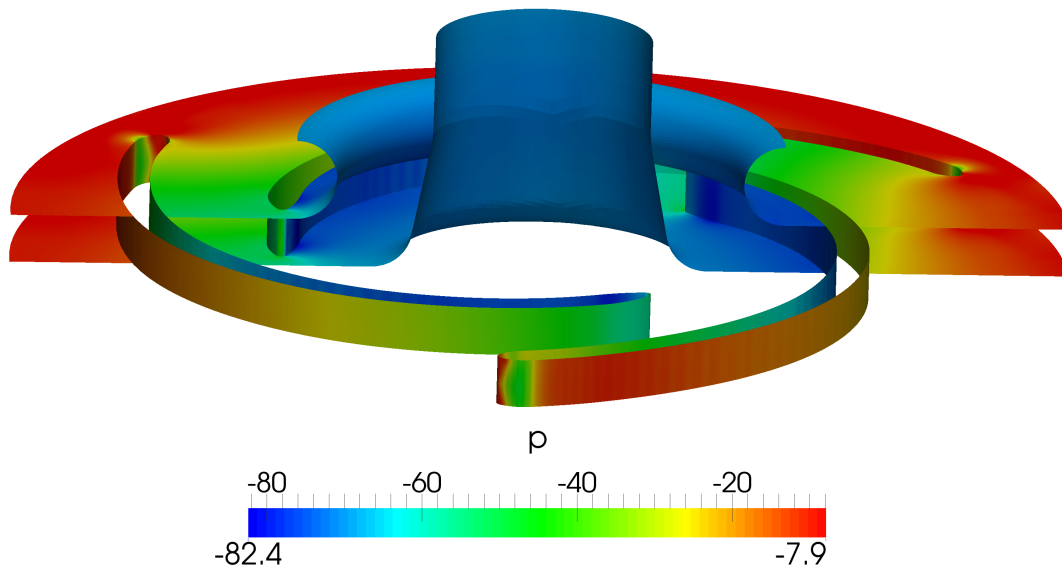
Figure 85: Pressure field over the rotor blades and casing of the OTA-2 pump obtained by MRF simulation.

To predict where the vortices will appear in the flow Q-contour is used. Q-contour with the value equal to 250 is shown in the Figure 86. It can be seen that the vortices appear behind the rotor blades. Three smaller vortices are combined in the bigger one that leaves the pump through the outlet pipe.
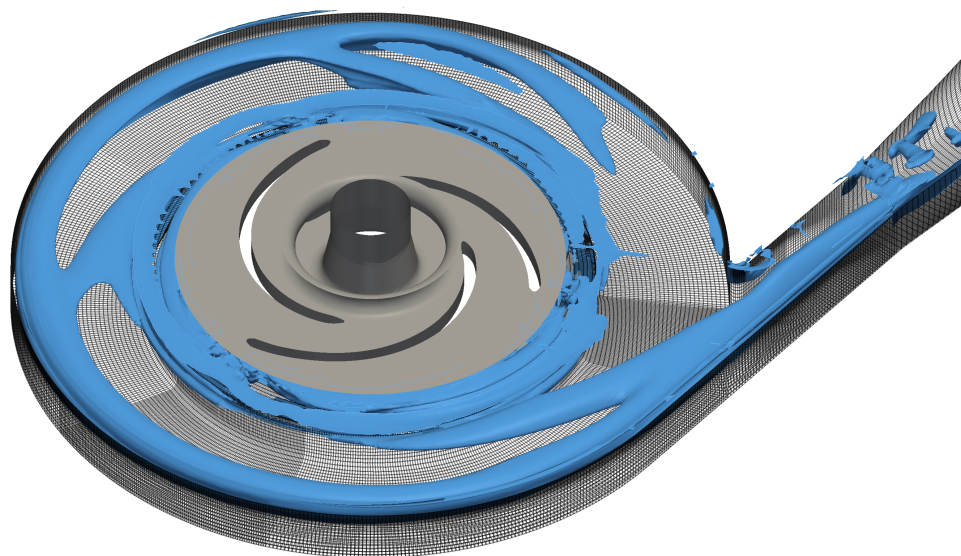

Figure 86: Q=250; for indication of the vortices around the rotor.

The same can be noticed if the flow distribution in the outlet casing is observed. Figure 87 shows the distribution of the flow in the outlet casing, with the detail of one of the cross-sections. Area of higher turbulence intensity can also be presented with the turbulent kinetic energy field distribution, depicted in the Figure 88.
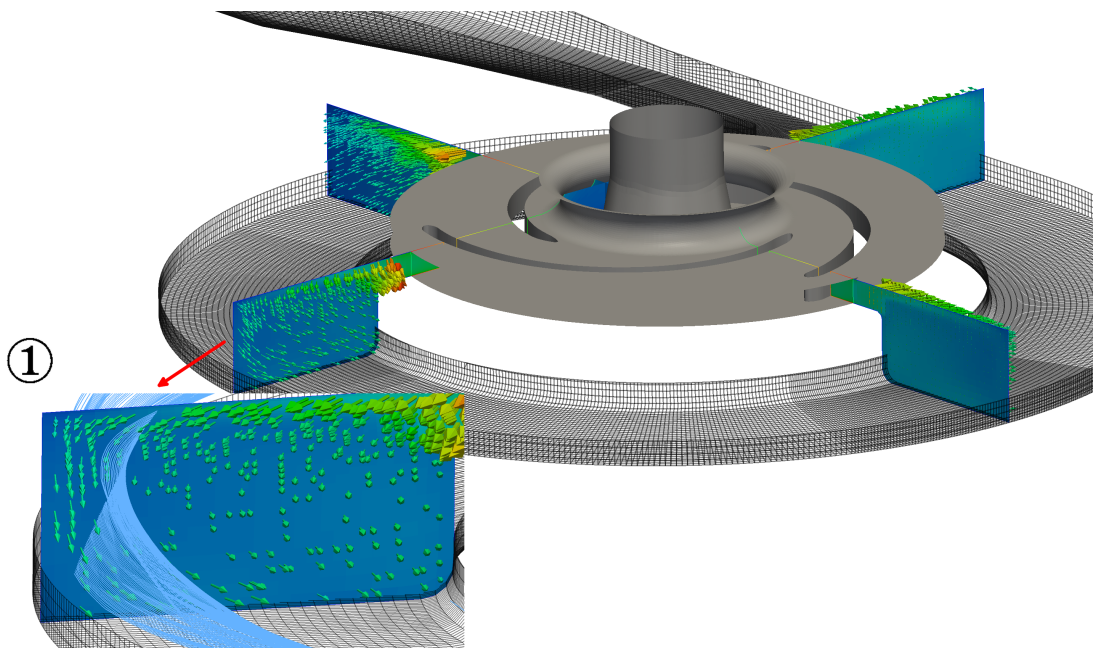

Figure 87: Distribution of flow in the outflow casing of the OTA-2 pump.
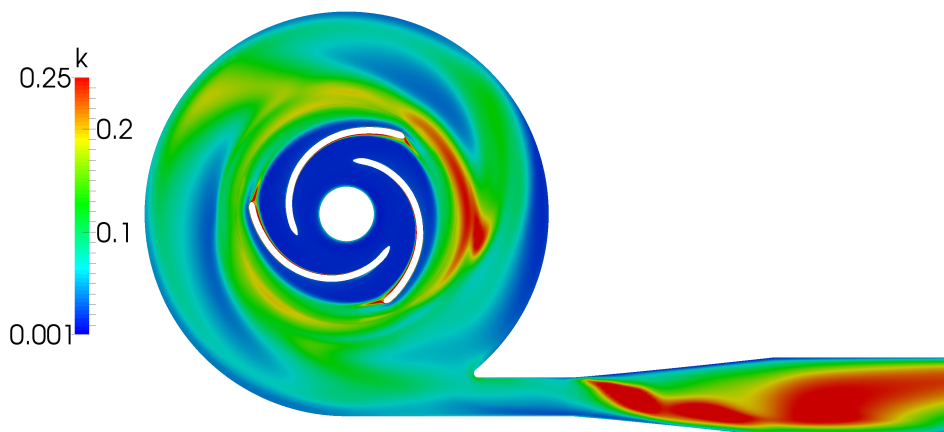

Figure 88: Distribution of turbulent kinetic energy in the outflow casing of the OTA-2 pump.

Performance curves

Simulated operating points are defined with the volumetric flux in the same way as for transient simulation. Figure 89 shows graph of pump head for first operating point. Maximum oscillation of head equals 0.03% and therefore, it can be concluded that the simulation results have converged. Value of the head equals 7.2 m, power is 1612.6 W and efficiency is 69.2% for 7900th iteration.
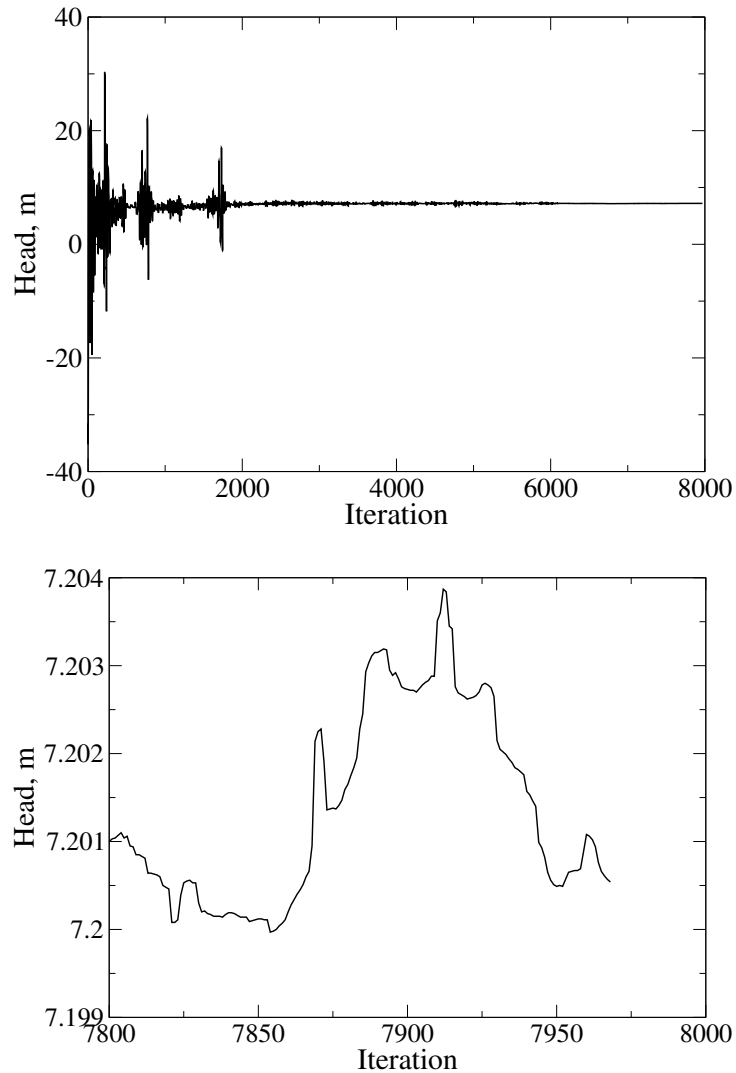

Figure 89: Convergence graphs for MRF simulation of the OTA-2 pump for the first operating point.

Second operating point is defined with lower volumetric flux than the first operating point and therefore the obtained value of head is greater. Oscillation of head is shown in the lower subfigure of Figure 90 and the maximum value equals 0.03%. Value of the head equals 7.8 m, power is 1476.1 W and efficiency is 69% for 5350th iteration.
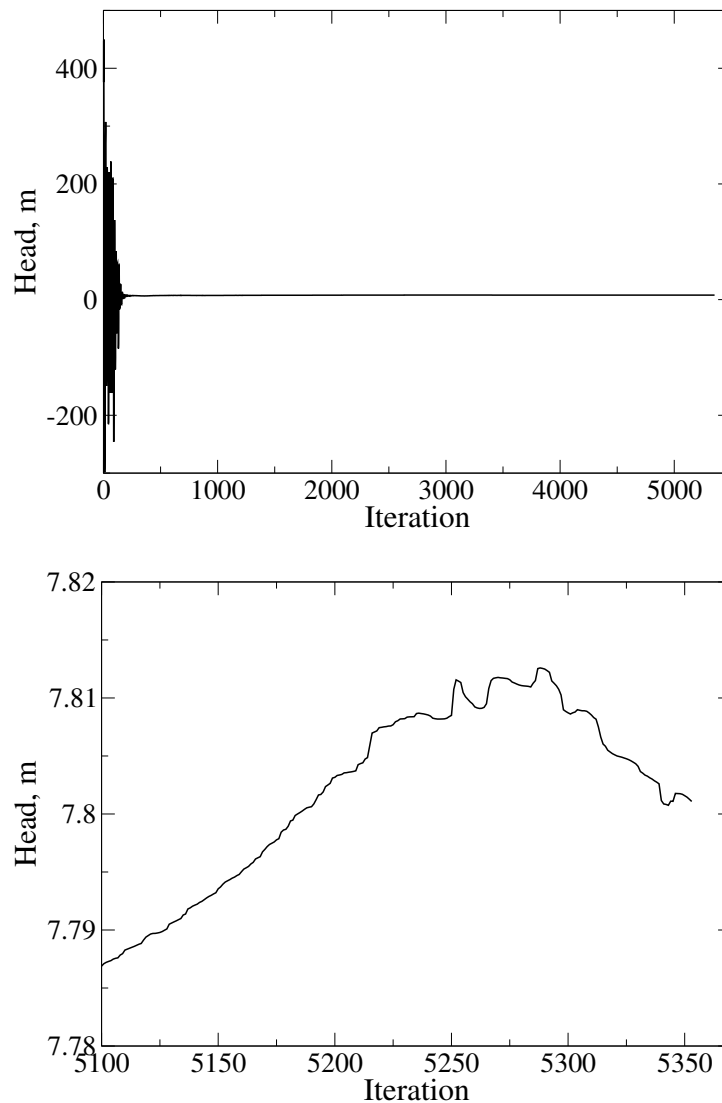

Figure 90: Convergence graphs for MRF simulation of the OTA-2 pump for the second operating point.

Third operating point is defined with higher volumetric flux than the first operating point and therefore obtained value of head is lower. Oscillation of head is shown in the lower subfigure of Figure 91 from which can be noticed that the maximum oscillation of head equals 0.03%. Value of the head equals 4.86 m, power is 1667.5 W and efficiency is 59.5% for 10,900th iteration.
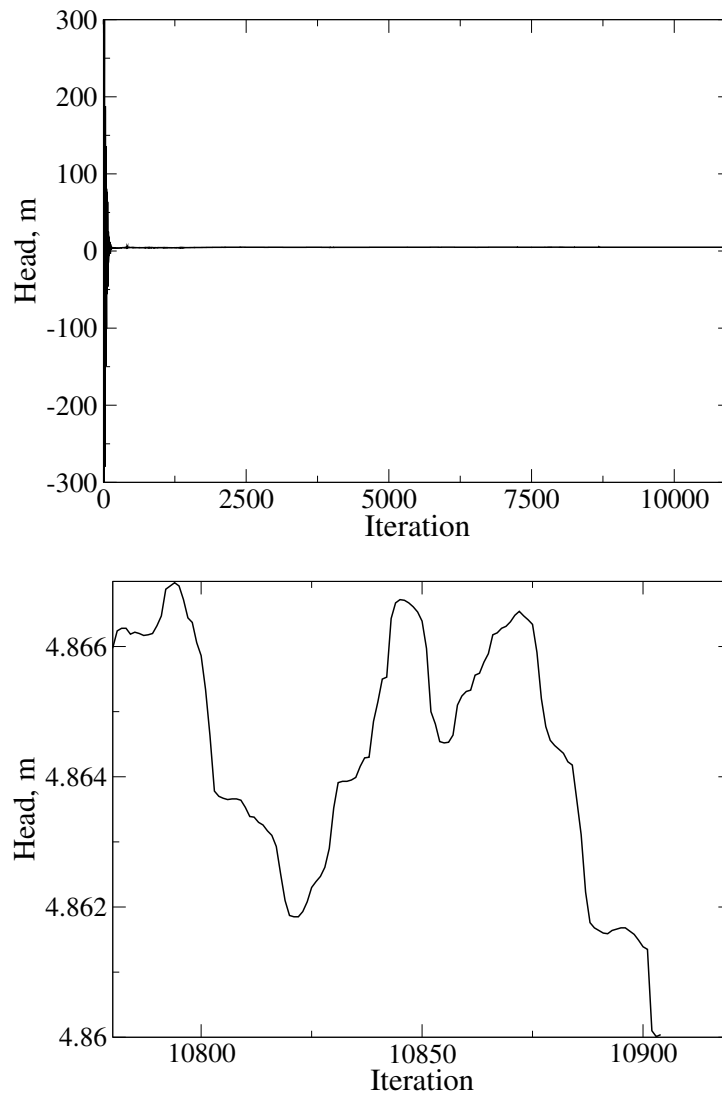

Figure 91: Convergence graphs for MRF simulation of the OTA-2 pump for the third operating point.

From the results of head and efficiency obtained by simulations of different operating points $Q - H$ and $Q - \eta$ curves are generated by an approximation of the points with a parabola. Both curves are present in a single diagram shown in a Figure 92.
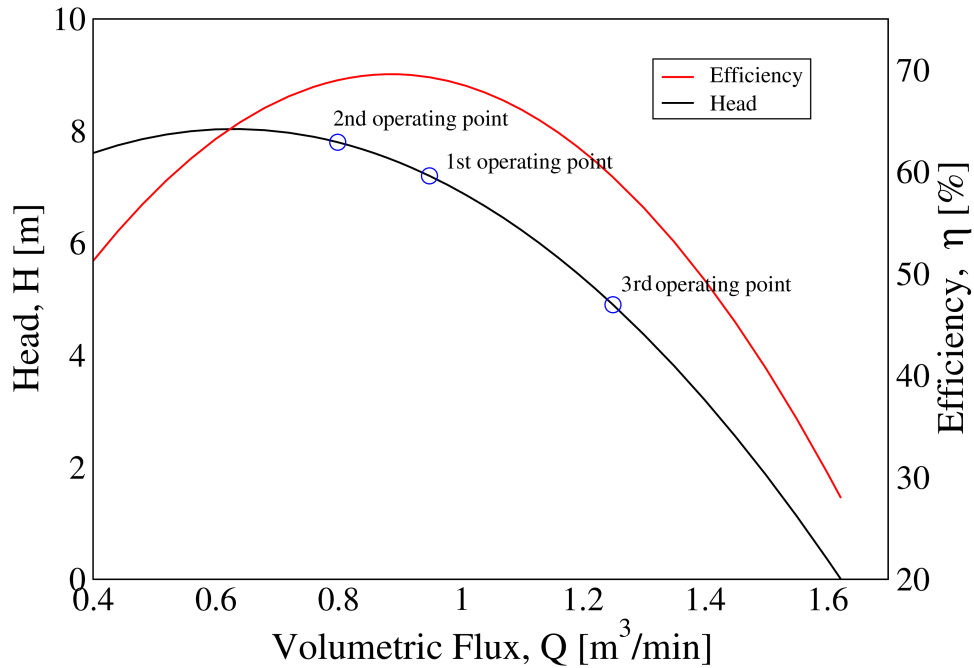
Figure 92: $Q - H$ and $Q - \eta$ performance curve of the OTA-2 pump.

5.4.3 Multiple Reference Frame Simulation with Mixing Plane Interface

Simulation with the mixing plane instead GGI was performed only to show the differences between results and therefore, only the operating point with the maximum efficiency is simulated. This operating point is defined with the volumetric flux which equals 0.95 m^3/s.

To set up a case for MRF simulation with the mixing plane interface boundary and initial conditions are defined in the same way as for simulation with the GGI, with an exception of the boundary condition for interfaces. For master and shadow patches of the interfaces, GGI is replaced with mixingPlane. As a convergence criterion for the simulation, head is monitored. Criterion for the converged results is the maximum oscillation of head equal to 2%. To solve a pressure equation, BiCGStab linear system solver is used. Hence, CPU time required for the simulation can not be compared to the transient and the GGI simulation.

Flow fields and turbulence parameters

Figures presented in this subsection show the details of the flow around the stator blades and in the rotor casing and they also cover the details of the flow in the inlet and outlet pipes. Velocity distribution in the stator casing is shown in the Figure 93. It can be seen that the flow behind the stator guiding blades is the same as for transient simulation and MRF simulation with the GGI. Closer look at the flow around the stator blades is given in the detail of the figure. Pressure field in the stator casing is shown in the Figure 94 with the detail showing the pressure distribution around one of the stator blades.
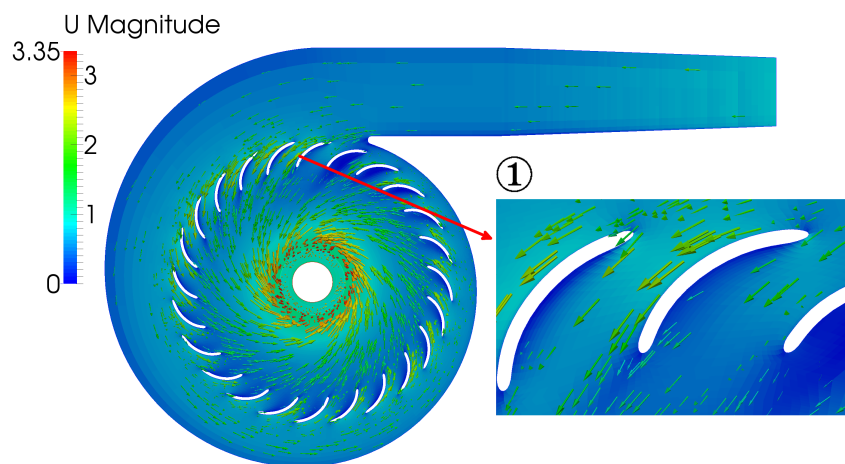

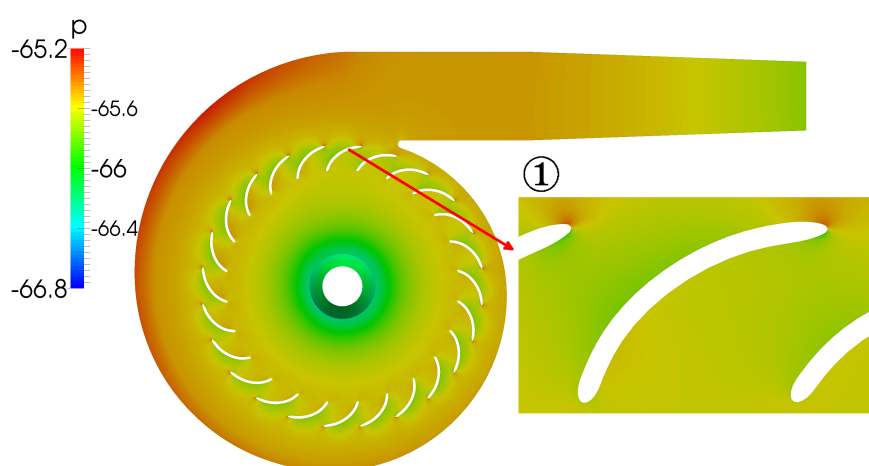Figure 93: Velocity field obtained by MRF simulation with mixing plane for the OTA-2 pump.

Figure 94: Pressure field obtained by MRF simulation with mixing plane for the OTA-2 pump.

Transition of flow between the stator and rotor is shown in Figure 95. Detail 1 of the figure

shows how the flow enters the rotor cell zone, while the detail 2 shows the flow vectors distribution in the outlet casing. It can be seen that the composition of the flow in the outlet casing is similar to the one obtained by simulation with GGI.
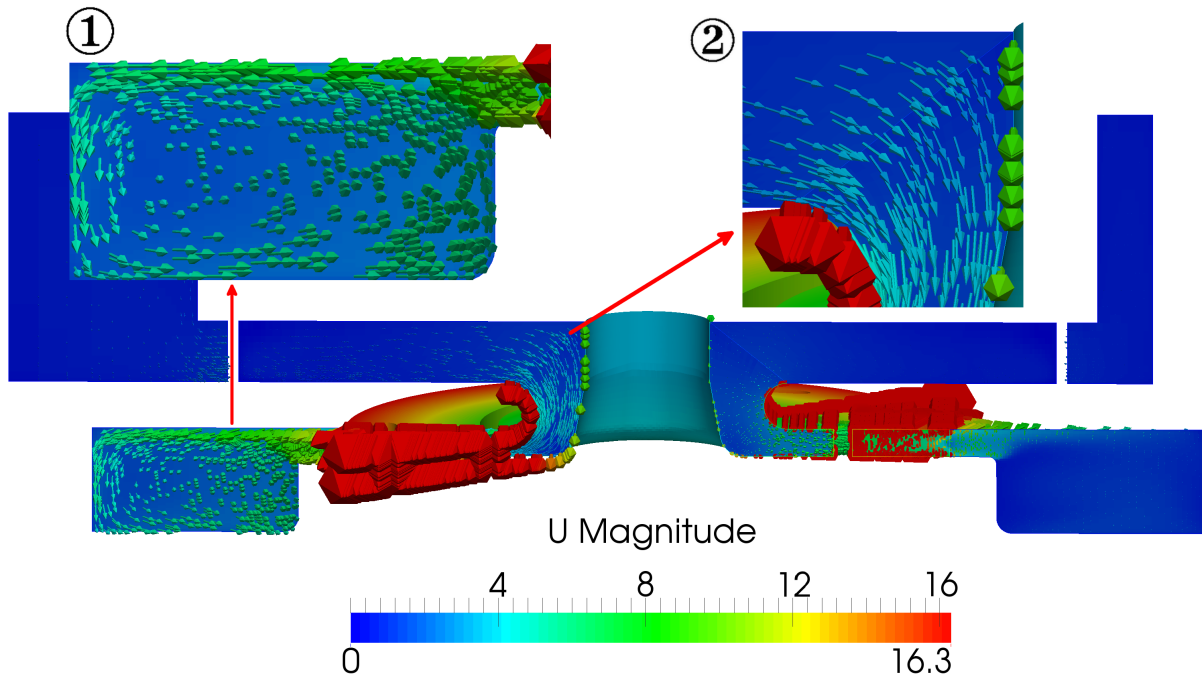

Figure 95: Transition of flow between the rotor and stator cell zones through mixing planes.

Figure 96 shows the velocity distribution in the rotor casing and the vectors of velocity over the mixing plane interface. It can be noticed that all the vectors have the same magnitude and the same angle relative to their corresponding position vector due to circumferential averaging.
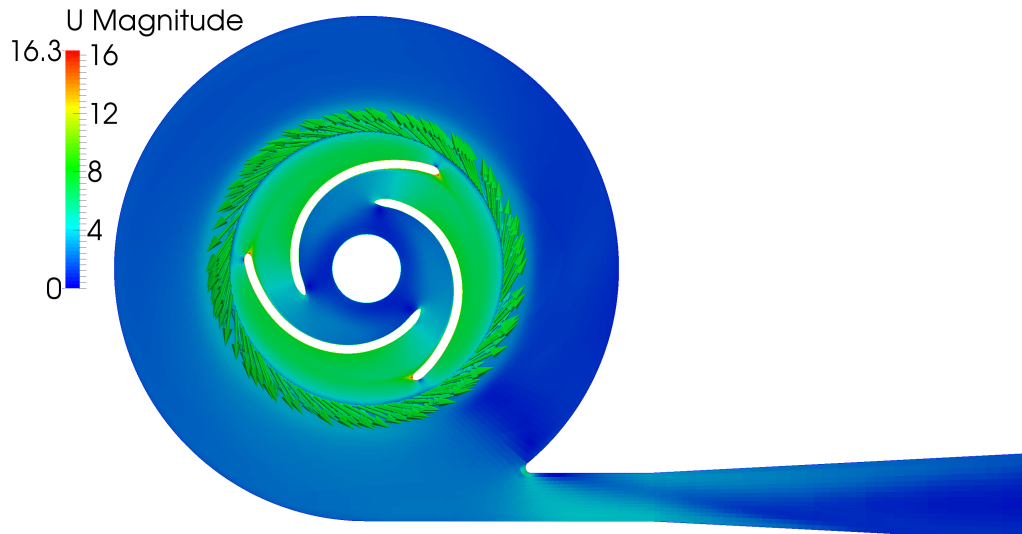
Figure 96: Velocity field in rotor casing obtained by MRF simulation with mixing plane for the OTA-2 pump.

Figure 97 shows the distribution of turbulent kinetic energy. It can be noticed that the wakes behind the rotor blades do not occur due to the averaging of velocity what influences the result negatively. Therefore, the mixing plane interface can be used only if the effect of the wakes behind the rotor blades is not negligible. In the Figure 99 and Figure 100 pressure and velocity distribution over the interfaces are shown.
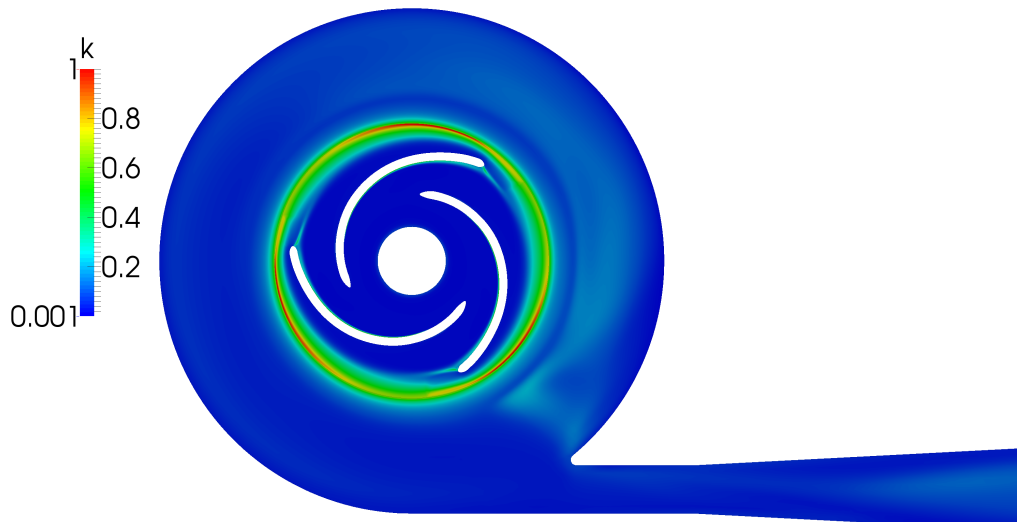

Figure 97: Turbulence kinetic energy field in rotor casing obtained by MRF simulation with mixing plane for the OTA-2 pump.

(a) Rotor inlet   (b) Rotor outlet
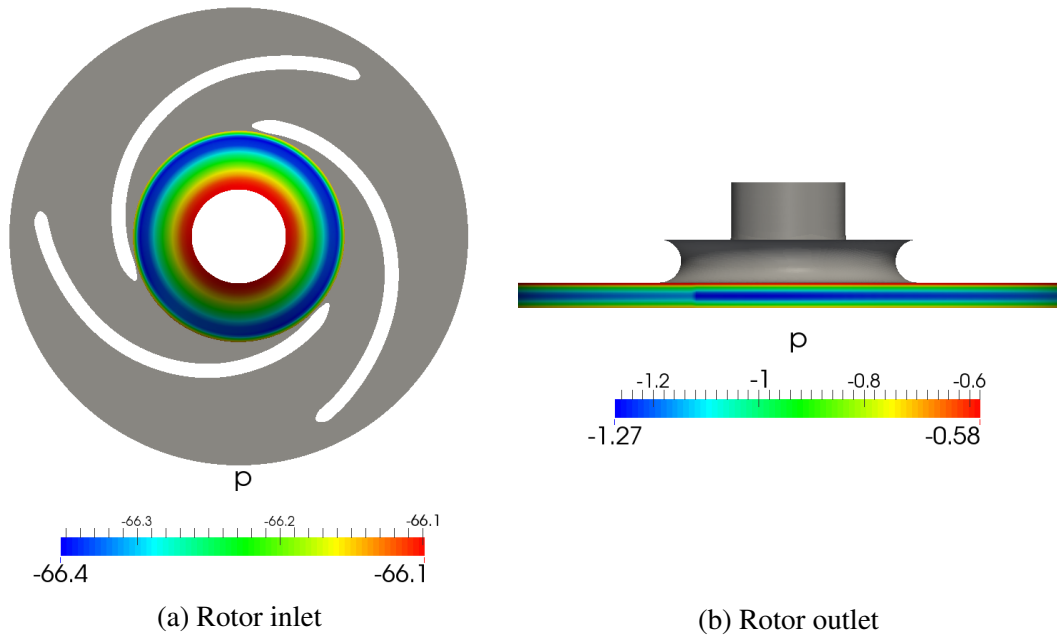
Figure 98: Distribution of pressure over the mixing plane interfaces for the OTA-2 pump.

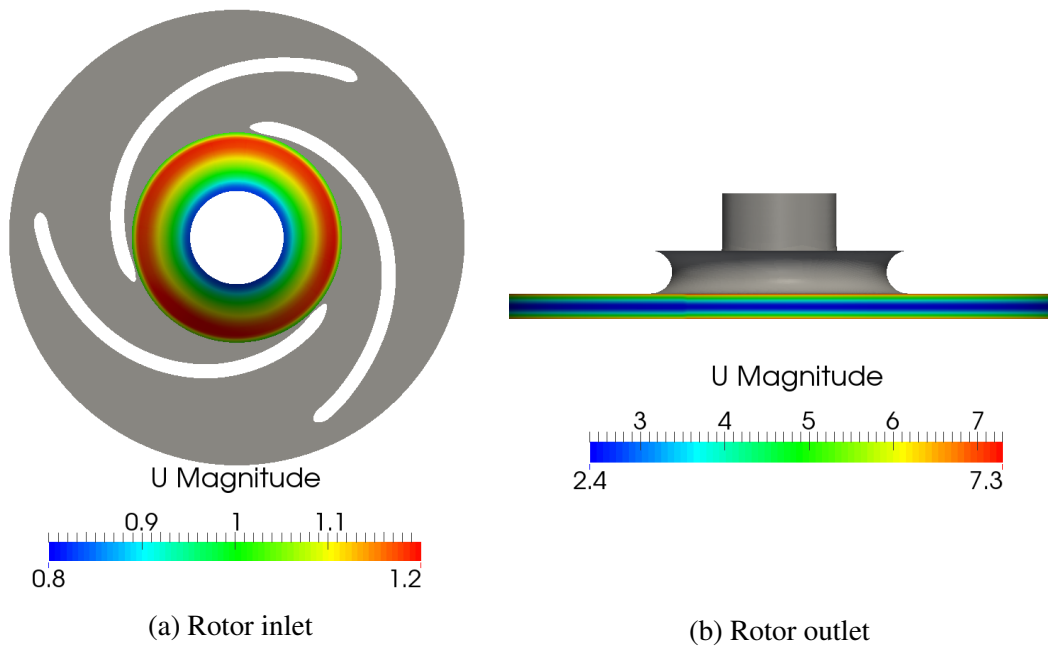(a) Rotor inlet   (b) Rotor outlet

Figure 99: Distribution of velocity over the mixing plane interfaces for the OTA-2 pump.

Convergence of results

Convergence of the results is monitored using head values. Criterion for the converged results is for head not to oscillate more than 1%. In the Figure 100 convergence graphs are shown. From the lower subfigure, it can be seen that the relative error of head equals 0.1%, what was enough to declare convergence of the results. For the 4800th iteration pump head equals 6.7 m, power 1722.4 W and efficiency 60.6%. Compared to MRF simulation with GGI for first operating point it can be seen that efficiency of the pump approximates the values obtained by transient simulation and the simulation with GGI well due to the weaker interaction between the rotor and stator geometry than for the OTA-1 pump. Compared to transient simulation, simulation with mixing plane gives closer values than the simulation with GGI. Therefore, mixing plane interface is recommended for simulation of turbomachinery with geometry where the stator blades and the stator casing are on the significant distance from the rotor blades.
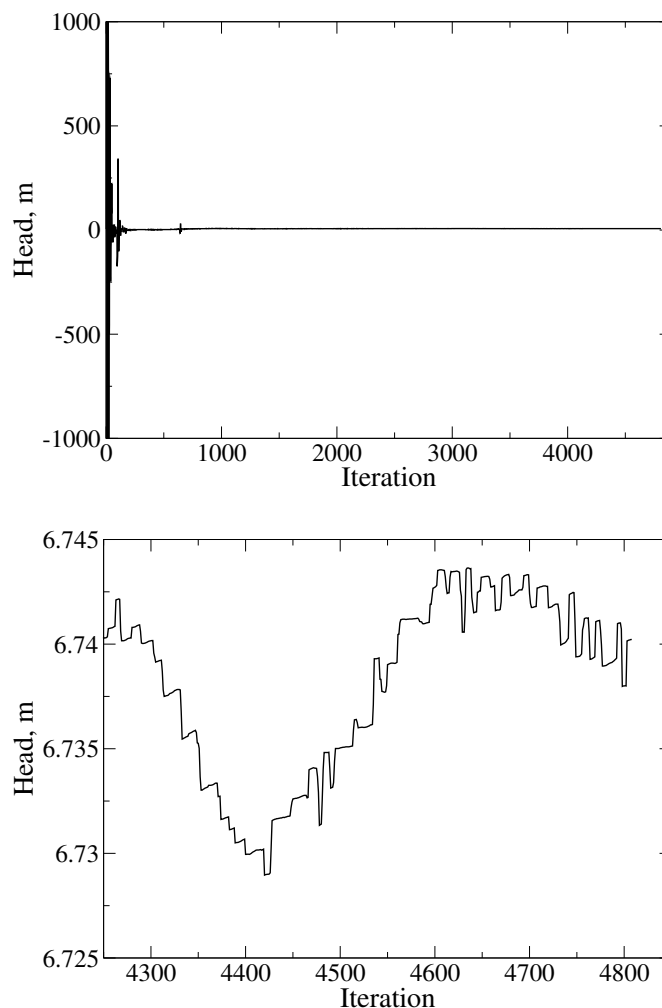

Figure 100: Convergence graphs for MRF simulation of the OTA-2 pump with the mixing plane interface.

5.4.4 Harmonic Balance Simulation

Harmonic balance simulation is a quasi steady-state simulation that enables the user to simulate defined time instances of periodic phenomena. Number of time instances simulated depends on the desired number of harmonics. On the other side, greater number of harmonics increases the required CPU time.

Case set-up for harmonic balance is different from the previous simulations. Initial and boundary conditions have to be defined for $(2n + 1)$ time instances, where n is desired number of harmonics. This simulation is performed to show the differences in the flow fields obtained by the harmonic balance method and for the purposes of the simulation desired number of harmonics is set to 1. Hence, time instances in which results are calculated are T, $\frac{1}{3}T$ and $\frac{2}{3}T$. T is the time after which periodic phenomenon repeats. Period time for the simulation is assumed to be required time for the rotor to make one full revolution. Therefore, angular velocity is defined two times in the case set-up. First time in dynamicMeshDict to specify the angular velocity of the rotor cell zone and the second time in the harmonicBalanceDict to connect angular velocity with the base frequency of the periodic phenomena observed. Turbulence model used in this simulation is $k - \varepsilon$ and the rotor-stator interface is GGI.

Flow fields and the turbulence parameters

Harmonic balance simulation is performed only for the operating point with the maximum efficiency which is defined with the volumetric flux of 0.95 m^3/s. All the presented figures will contain fields obtained for the time instance $\frac{1}{3}T$. Figure 101 shows a velocity field in the stator casing. In the detail of the figure is shown the flow distribution over the stator blades. It can be seen that the value of the maximum velocity is the same for all the presented numerical simulations of the OTA-2 pump. Pressure field in the stator cell zone is shown in Figure 102. The pressure drop, which can be seen in the figure, is the result of the same phenomena explained for the other simulation models.
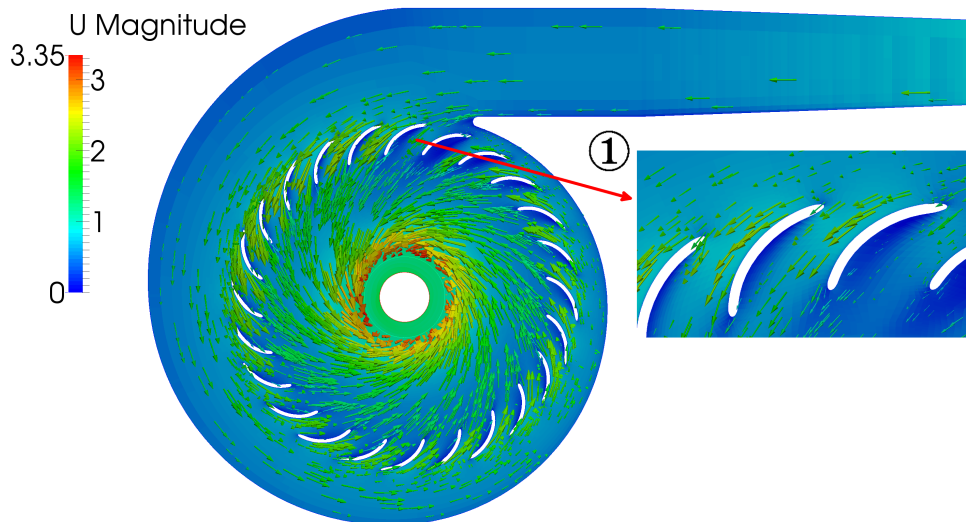
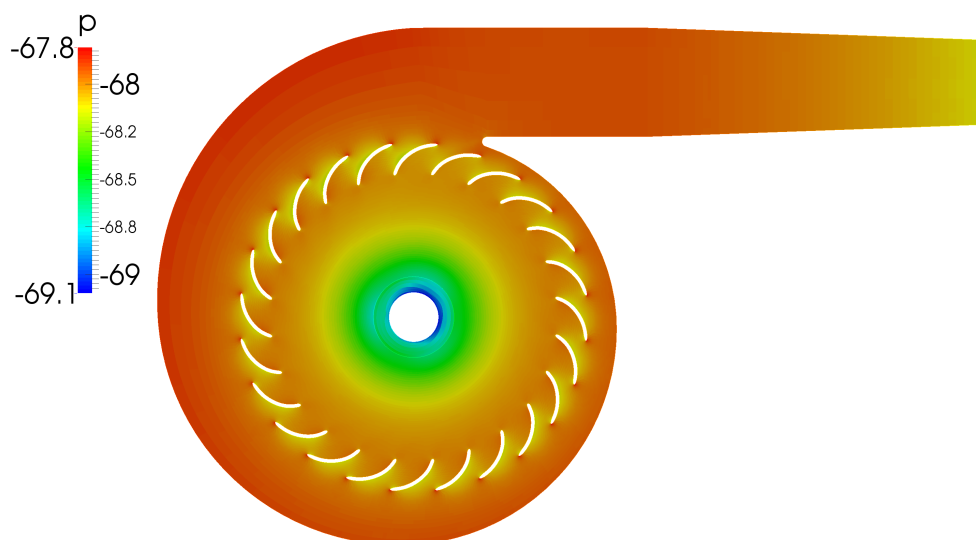Figure 101: Velocity field in stator casing obtained by harmonic balance.

Figure 102: Pressure field in stator casing obtained by harmonic balance.

Transition of flow between the stator and rotor cell zones is shown in Figure 103. In the detail 1 of the figure the flow distribution in the outlet casing of the pump is shown, while in the detail 2 a transition from the stator casing to the rotor casing is shown. Pressure and velocity distribution in the rotor casing have the highest impact on the results of the simulation. Fields with the details around the leading and trailing edge of the rotor blade are shown in Figure 104 and Figure 105. Distribution of pressure over the rotor casing and blades is shown in the Figure 106
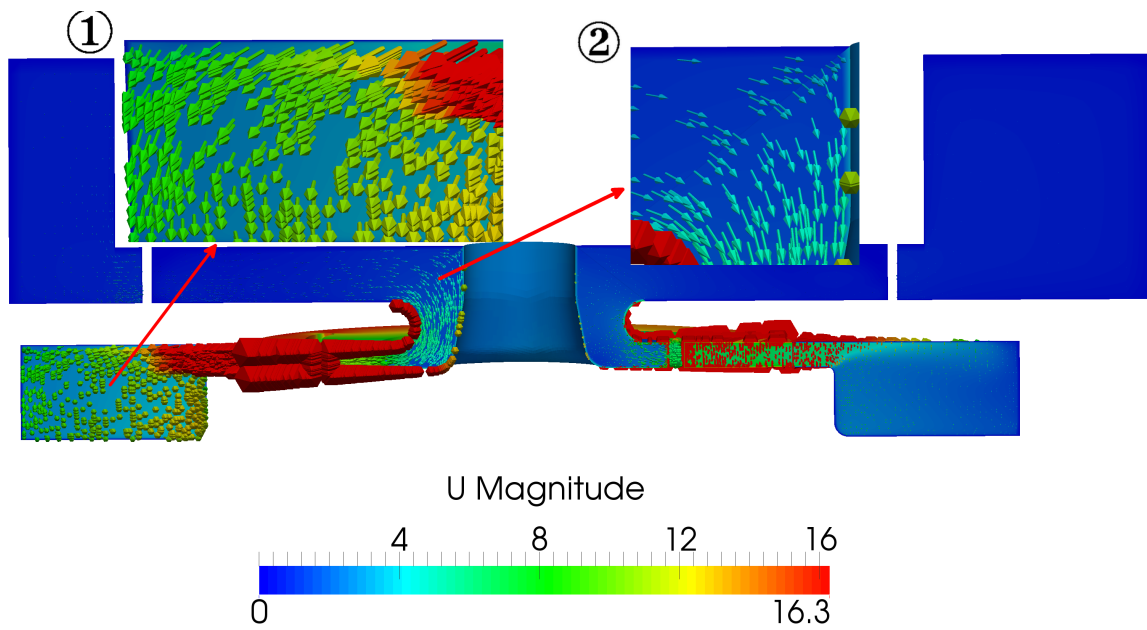
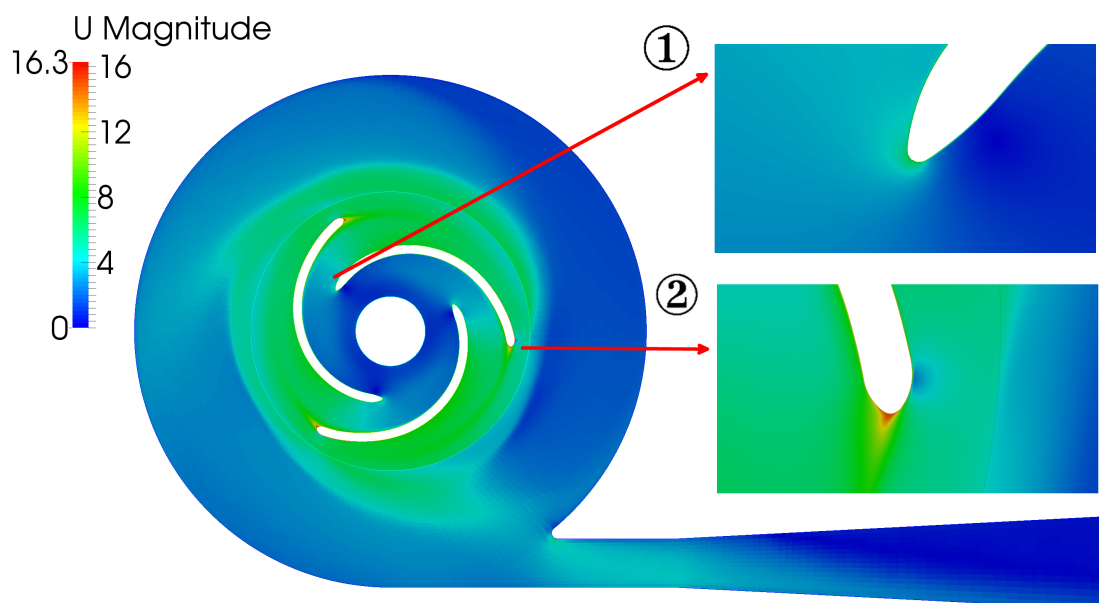Figure 103: Transition of flow from stator to rotor casing obtained by harmonic balance.

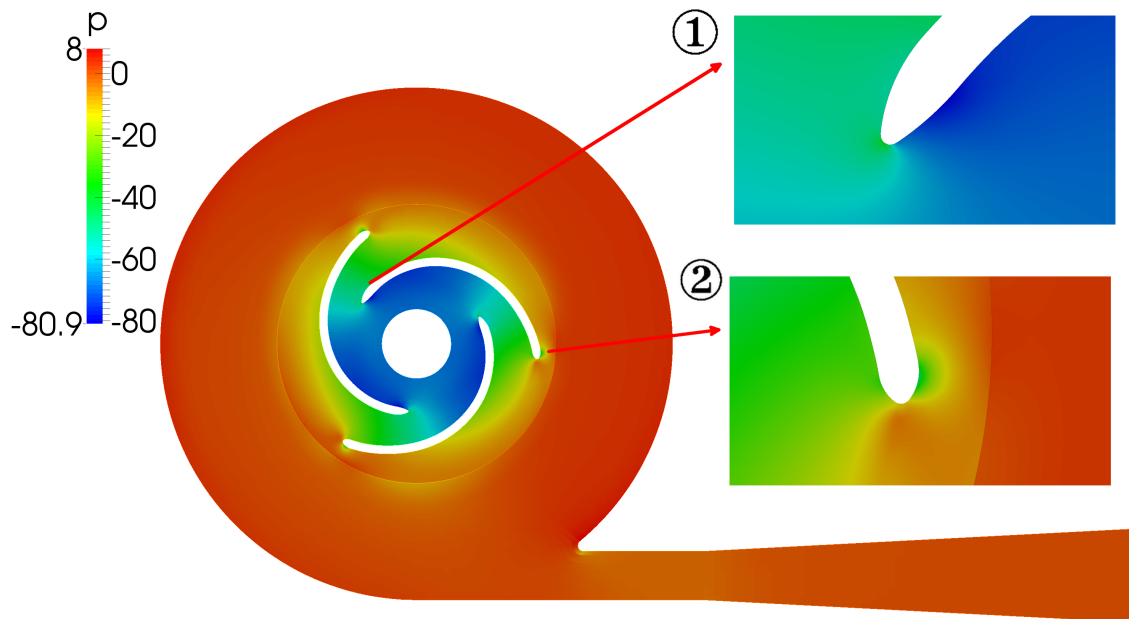Figure 104: Velocity field in rotor casing obtained by harmonic balance.

Figure 105: Pressure field in rotor casing obtained by harmonic balance.
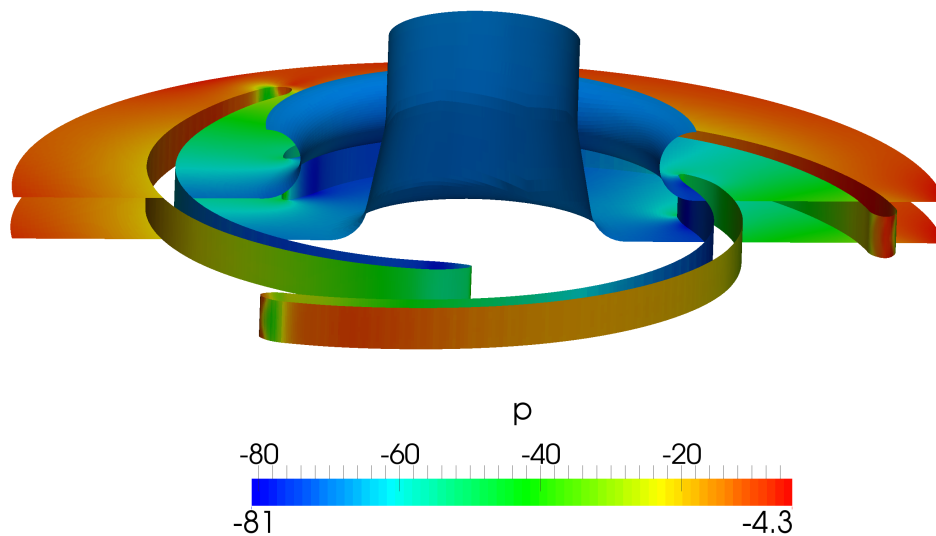
Figure 106: Pressure over the rotor obtained by harmonic balance.

Convergence of results

Convergence of the results is monitored using head values. Criterion for the converged results is the maximum value of head equal to 2%. Figures 107, 108 and 109 show convergence graphs. Difference from other simulations presented is that the results have to converge for the $(2n + 1)$ time instances that are simulated. For the purposes of the thesis only one harmonic is taken into account and therefore, simulation had to converge for 3 time instances. Last iteration of the

simulation is 23,000 due to the convergence problems. Results for head, power and efficiency for all time instances are given in the Table 7.

Table 7: Result for different time instances.

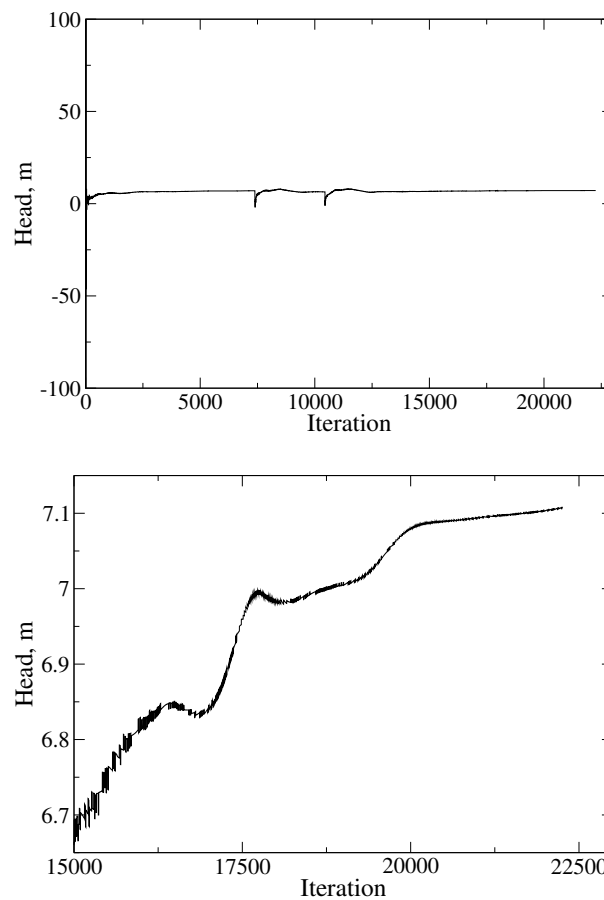| Time	Head, m	η , %	Power, W
$\frac{T}{3}$	7.11	65.87	1669
$\frac{2T}{3}$	7.16	66.37	1668
T	7.12	65.99	1669

Figure 107: Convergence graphs for $t = \dfrac{T}{3}$.
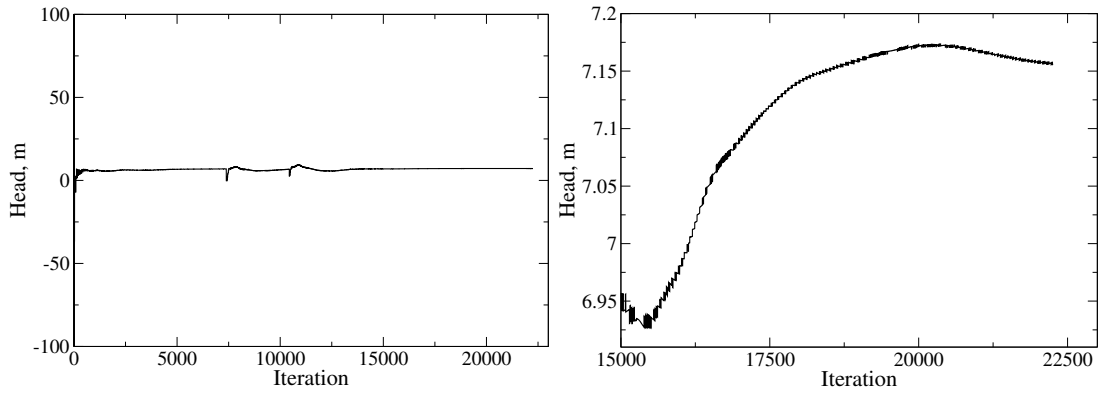
Figure 108: Convergence graphs for $t = \dfrac{2T}{3}$.
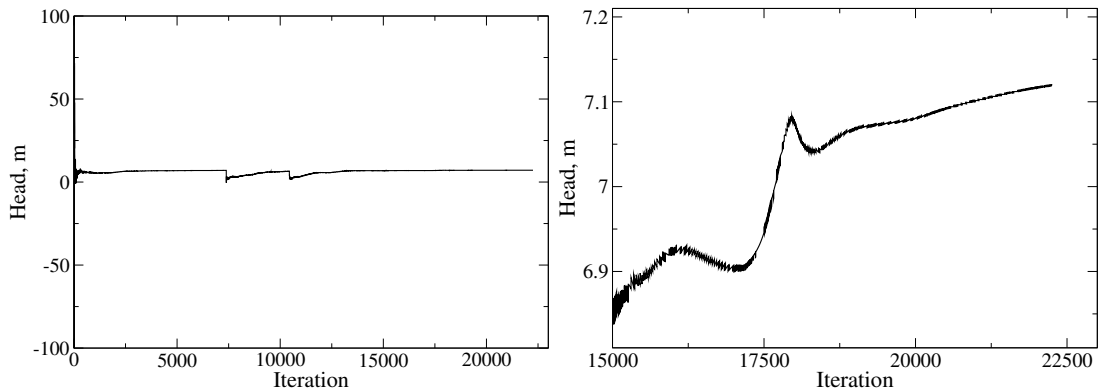
Figure 109: Convergence graphs for $t = T$.

5.4.5 Accuracy of the results

Results for first operating point are compared with assumption for transient simulation to be the most accurate. In Table 8 are shown results of head, efficiency and power for all the simulations. Relative errors represented in the table are calculated according to the value of corresponding value for transient simulation. MRF simulation with mixing plane interface gives the best agreement with the transient simulation, but the results from MRF simulation with GGI and harmonic balance agree with the transient simulation well.

Table 8: Result comparison of the OTA-2 pump.

Simulation	Head, m	H_{Err} , %	η , %	η_{Err} , %	Power, W	P_{Err} , %
Transient	6.8	-	60	-	1650	-
MRF (GGI)	7.2	-9.1	69.2	-15.3	1612.6	2.3
MRF (mixing plane)	6.7	-1.5	60.6	-1	1722.4	-4.4
HB ($\frac{T}{3}$)	7.11	-4.6	65.87	-9.8	1669	-1.15
HB ($\frac{2T}{3}$)	7.16	-5.2	66.37	-10.6	1668	-1.15
HB (T)	7.12	-4.7	65.99	-10	1669	-1.15

5.4.6   Closure

This sections presents different numerical methods for the simulation of the OTA-2 pump. Transient simulation is assumed to be the most accurate and the accuracy of the results are assessed relatively to the results obtained by transient simulation. It is shown that mixing plane gives the best results compared to the transient simulation. To have consistent performance curves of pumps for the OTA-2 and the OTA-1 pump, curves are also made from the result of different operating points for MRF simulation with GGI. CPU times required for the simulations are not compared due to the different mesh used for MRF simulation with GGI. Another reason is that the linear system solver for calculation of pressure for the simulation with mixing plane is BiCGStab instead of AMG. Therefore, simulations cannot be compared on the basis of the CPU time required to perform the simulation.

6   Conclusion

This thesis deals with the numerical models that are nowadays used in the simulation of centrifugal pumps. From the work presented here it can be concluded that the flow in the centrifugal pumps can be simulated using Computational Fluid Dynamics. Therefore, expensive experiments can be replaced by numerical simulations. There are different methods used for numerical simulations of centrifugal pumps. Best results are obtained if the flow is simulated using fully transient simulation with dynamic mesh. However, transient simulation requires more CPU time than a steady-state approximation and for the rotation, the numerical mesh

has to be axisymmetrical what requires additional steps in mesh generation process. MRF model is a steady-state simulation often used as a preliminary step to obtain results that are close to transient simulation. Critical part of such simulations is rotor-stator interface treatment which is used to couple rotor and stator zone into a single domain. Selection of rotor-stator interface treatment used in flow simulation can affect the accuracy and the time required to perform numerical simulation. Simulation results show that using a mixing plane interface in geometries with little space between rotor blades and stator casing gives a less accurate solution in case of OTA-1 pump. On the other side, results obtained by mixing plane for OTA-2 pump give closer results to transient simulation than simulation with the GGI. From mentioned, it can be concluded that the choice of numerical model in simulation of centrifugal pump has a great effect on the results.

If more operating points of a pump are simulated, from obtained results performance curves can be created. Due to the parabolic nature of $Q-H$ and $Q-\eta$ curves, minimum number of needed points is three. In this thesis transient simulation and MRF simulation with GGI are simulated for three operating points to obtain performance curves, while all the other simulations are performed only for the operating point with the maximum efficiency to show the differences in flow.

Comparison of the results is made on the basis of CPU time required and accuracy of the results. Additional methods, which are not specified in the assignment of the thesis, are done to compare additional numerical models. Comparison between consistent and non-consistent simulation shows that the consistent transient solver gives the solution with less oscillations. On top of that, simulations can be performed with the greater time step. Comparison between coupled and segregated solver shows that the coupled solver, even though it requires more memory, improves the convergence of the results. Therefore with the development of new methods for simulations will in future converge faster, yielding lower CPU time.

References

[1] "Impeller," `https://www.ksb.com/centrifugal-pump-lexicon/impeller/191094`, 2009, last access 29.6.2016.

[2] Gregor Cvijetić, "ANALYSIS AND IMPLEMENTATION OF THE HARMONIC BALANCE METHOD IN COMPUTATIONAL FLUID DYNAMICS," 2015.

[3] Beaudoin M., Jasak H., "Development of a Generalized Grid Interface for Turbomachinery simulations with OpenFOAM," 2008.

[4] Beaudoin M., Nilsson H., Page M., Magnan R., Jasak H., "Evaluation of an improved mixing plane interface for OpenFOAM," 2014.

[5] "Pointwise V17.3R5 Release Notes," `http://www.pointwise.com/library/pw_ReleaseNotes.pdf`, 2016, last access 5.7.2016.

[6] Guzović Z., Jasak H., "Hidraulički strojevi (Hidraulic Turbomachinery), Material for lectures," 2013.

[7] Jasak H., Jemcov A., Tuković Ž, "OpenFOAM: A C++ Library for Complex Physics Simulations," 1998.

[8] Jasak, H., "Numeričke metode u mehanici montinuuma (Numerical Methods in Continuum Mechanics), Material for lectures," 2006.

[9] Robert Keser, "Block-Coupled Solution Algorithms for 2-equation Turbulence Models," 2016.

[10] Cvijetić, G., "Steady State Methods for Turbomachinery," 2014.

[11] "See the MRF development," `http://openfoamwiki.net/index.php/See_the_MRF_development`, 2009, last access 29.6.2016.

[12] Jasak H., Cvijetić G., "IMPLEMENTATION AND VALIDATION OF THE HARMONIC BALANCE METHOD FOR TEMPORALLY PERIODIC NON–LINEAR FLOW," 2016.

[13] Beaudoin M., Jasak H., "OpenFOAM TURBO TOOLS: FROM GENERAL PURPOSE CFD TO TURBOMACHINERY SIMULATIONS," 2011.